NUMERICAL STUDY OF SELF-ASSEMBLY OF GRANULAR AND COLLOIDAL PARTICLES

A Dissertation

presented to

the Faculty of Graduate School

at the University of Missouri-Columbia

In Partial Fulfillment

of the Requirement for the Degree

Doctor of Philosophy

By

RAIHAN TAYEB

Dr. Yuwen Zhang, Dissertation Supervisor

July 2021

The undersigned, appointed by the dean of the Graduate School, have examined the dissertation entitled

NUMERICAL STUDY OF SELF-ASSEMBLY OF GRANULAR AND COLLOIDAL PARTICLES

presented by **Raihan Tayeb**,

a candidate for the degree of Doctor of Philosophy in Mechanical and Aerospace Engineering

and hereby certify that, in their opinion, it is worthy of acceptance.

Professor Yuwen Zhang

Professor Frank Feng

Professor Jian Lin

Professor Gary L. Solbrekken

Professor Tommy Sewell

ACKNOWLEDGEMENTS

I would like to express my deepest gratitude to my supervisor, Dr. Yuwen Zhang, who guided me in my research and supported me both academically and financially from the first day at MU. Without his persistent guidance and support this thesis would not be possible.

I would like to thank the members of my thesis committee for their willingness to serve on my committee and for providing me with precious suggestions and insightful comments.

I would like to express great gratitude to my parents whose love and encouragement help me overcome difficulties in study and life. I would also thank my friends and co-workers for all the wonderful time they shared with me.

TABLE OF CONTENTS

LIST OF FIGURES

LIST OF TABLES

NOMENCLATURE

a_{ij}	elements of adjacency matrix
c	species concentration, mol/m^3
c'	sound speed, m/s
$c(i)$	clustering coefficient of particle i
c_p	specific heat, J/kgK
d	diameter of particle, m
d_B	equivalent diameter, m
$dist$	surface separation, m
e	specific internal energy, J/kg
e_{res}	coefficient of restitution
$e_{surface}$	surface energy density, J/m^2
g	gravity, m/s^2
h	smoothing length, m
h_v	enthalpy of vaporization, J/kg
j	mass flux, kg/m^{2}s
k	thermal conductivity, W/mK
k	reaction rate constant (only Chapter 6)
k_B	Boltzmann constant, m^{2}kg/s^{2}K
k_i	degree of a node
k_n	elastic constant, N/m
l	length scale, m

$l^{\dagger}$	characteristic length scale, m
m	mass of particle, kg
m_{eff}	equivalent mass, kg
n	unit normal vector, m
p	hydrostatic pressure, N/m^2
p_{rgh}	dynamic pressure, N/m^2
r	distance vector, m
$\dot{r}$	reaction source term (only Chapter 6)
r_i	position of particle i
s	deviatoric stress tensor, N/m^2
$t_{\max}$	time for collision, sec
x	distance vector, m
y	mole fraction
u	velocity, m/s
A	area of contact, m^2
Area	area of the container, m^2
$\tilde{A}$	adjacency matrix
D	diffusion coefficient, m^2/s
Da	Damkohler number
Dim	System dimension
$D_{\min}$	non-affine deformation
E	Elastic modulus, Pa
Eo	Eotvos number

E'	transformation matrix
F_i	force on particle *i*, N
$F_{\max}$	maximum contact force, N
Fr	Froud number
F'	symmetry matrix
G	Shear modulus, Pa
I	moment of inertia, kg·m^2
K_H	hydrophobic force constant, Nm
Mo	Morton number
N	number of particles
N_s	Number of species
M_w	Molecular weight, kg/mole
$P_{contact}$	normal contact force, N
Pe	Peclet number
PF	packing fraction
Q_s	self-overlap order parameter
Re	Reynolds number
R_i	radius of particle i, m
$\dot{R}^{\beta\gamma}$	rotation rate tensor
R_θ	rotational matrix
R	normalized distance
R_{gas}	Universal gas constant, J/molK
R*	effective radius, m

Sc Schmidt number

Sh Sherwood number

T temperature, K

Trq torque, Nm

T_c critical temperature, K

X position vector, m

U velocity of fluid, m/s

$U(r_{ij})$ pair potential, Nm

V volume of particle, m^3

V_c volume of CFD/Voronoi cell, m^3

V_i area of particle i, m^2

$V(i)$ set of neighboring vertices

W kernel function

Y_v vapor mass fraction

Z average per particle contacts

Greek Symbols

α volume fraction

α_d normalization factor

β constant in SPH equation

γ damping coefficient, s

δ contact deformation/ overlap distance, m

δ_c concentration boundary layer thickness, m

δ_h hydrodynamic boundary layer thickness, m

$\delta_{\max}$ maximum deformation, m

$\delta\varepsilon$ affine shear strain

δ_{ψ} delta function

ε strain matrix

ε_c interface thickness coefficient

ε_{int} interface thickness, m

$\bar{\varepsilon}$ affine dilation

$\in$ permittivity of free space, $C^2/J \cdot m$

$\in_0$ relative permittivity

η EOS parameter

θ rotational angle, rad

κ inverse Debye screening length, 1/m

λ penalty parameter

λ' mean free path of water, m

μ fluid viscosity, Pas

μ_1 mean

μ_3 skewness

μ_4 kurtosis

μ_g air viscosity, N s/m^2

μ_l liquid viscosity, N s/m^2

μ_s sliding friction coefficient

μ_r rolling friction coefficient

μ_v vapor viscosity, N s/m^2

ξ_n normal direction displacement, m

ξ_t tangential displacement, m

ρ density, kg/m^3

ρ_∞ electrolyte concentration, mole/m^3

$\boldsymbol{\sigma}$ stress tensor, N/m^2

σ_l liquid surface tension, N/m

σ^p Poisson ratio

$\tilde{\sigma}$ standard deviation

τ time delay

$\tau^\dagger$ characteristic time scale

ϕ surface charge, C/m^2

ϕ_i local packing fraction

$\tilde{\phi}$ gas-phase fugacity coefficient

χ_4 four-point susceptibility

ψ level set function parameter

$\tilde{\psi}$ color function

ψ_0 particle surface potential, J/C

ω angular velocity, rad/s

$\tilde{\omega}$ mass fraction

Γ EOS parameter

Π artificial viscosity term

Symbols

< > area averaged

ABSTRACT

Self-assembly of granular materials and colloids are studied using several different computational methods such as Discrete Element Method (DEM), Smoothed Particle Hydrodynamics (SPH) method, finite volume Volume of Fluid and DEM (VOF-DEM) method and coupled VOF-Level Set and Dissipative Particle Dynamics (CVOFLS-DPD) method. A history dependent contact model is developed for the DEM and a cohesion model is introduced to study the packing of granular materials under cohesive forces. The study reveals granular size and size distribution has an important effect on the final packing structure. The study using SPH method reveals stress relaxation in a granular system subjected consecutive jamming cycles. However, above a certain initial packing fraction stress relaxation is found to be negligible. Further analysis reveals characteristics length and time scales for stress relaxation. Three-cycle basis is found to be the most preferred configuration of the particles as the granular system drives towards a more stable state. The study using VOF-DEM method reveals pattern formation by colloidal deposits as a thin film of fluid evaporates. Further analysis with CVOFLS-DPD method reveals interface forces on particles need to be carefully modeled to prevent escaping of particles during evaporation. The use of machine learning (ML) for computational study is also explored in this study. A machine-learned sub-grid scale (SGS) modeling technique is introduced for efficient and accurate prediction of reactants and products undergoing parallel competitive reactions in a bubble column. The machine-learned model replaces the iterative approach associated with the use of analytical profiles for previous sub-grid scale models for correcting concentration profiles in boundary layers.

1 INTRODUCTION

Self-assembly is an autonomous process by which individual components arranged themselves into an ordered structure. The term is generally reserved for building blocks not linked together by covalent bonds but assembled by weak or short-range forces or hard-particle interactions. Granular materials and colloids both exhibit self-assembled structures but the former is characterized by out-of-equilibrium self-assembly due to athermal nature of the system. The discrete particles of the granular system can exhibit a wide range of interesting collective behaviors such as pile formation, fluid-flow like behavior, and fracture. Understanding these behaviors are important in many industrial applications such as mining, construction, agriculture, and packing. Geological processes such as landslide, avalanche, erosion, sedimentation, and plate tectonics are also governed by collective granular structural behavior. One particular aspect of granular material is the phenomenon of jamming where randomly organized system of particles changes from mechanically unstable states to stable states. Jamming phenomena are also observed in colloids, foams, and glass transition in molecular liquids. In most of these cases, the system starts from an unjammed state and gradually transition to a jammed state. Sometimes the system undergoes several transitions between jammed and unjammed states. By careful micromechanical simulations like the one presented in this work, one can study the jamming behavior of the system under different loading conditions and derive macroscopic model to replicate such behavior.

In contrast to granular jamming, self-assembly of colloids are affected by thermal fluctuations (Brownian motion), and also by the surrounding fluid medium and electrostatic forces. Colloidal self-assembly has gained widespread attention due to its

application in micro- or nano-scale technologies such as importance in photonics [3], chemical reaction controlling [4], and ink-jet printing technology [5]. One common method to self-assemble colloids is to evaporate the surrounding liquid and let the colloids assemble themselves at the bottom on the substrate [1, 2]. A complete understanding of the process can help in tuning the deposit morphology to cater to its applications. In this study a multi-scale simulation method is developed to study the evaporation induced self-assembly of colloids by taking into account non-ideal mixture properties in evaporating droplet and the roughness of the colloids and substrate.

This dissertation is divided into three parts. Part one composed of two chapters that studies the packing and jamming transition of granular systems. Part two is also made up of two chapters and presents numerical studies on self-assembly of colloids induced by evaporation. Part three discusses the development of a machine learned (ML) computational fluid dynamics (CFD) solver for studying the concentration of reactants and products undergoing parallel competitive reactions in a bubble column. The future works and studies to be done based on the present research and a list of publications produced as a result of this doctoral work are also provided.

The objectives for the first part are as follows:

1. Develop a history dependent contact force model that includes cohesion in the framework of Discrete Element Method (DEM) for studying granular materials.

2. Develop a meshless Lagrangian solver as part of a high-performance computing (HPC) program that is able to handle the low velocity collisions of the granular particles and at the same time provide better resolution than the traditional DEM for the stress arising within the granular particles.

3. Using the developed HPC program study the evolution of global pressure and microstructure of granular system subjected to consecutive jamming cycles.

4. If there is a variation of global pressure for successive compression cycles the study should the find the cause of such variation using proper statistical analysis such that the relationship between pressure and system configuration can be applied to other granular systems.

The dynamics of near jammed isotropically driven granular assemblies has been studied in the past. However, most of these systems involve shear [3-6], vibration [7, 8] or biaxial strain [9]. In the present study, the granular system is cyclically and isotropically compressed with small strain steps, starting from a packing fraction below jamming, to a packing fraction above jamming. Unlike previous studies which describe the granular system by average coordination number or distribution of contact forces, the mobility of individual particle is studied as well as the mobility of particle cluster is studied using four-point susceptibility measure and Falk-Langer measure of affine and non-affine deformation. The relationship between particles in a cluster is also studied using complex network analysis. The study revealed strong correlation between the rearrangement of particle clusters and the evolution of global stress in the system.

For the second part of the study which deals with the self-assembly of colloids the objectives are:

1. To study and control evaporation induced self-assembly of colloids using a comprehensive multi-scale computational tool.

2. The evaporation model must include multi-component liquid, the evaporation flux should be evaluated directly from the diffusion and convective fluxes at the gaseous

interface, without the need of any evaporation model or empirical correlations. Must adopting a detailed thermodynamic model (including activity coefficients) and the impact of the mixture non-ideality on the evaporation process.

3. The particle model must include colloid roughness (an increase in repulsive force which cannot be accounted for by DLVO theory or hydration forces).

4. Other numerical problems such as contact line pinning, interface effect, lubrication forces and spurious current need to be tackled.

The most commonly observed structure for nanofluid droplet evaporation is the "coffee ring pattern." The capillary flow to the pinned contact line that drives this pattern formation was first observed and reported by Robert Brown in 1829 [10]. After almost 170 years later Deegan et al. [11] provided some mathematical analysis to relate the outward radial velocity to the evaporation rate. After that, there have been many attempts to mathematically model and then simulate the evaporation-induced particle deposition phenomena and understand the effect of different parameters associated with them. These efforts include full-scale Molecular Dynamics (MD) [12] and Dissipative Particle Dynamics (DPD) [13] simulation of both fluids and particles, MD simulation of particles with implicit solvent [14], DPD simulation of particles with flow fields estimated from analytical result under ideal conditions [14], and Finite Element (FE) simulation where particles are assumed as continuum concentration field [15, 16]. All of these numerical methods have their own disadvantages. In order to properly model the evaporation and the surface tension effects, the liquid and the surrounding medium need to be considered as continua whereas the particles need to be considered as discrete to model their interactions with each other and also with the fluid and the substrate. Hence the problem

at hand is inherently multiscale and a multiscale simulation method that can handle the fluids as continua and particles as discrete medium is required. On that endeavor, for the first time, a finite volume coupled volume of fluid-level set method paired with dissipative particle dynamics (CVOFLS-DPD) method is developed for the accurate handling of fluids and particles for evaporation induced self-assembly. Using the aforementioned method, the deposition of colloids in a sessile droplet is studied and the effect of different system parameters are discussed. The computational tool developed is very general and can be study other systems with colloids where there is phase change and interface deformation.

2 ANALYSIS OF COHESIVE MICRO-SIZED PARTICLE PACKING STRUCTURE USING HISTORY-DEPENDENT CONTACT MODELS

2.1 Introduction

This chapter discussed the study on packing of granular materials when cohesive forces are acting between the particles along with a shear stress that depends on the deformation history. To study the process a numerical method known as Discrete Element Method (DEM) is used for the simulation of granular system. This method was originally developed by Cundall for rock mechanics problem. DEM has been showed by Cundall and Hart to be a better tool for modelling discontinuous media compared to other methods like finite element method. DEM is a Lagrangian method where trajectory of each particle is calculated separately using Newton's equation of motion. Collisions among particles and between particles and walls are accounted for using contact force models. Both normal contact force and tangential contact force are accounted for in the contact model. Other forces such as cohesive force, van der Waal force are considered in the equations of motion.

2.2 Equations of motion

For each particle Newton's second law is invoked that provides the equations to solve the translational and rotational motions of the particles.

$$\mathbf{m_i} \frac{\partial^2 \mathbf{X_i}}{\partial \mathbf{t}^2} = \mathbf{F_i} \tag{2.1}$$

$$I_i \frac{d^2\boldsymbol{\theta}_i}{dt^2} = \mathbf{Trq}_i \tag{2.2}$$

$$\mathbf{F_i} = \mathbf{F^n_{ij}} + \mathbf{F^t_{ij}} \tag{2.3}$$

$$\mathbf{Trq_i} = \mathbf{Trq^r_{ij}} + \mathbf{Trq^t_{ij}} \tag{2.4}$$

where m_i is the mass of the i^{th} particle, $\mathbf{X}_i$ is the position vector of the i^{th} particle, I_i is the moment of inertia that equals to $0.4m_iR_i^2$ and the rotated angle of particle i is represented by $\boldsymbol{\theta}_i$. The symbol $\mathbf{F}_i$ in Eq. (1.1) is the resultant contact force generated by two collided particles, i and j. This force can be decomposed further into two components: one is contact force in normal direction $\mathbf{F}_{ij}^n$ and the other is contact force in tangential direction $\mathbf{F}_{ij}^t$, as shown in Eq. (1.3). The symbol $\mathbf{Trq}_i$ in Eq. (1.2) is the resultant torque acting on the i^{th} particle. It can also be decomposed into two components: torques caused by rolling friction and tangential force, respectively, as given in Eq. (1.4).

2.2.1 Contact forces

Contact forces arise when two particles collide. Two contact models are adopted in this work to account for the contact force between two particles. The contact models are both deformation history dependent meaning their deformation in tangential direction is obtained from an integral equation that integrates the tangential velocity from the time of collision to the time of interest. However, the Gran-Hertz-History model describe a nonlinear relationship between contact force and overlap distance, while Gran-Hooke-History model gives a linear relationship. Both models are implemented in the open-source software package LIGGGHTS. The Gran-Hertz-History model is also modified to

include van der Waals force, which can be significant for small particles, and thereby refer to as Modified Gran-Hertz-History model.

Normal contact force

The normal contact force $\mathbf{F}_{ij}^{n}$ can be determined by [17-19],

$$\mathbf{F}^{n}_{ij} = \left[K_n \boldsymbol{\xi}_n - \boldsymbol{\gamma}_n \left(\mathbf{u}_{ij}.\mathbf{n}_{ij} \right) \right] \mathbf{n}_{ij} \tag{2.5}$$

where in Modified Gran-Hertz-History model, parameters are given by,

$$K_n = \frac{4}{3} E_{eff} \sqrt{\bar{R}\xi_n} \,, \boldsymbol{\gamma}_n = 2\sqrt{\frac{5}{6}} \beta_{eff} \sqrt{S_n m_{eff}} \,, \beta_{eff} = \frac{\ln\left(e_{res}\right)}{\sqrt{\ln^2\left(e_{res}\right) + \pi^2}}, \tag{2.6}$$

$S_n = 2E_{eff}\sqrt{\bar{R}\xi_n}$.

and in Gran-Hooke-History model,

$$K_n = \left(\frac{16}{15} \sqrt{\bar{R}} E_{eff} \right)^{0.8} \left(m_{eff} v_{ch}{}^2 \right)^{0.2} , \boldsymbol{\gamma}_n = \sqrt{\frac{4 m_{eff} K_n}{1 + \dfrac{\pi^2}{ln^2\left(e_{res}\right)}}} \,. \tag{2.7}$$

and $\mathbf{v}_{ij}$ represents the velocity of the particle i relative to velocity of the particle j, $\mathbf{n}_{ij}$ is the unit vector point from particle i to particle j, e_{res} is the coefficient of restitution of the particles, $\bar{R} = Rad_i Rad_j / \left(Rad_i + Rad_j \right)$ is the effective radius that represent the geometric mean diameter of the i and j particle, $E_{eff} = 1 / \left(\dfrac{1 - \left(\sigma_1^p\right)^2}{E_1} + \dfrac{1 - \left(\sigma_2^p\right)^2}{E_2} \right)$ is the effective Young's modulus that is calculated in terms of individual Young's modulus and Poisson ratio accordingly, $\xi_n = Rad_i + Rad_j - \left| \mathbf{Rad}_{ij} \right|$ is the overlap in normal direction

and $m_{eff} = \dfrac{m_{\mathbf{i}} m_{\mathbf{j}}}{m_{\mathbf{i}} + m_{\mathbf{j}}}$ is the effective masses of the particles. Characteristic velocity v_{ch} is taken as unity in Gran-Hooke-History model.

Tangential contact force

The contact force in tangential direction is calculated by [20],

$$\mathbf{F}^{\mathbf{t}}_{\mathbf{ij}} = -\mathbf{min}\left[\mu_s \left|\mathbf{F}^{\mathbf{n}}_{\mathbf{ij}}\right|, K_t \left(\boldsymbol{\xi}_{\mathbf{t}} \cdot \mathbf{t}_{\mathbf{ij}}\right) - \gamma_t \left(\mathbf{u}_{\mathbf{t}} \cdot \mathbf{t}_{\mathbf{ij}}\right)\right] \mathbf{t}_{\mathbf{ij}} \tag{2.8}$$

where in Modified Gran-Hertz-History model, parameters are determined by,

$$\begin{gathered} K_t = 8G_{eff}\sqrt{\bar{R}\boldsymbol{\xi}_{\mathbf{n}}}\ , \gamma_t = 2\sqrt{\frac{5}{6}}\beta_{eff}\sqrt{S_t m_{eff}}\ ,\ S_t = 8G_{eff}\sqrt{\bar{R}\boldsymbol{\xi}_{\mathbf{n}}}\ , \\ G_{eff} = 1/\left[\frac{2\left(2-\sigma_1^p\right)\left(1+\sigma_1^p\right)}{E_1} + \frac{2\left(2-\sigma_2^p\right)\left(1+\sigma_2^p\right)}{E_2}\right]. \end{gathered} \tag{2.9}$$

and in Gran-Hooke-History model,

$$K_t = K_n\ ,\ \gamma_t = \gamma_n\ . \tag{2.10}$$

where $\boldsymbol{\xi}_t = \int_{t_0}^{t} \mathbf{u}_t dt$ represents the tangential displacement vector between the two spherical particles, $\mathbf{u}_{\mathbf{t}} = [\left(\mathbf{u}_{\mathbf{i}} - \mathbf{u}_{\mathbf{j}}\right) \cdot \mathbf{t}_{\mathbf{ij}}]\mathbf{t}_{\mathbf{ij}} + \left(\boldsymbol{\omega}_{\mathbf{i}} \times \mathbf{Rad}_{\mathbf{i}} - \boldsymbol{\omega}_{\mathbf{j}} \times \mathbf{Rad}_{\mathbf{j}}\right)$ is the tangential relatively velocity, t_{ij} is the unit vector along the tangential direction, t_0 is the time when the two particles just touch and have no deformation, t is the time of collision, $\boldsymbol{\omega}_i$ or $\boldsymbol{\omega}_j$ is the angular velocities of particles i or j and $\mathbf{Rad_i}$ or $\mathbf{Rad_j}$ is the vector running from the center of particle i or j to the contact point of the two particles.

2.2.2 Van der Waals force

The van der Waals forces among particles are included only in the Modified Gran-Hertz-History model. The van der Waals force, $\mathbf{F}^{\mathbf{v}}_{\mathrm{ij}}$ between particles i and j is given by [21],

$$\mathbf{F}^{\mathbf{v}}_{\mathbf{ij}} = -\frac{H_{\mathbf{a}}}{6} \times \frac{64 Rad_i^{\,3} Rad_j^{\,3} \left(h + Rad_i + Rad_j\right)}{\left(h^2 + 2Rad_i h + 2Rad_j h\right)^2 \left(h^2 + 2Rad_i h + 2Rad_j h + 4Rad_i Rad_j\right)^2} \tag{2.11}$$

where H_{a} is the Hamaker constant, and h is the separation of surfaces along the line of the centers of particles i and j. To prevent $\mathbf{F}^{\mathbf{v}}_{\mathrm{ij}}$ becoming infinity when h goes to zero a minimum separation distance $h_{\min}$ is considered. The Hamaker constant is related to the surface energy density by [22]:

$$\mathbf{H}_{\mathbf{a}} = 24\pi e_{surface} h_{\min}^2 \tag{2.12}$$

2.2.3 Cohesive force

The cohesive force is included in both Modified Gran-Hertz-History model and Gran-Hooke-History model. For the cohesive force, Johnson-Kendall-Roberts (JKR) model [23] is used to estimate the cohesive behavior of the particles. In this model, the normal cohesive force between two particles is proportional to the area of overlap between the particles.

$$\left|\mathbf{F}\right| = e_{surface} A \tag{2.13}$$

where $e_{surface}$ is the surface energy density and A is the particle contact area. For sphere-sphere contact [24], contact area A is evaluated by,

$$A = \frac{\pi}{4} \times \frac{(dist - Rad_i - Rad_j)(dist + Rad_i - Rad_j)(dist - Rad_i + Rad_j)(dist + Rad_i + Rad_j)}{dist^2} \tag{2.14}$$

where *dist* is the central distance between the i and j particles. Rad_i and Rad_j are the radius of the i^{th} and j^{th} particle, respectively.

2.2.4 Torques

The torque due to tangential contact force and the torque due to rolling friction are calculated in the same way for both models [25]:

$$\mathbf{Trq^t_{ij}} = \mathbf{Rad_i} \times \mathbf{F^t_{ij}} \tag{2.15}$$

$$\mathbf{Trq^r_{ij}} = \mu_r \bar{R} K_n \xi_n \frac{\boldsymbol{\omega}_{\mathbf{ij}} \cdot \mathbf{t_{ij}}}{\left|\boldsymbol{\omega}_{\mathbf{ij}}\right|} \mathbf{t_{ij}} \tag{2.16}$$

where $\boldsymbol{\omega}_{\mathbf{ij}} = \boldsymbol{\omega}_{\mathbf{i}} - \boldsymbol{\omega}_{\mathbf{j}}$ is the relative angular velocity.

2.3 The Integration Scheme

For particle simulation using DEM the popular explicit Velocity Verlet scheme is used for time integration of the equation of motions. The accuracy of the integration scheme is of second order. Time integration operation for the n-th time step is as follows:

$$acc_i^n = \frac{F_i^n}{m_i} \tag{2.17}$$

$$u_i^{n+1/2} = u_i^{n-1/2} + acc_i^n \Delta t \tag{2.18}$$

$$x_i^{n+1} = x_i^n + u_i^{n+1/2} \Delta t \tag{2.19}$$

Here x is the displacement, v is the velocity, a is the acceleration, Δt is the time step and n indicates the time step position.

2.3.1 Numerical Stability

Explicit time integration schemes suffer from numerical stability that depends on time step, Δt despite enjoying higher computational efficiency for discontinuous and large

systems than implicit ones. The time-step must be sufficiently small to prevent any unrealistic overlap [26] during collision of particles. In this work, the time step of 1×10^{-8} s is found to be sufficient for all simulation cases. For each particle, a cutoff velocity is also considered below which the particles are deemed completely stationary. This velocity is 1×10^{-8} m/s.

2.4 Physical Model

For each simulation, 4,500 particles are allowed to settle in a box with dimensions 6 mm × 6 mm. The particles are inserted such that they have no initial contact among them. The initial porosity of the system is kept constant at 0.75. **Figure 2-1** shows the initial state of Gaussian particle packing. The particles are allowed to fall down due to gravity and then collide with other particles or with the boundaries. In this work, all six sides of the simulation box are considered as physically stationary.

Sixty scenarios are studied in this work: five different mean radius (75μm, 85 μm, 100 μm, 110 μm, and 120 μm) and three different size distributions (mono-sized, uniform and Gaussian) for two contact models (Modified Gran-Hertz-History model and Gran-Hooke-History model) with and without cohesion. It should be noted that the deformation calculation is very important for packing simulation since the oversimplified model of calculating overlap distance is always the main reason that leads to the simulation crash by introducing unrealistic energy. Two basic rules are applied to these packing simulations: one is that particles are always considered as rigid body even though a deformation is considered by the chosen model, and the other is that the critical central distance is set for particle deformation. The critical distance is 1.01(d1+d2)/2 where d1 and d2 are the diameters of the two particles. It means when the central distance of two

particles is less than the critical distance the two particles are considered to be in direct contact [27].

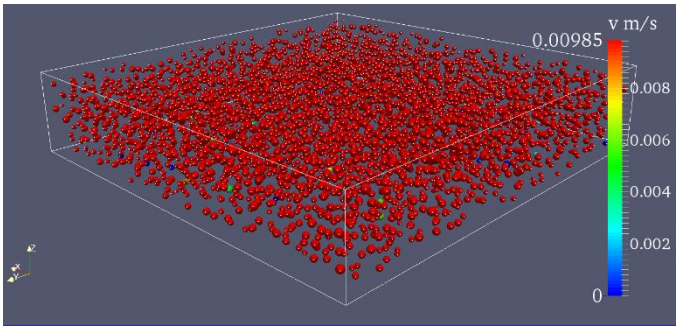

(a) Particles at t = 1×10^{-8} sec

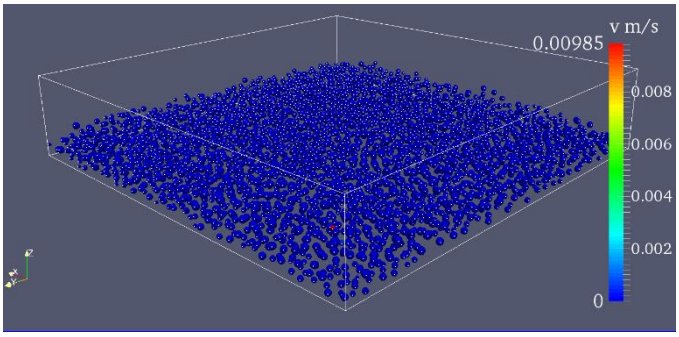

(b) Particles at t = 0.2 sec

Figure 2-1 Initial and final structure for Gaussian particles from Modified Gran-Hertz-History model with cohesion.

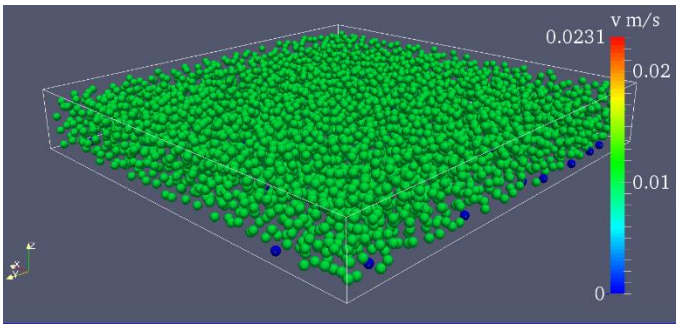

(a) Particles at t = 1×10^{-8} sec

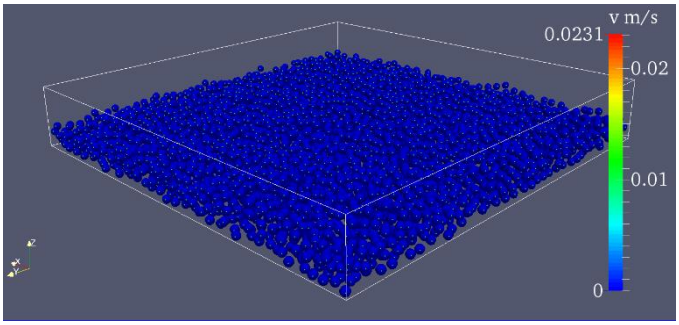

(b) Particles at t = 0.2 sec

Figure 2-2 Initial and final packing structure for mono-sized particles from Modified Gran-Hertz-History model with cohesion.

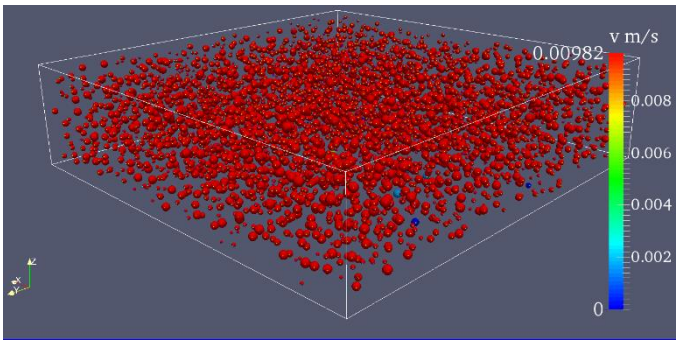

(a) Particles at t = 1×10^{-8} sec

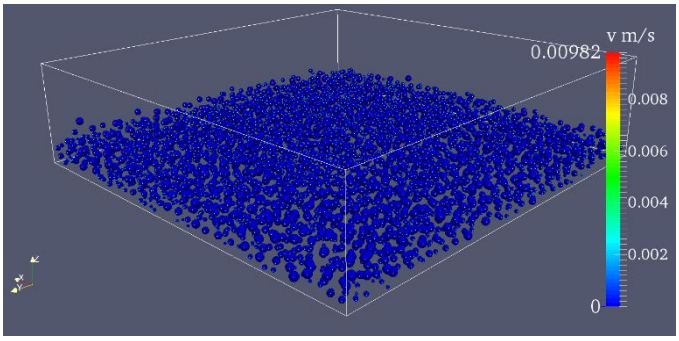

(b) Particles at t = 0.2 sec

Figure 2-3 Initial and final packing structure for uniform size particles from Modified Gran-Hertz-History with cohesion.

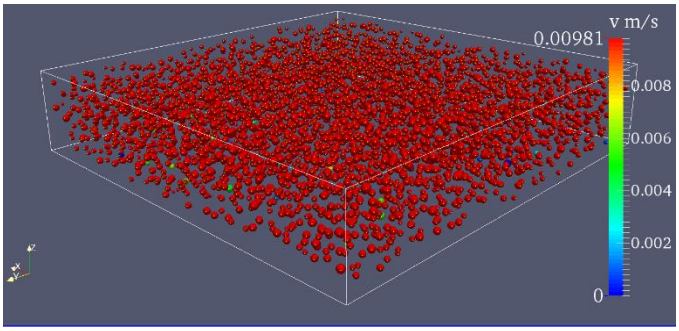

(a) Particles at t = 1×10^{-8} sec

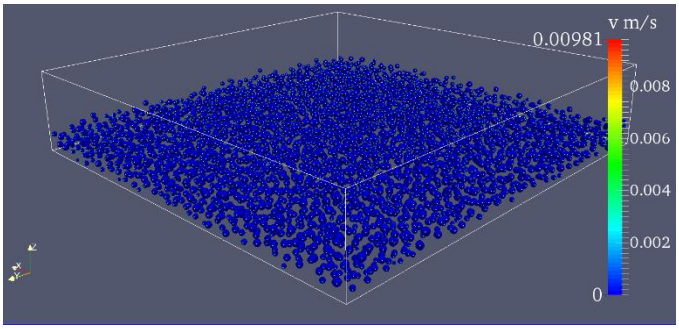

(b) Particles at t = 0.2 sec

Figure 2-4 Initial and final structure for Gaussian particles from Gran-Hooke-History model with cohesion.

2.5 Material Properties

Table 2-1 Values of the parameters used in the simulation process

Parameters	Values
Particle density ρ	7870 kg/m^3
Young's modulus E	200×10^9 N/m^2
Restitution coefficient e_{res}	0.75
Sliding friction coefficient μ_s	0.42
Rolling friction coefficient μ_r	2×10^{-4}
Poison ratio σ^p	0.29
Hamaker constant, H_a	21.1×10^{-20} J
Minimum separation distance, h_{min}	1×10^{-10} m
Surface energy density, $e_{surface}$	0.280 J/m^2

2.6 Results and Discussion

2.6.1 Porosity and Coordination Number

Table 2-2 Porosity and coordination number for Modified Gran-Hertz-History model

Radius	Porosity			Coordination number		
	Mono-sized	Uniform	Gaussian	Mono-sized	Uniform	Gaussian
75μm	0.615	0.695	0.713	4.04	3.50	3.14
85μm	0.656	0.685	0.660	4.84	4.49	4.01

100μm	0.583	0.615	0.637	5.27	5.29	5.14
110μm	0.575	0.505	0.557	5.41	5.56	5.37
120μm	0.485	0.574	0.487	5.36	5.46	5.45

Table 2-3 Porosity and coordination number for Gran-Hooke-History model

Radius	Porosity			Coordination number		
	Mono-sized	Uniform	Gaussian	Mono-sized	Uniform	Gaussian
75μm	0.599	0.695	0.724	4.00	3.59	3.11
85μm	0.656	0.685	0.643	4.83	4.50	4.00
100μm	0.566	0.615	0.476	5.25	5.25	5.13
110μm	0.525	0.505	0.591	5.50	5.55	5.43
120μm	0.476	0.574	0.651	5.33	5.47	5.36

Table 2-4 Porosity and coordination number for Modified Gran-Hertz-History model without cohesion

Radius	Porosity			Coordination number		
	Mono-sized	Uniform	Gaussian	Mono-sized	Uniform	Gaussian
75μm	0.454	0.485	0.505	4.05	3.55	3.46
85μm	0.436	0.478	0.493	4.85	4.48	4.08
100μm	0.415	0.422	0.439	5.28	5.27	5.12
110μm	0.430	0.421	0.437	5.33	5.47	5.35
120μm	0.429	0.426	0.438	5.43	5.50	5.38

Table 2-5 Porosity and coordination number for Gran-Hooke-History model without cohesion

Radius	Porosity			Coordination number		
	Mono-sized	Uniform	Gaussian	Mono-sized	Uniform	Gaussian
75μm	0.407	0.483	0.458	4.01	3.52	3.60
85μm	0.439	0.460	0.472	4.82	4.44	4.00

100μm	0.419	0.427	0.453	5.28	5.31	5.13
110μm	0.427	0.452	0.448	5.37	5.44	5.33
120μm	0.419	0.435	0.436	5.36	5.55	5.46

Table 2-6 Magnitude of mean net contact force (N) for Modified Gran-Hertz-History model

Radius	Cohesion			No Cohesion		
	Mono-sized	Uniform	Gaussian	Mono-sized	Uniform	Gaussian
75μm	1.91×10^{-7}	3.00×10^{-7}	2.20×10^{-6}	1.94×10^{-7}	2.87×10^{-7}	2.25×10^{-7}
85μm	3.75×10^{-7}	4.86×10^{-7}	4.13×10^{-7}	3.76×10^{-7}	4.74×10^{-7}	4.22×10^{-7}
100μm	8.50×10^{-7}	1.07×10^{-6}	9.22×10^{-7}	8.60×10^{-7}	1.03×10^{-6}	9.09×10^{-7}
110μm	1.41×10^{-6}	1.59×10^{-6}	1.52×10^{-6}	1.41×10^{-6}	1.59×10^{-6}	1.50×10^{-6}
120μm	2.30×10^{-6}	2.41×10^{-6}	2.30×10^{-6}	2.23×10^{-6}	2.40×10^{-6}	2.30×10^{-6}

Table 2-7 Magnitude of mean net contact force (N) for Gran-Hooke-History model

Radius	Cohesion			No Cohesion		
	Mono-sized	Uniform	Gaussian	Mono-sized	Uniform	Gaussian
75μm	1.96×10^{-7}	2.93×10^{-7}	2.23×10^{-7}	2.00×10^{-7}	2.85×10^{-7}	2.23×10^{-7}
85μm	3.92×10^{-7}	4.94×10^{-7}	4.30×10^{-7}	3.94×10^{-7}	5.46×10^{-7}	4.10×10^{-7}
100μm	8.75×10^{-7}	1.00×10^{-6}	9.28×10^{-7}	8.61×10^{-7}	1.03×10^{-6}	8.87×10^{-7}
110μm	1.50×10^{-6}	1.59×10^{-6}	1.45×10^{-6}	1.39×10^{-6}	1.58×10^{-6}	1.49×10^{-6}
120μm	2.24×10^{-6}	2.35×10^{-6}	2.31×10^{-6}	2.19×10^{-6}	2.44×10^{-6}	2.48×10^{-6}

Figure 2-5 and **Figure 2-6** present the porosities and coordination numbers for different cases. It can be seen that the porosity decreases along with the increasing particle radius for all distributions when cohesive forces are considered. Similar trend was observed in the work of previous researchers [28]. This decrease in porosity with increase in radius is expected since with increase of radii or masses of the particles the initial supplied energy (gravitational potential) also increases. So the effect of cohesion in the packing of particles decreases and the porosity values become closer to that for Random Loose Packing [29, 30]. This also explains the decrease in differences between different size distributions in terms of porosity when the radius increases. Among the three distributions considered, Gaussian distribution has the highest porosity and mono-

size has the lowest. The porosity values for the two models, Modified Gran-Hertz and Gran-Hooke are slightly different but both show the same trend. As for the non-cohesion case porosity also decreases with increase in particle radius, but the porosity values are much smaller. **Figure 2-5** also shows that the rate of decrease of porosity with radius for non-cohesion case is much smaller. For mono-sized distribution without cohesion, porosity remains almost constant for both Modified Gran-Hertz-History model and Gran-Hooke-History model. Since there is no cohesion the dissipative forces are smaller and particles can pack more closely. Again the difference between the two models in non-cohesion cases is very small. For the coordination number, the trends for three distributions with cohesion are similar. It can be observed that the coordination number increases as particle radius increases which is exactly the opposite of the trend of porosity. Unlike porosity, Gaussian distribution now has the lowest coordination number and mono-size distribution has the highest. Interestingly, it is found that there is no significant change in coordination number whether or not cohesion is included. However, one can expect that coordination number should be smaller when there is no cohesion (porosity is larger). This can be explained as follows. When there is cohesion, particles tend to clump together and form clusters. These clusters have void spaces in them. Due to this formation of clusters in some region particles have high coordination number and in some region the coordination number is small. The coordination numbers given in **Table 2-2** and **Figure 2-6** are average of coordination numbers for all particles. It can be seen that the coordination numbers for cohesion and non-cohesion cases are similar.

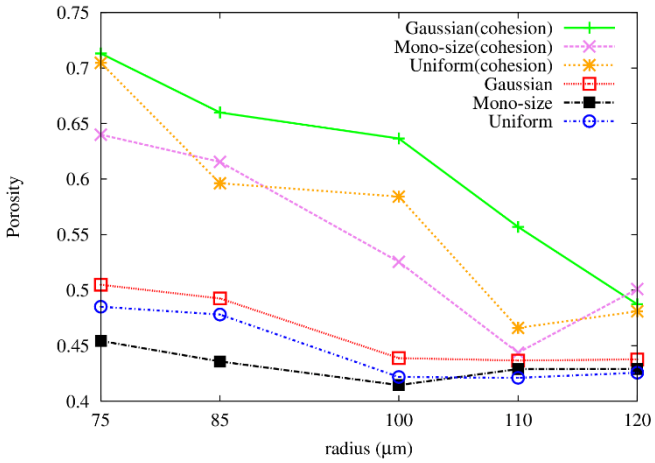

(a) Modified Gran-Hertz-History Model

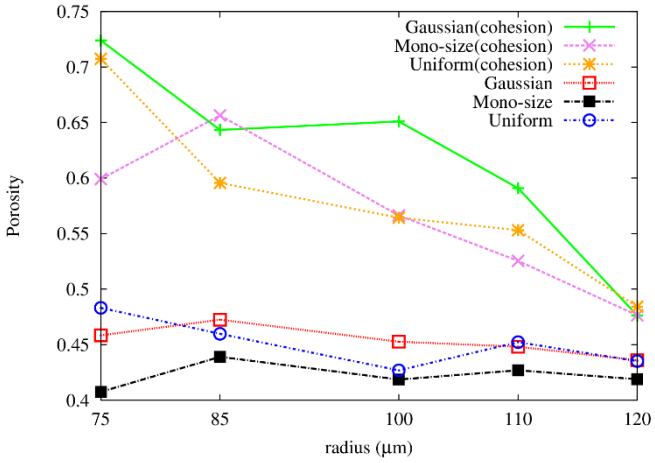

(b) Gran-Hooke-History Model

Figure 2-5 Effect of porosity with particle size and distribution

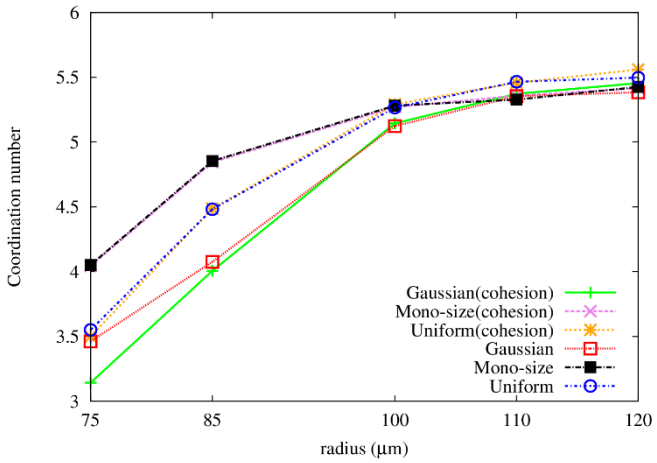

(a) Modified Gran-Hertz-History Model

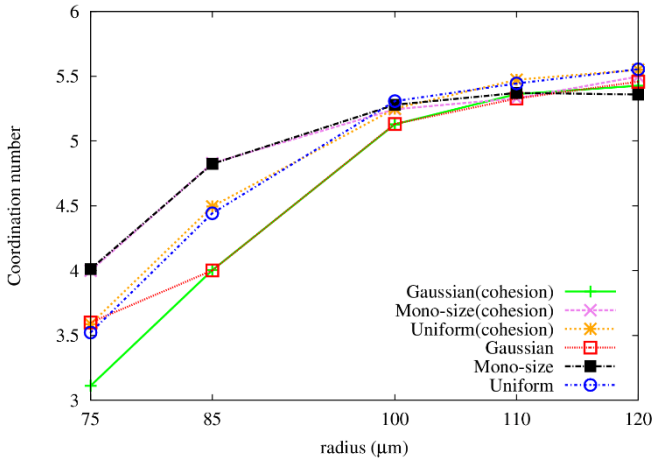

(b) Gran-Hooke-History Model

Figure 2-6 Effect of coordination number with particle size and distribution

2.6.2 Radial Distribution Function

Figure 2-7-11 show the RDF for particle systems with mean radius of 75 μm, 85μm, 100 μm, 110 μm and 120 μm and associated with three different size distributions (mono-sized, uniform and Gaussian). For the cases where the particles have the same radius, three main apparent peaks appear. The first peak is sharply at $2r$ which is for the initial one to one contact, the second and the third are at around $2\sqrt{2}r$ and $4r$, respectively

which corresponds to the two characteristic particle contact types, namely edge-sharing-in-plane equilateral triangle and three particles centers in a line (the three contact types are illustrated in Figure 2-7 (a)). The second and third peaks merge into a single second peak for other distributions. The particle systems with mono-size distribution usually have the highest peak values among all three cases. The peak values for Hertz model are close to that for Hooke model. Also the peak values of RDF are almost same for cohesion and non-cohesion cases.

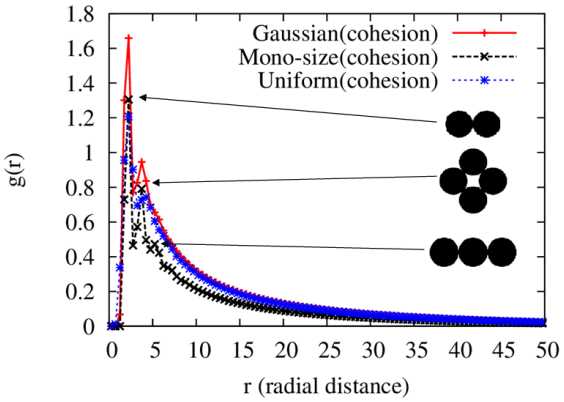

(a) Modified Gran-Hertz-History with cohesion

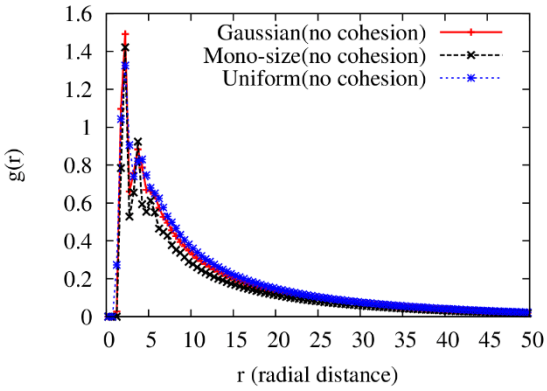

(b) Modified Gran-Hertz-History without cohesion

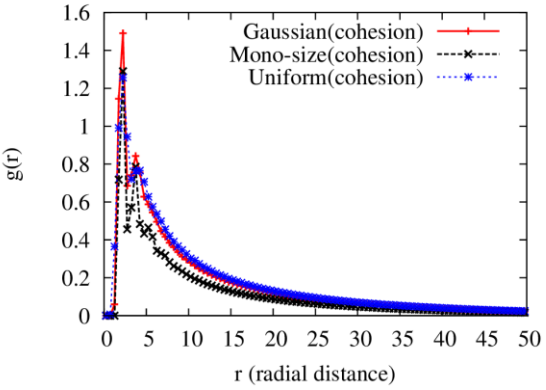

(c) Gran-Hooke-History with cohesion

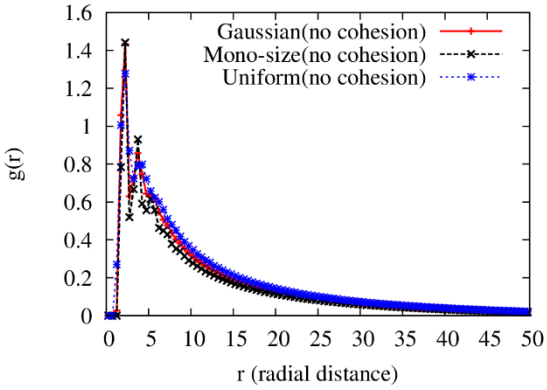

(d) Gran-Hooke-History without cohesion

Figure 2-7 RDF for particles with 75 μm radius

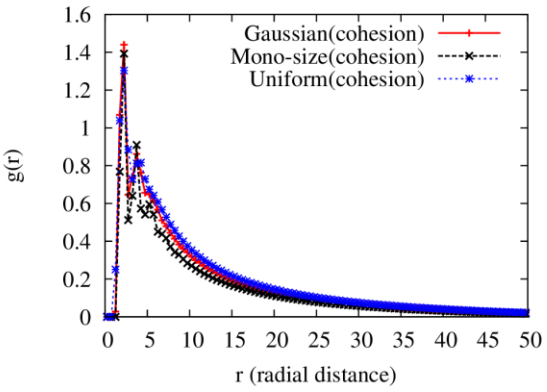

(a) Modified Gran-Hertz-History with cohesion

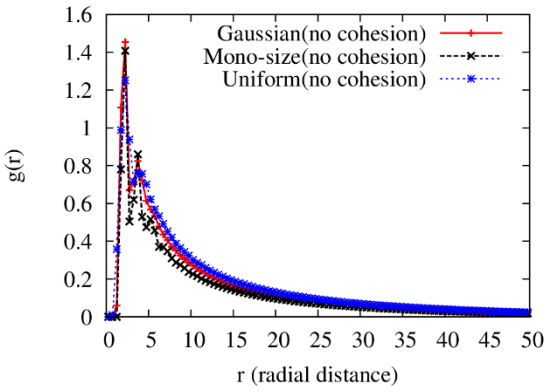

(b) Modified Gran-Hertz-History without cohesion

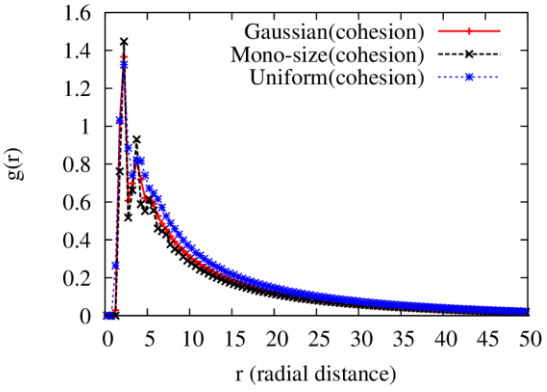

(c) Gran-Hooke-History with cohesion

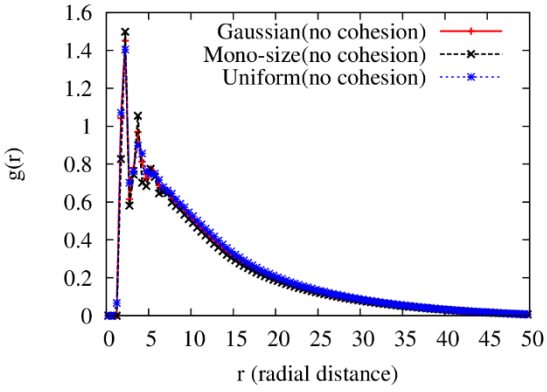

(d) Gran-Hooke-History without cohesion

Figure 2-8 RDF for particles with 85μm radius

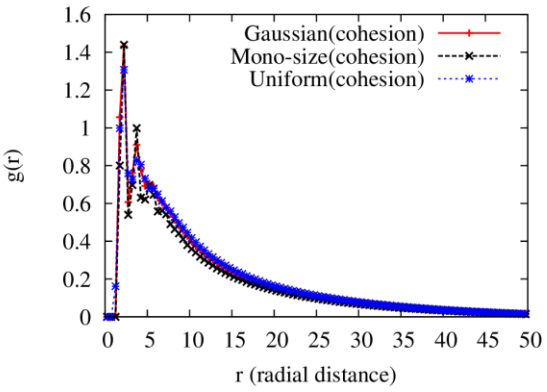

(a) Modified Gran-Hertz-History with cohesion

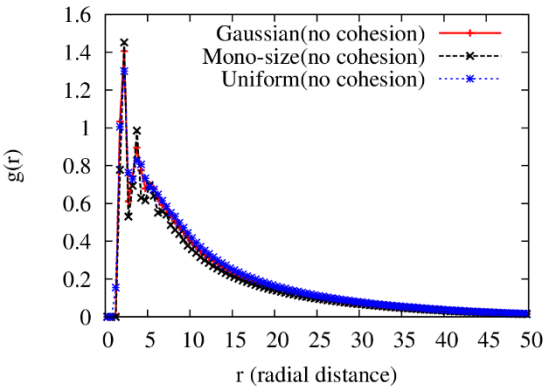

(b) Modified Gran-Hertz-History without cohesion

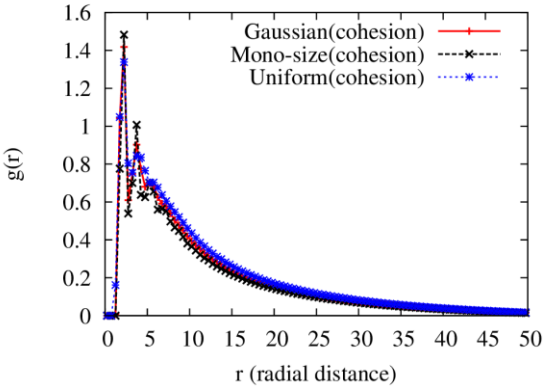

(c) Gran-Hooke-History with cohesion

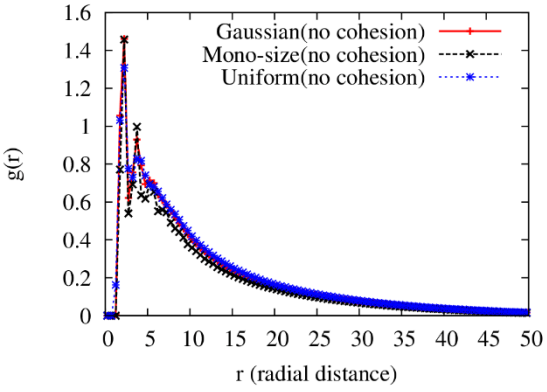

(d) Gran-Hooke-History without cohesion

Figure 2-9 RDF for particles with 100 μm radius

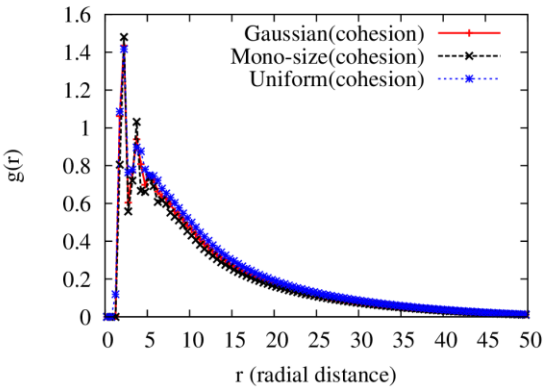

(a) Modified Gran-Hertz-History with cohesion

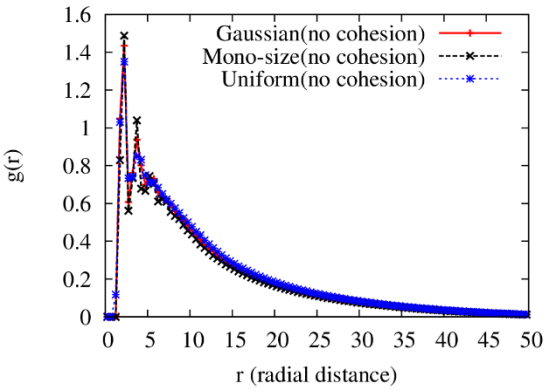

(b) Modified Gran-Hertz-History without cohesion

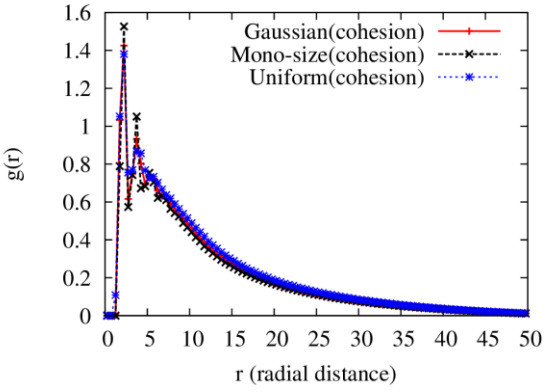

(c) Gran-Hooke-History with cohesion

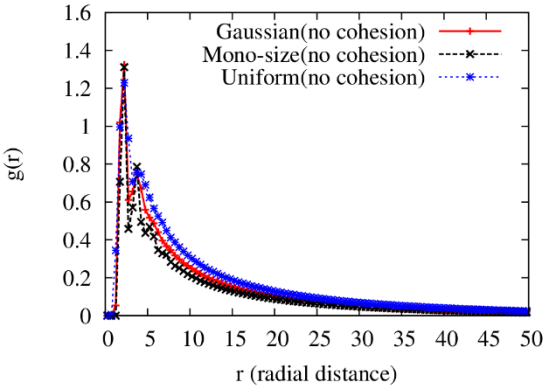

(d) Gran-Hooke-History without cohesion

Figure 2-10 RDF for particles with 110μm radius

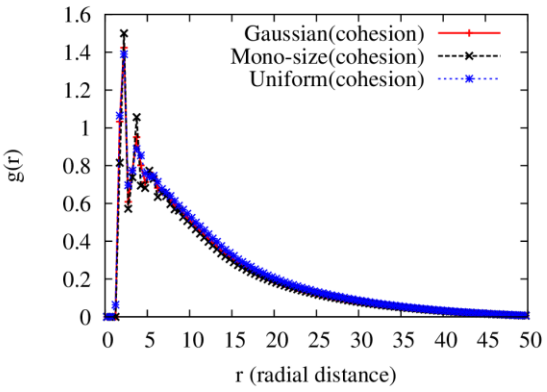

(a) Modified Gran-Hertz-History with cohesion

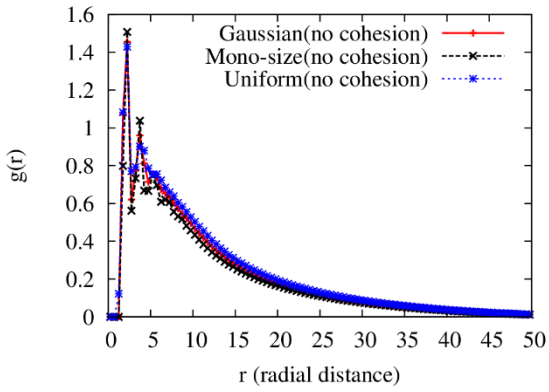

(b) Modified Gran-Hertz-History without cohesion

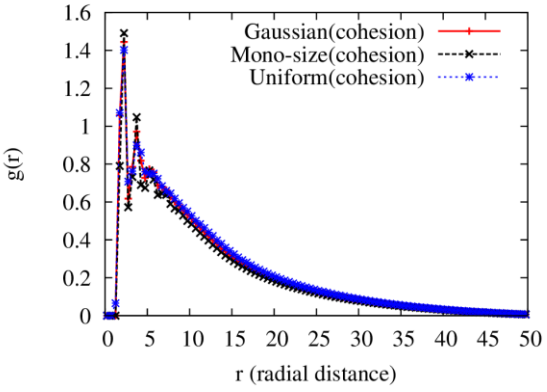

(c) Gran-Hooke-History with cohesion

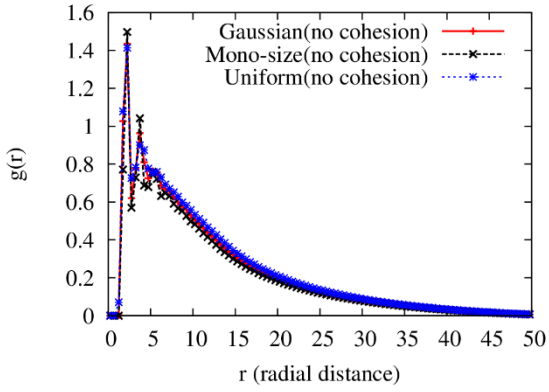

(d) Gran-Hooke-History without cohesion

Figure 2-11 RDF for particles with 120μm radius

2.6.3 Force Distribution

Figure 2-12-14 show the force distribution results after the particles are completely packed for particle systems with mean radius of 75μm. The force distribution graphs for other particle radii look similar. For same distribution the counts for each force magnitude are not exactly the same but close. However, as the particle radius increases, the force magnitudes increase as a response.

Table 2-6 and **Table 2-7** give the mean net force for all the cases when the particles are finally packed. It has to be pointed out that the resultant force here does not represent gravity, since effect of gravity is small (of the order of 10^{-12} N). It can also be observed that the net force does not vary much even when the cohesion is included. The mean net force increases with the size of the particles, and it can also be seen that this force has the largest value if the particle size follows uniform distribution. Particles with Gaussian distribution have the secondary magnitude of force, while the mono sized particles have the smallest net force. The difference in magnitude of mean net force between the two different contact models is negligible.

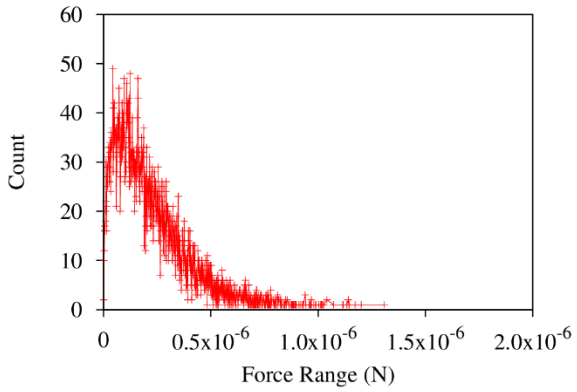

(a) Modified Gran-Hertz-History with cohesion

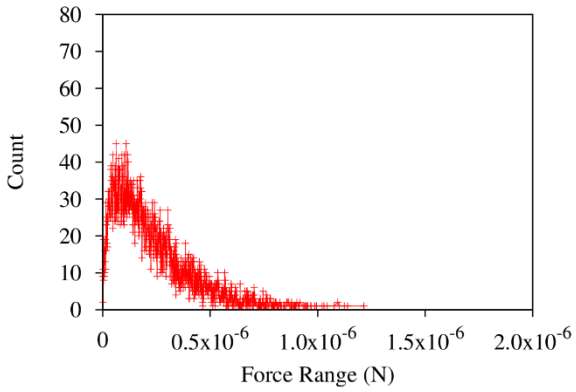

(b) Modified Gran-Hertz-History without cohesion

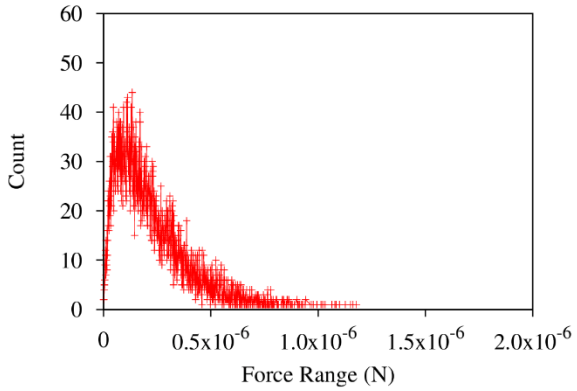

(c) Gran-Hooke-History with cohesion

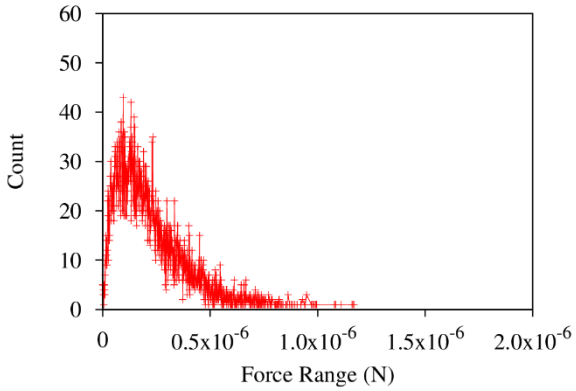

(d) Gran-Hooke-History without cohesion

Figure 2-12 Force distribution for particles with 75 μm radius and Gaussian distribution

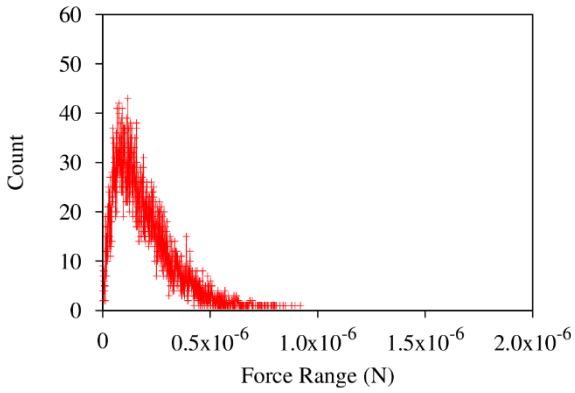

(a) Modified Gran-Hertz -History with cohesion

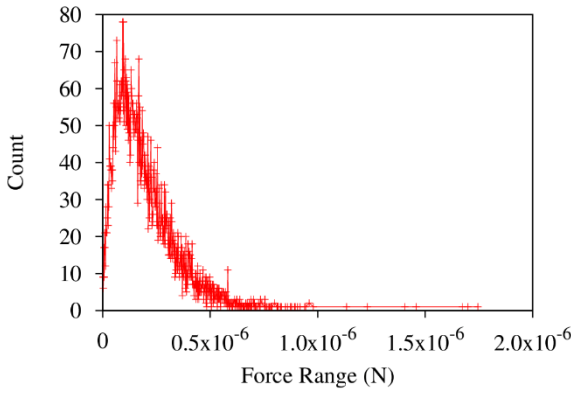

(b) Modified Gran-Hertz-History without cohesion

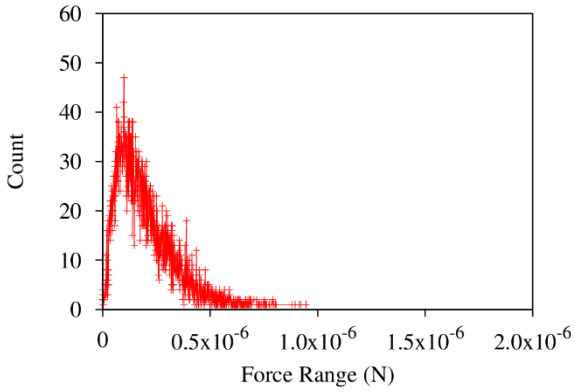

(c) Gran-Hooke -History with cohesion

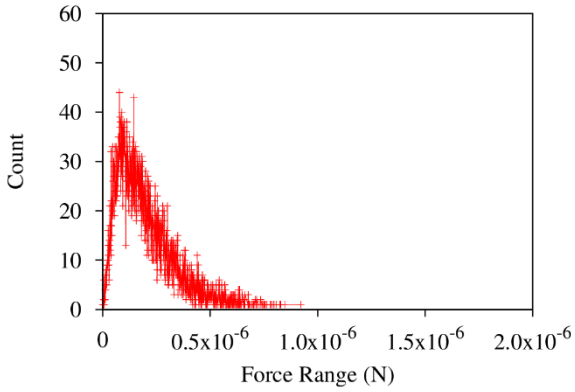

(d) Gran-Hooke -History without cohesion

Figure 2-13 Force distribution for particles with 75 μm radius and mono-size distribution

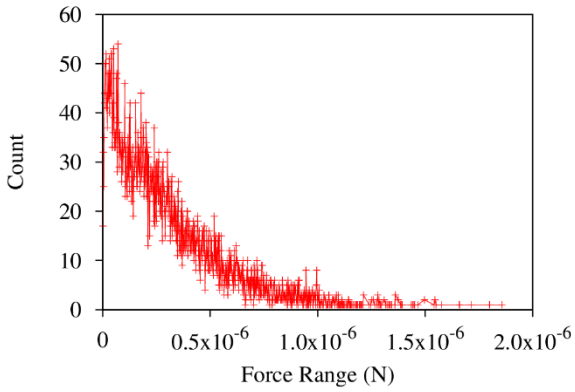

(a) Modified Gran-Hertz -History with cohesion

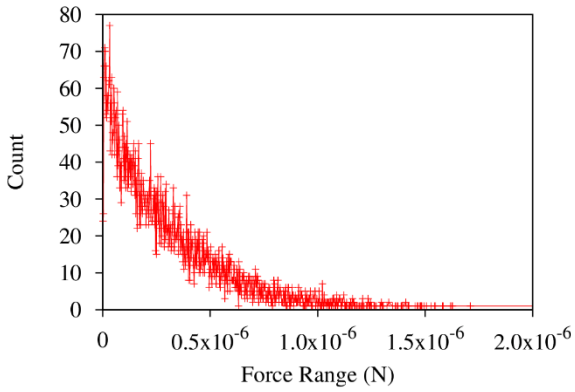

(b) Modified Gran-Hertz -History without cohesion

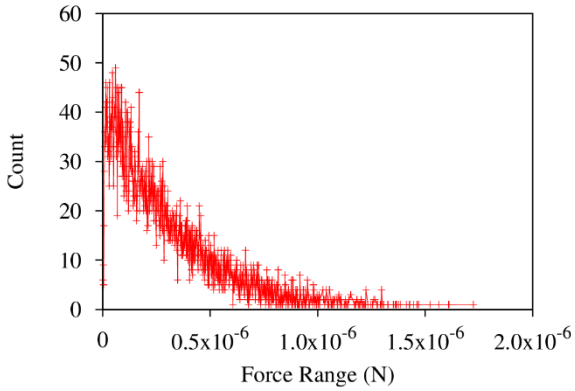

(c) Gran-Hooke-History with cohesion

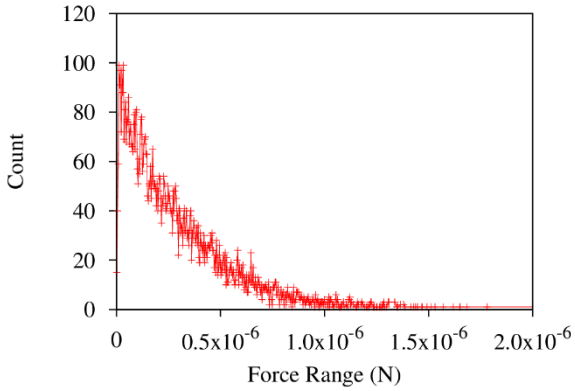

(d) Gran-Hooke-History without cohesion

Figure 2-14 Force distribution for particles with 75 μm radius and uniform distribution

2.6.4 Comparison between contact models

By comparing the two models, Modified Gran-Hertz-History and Gran-Hooke-History, it can be seen that the difference between them is not significant in terms of porosity, coordination number and mean net force. Both of these models assume that the particles are viscoelastic and have a stiffness term and dissipation term. As pointed out by [31] the linear Gran-Hooke model can be as accurate as the non-linear Modified Gran-Hertz model if the stiffness constants, K_n and K_t, and damping coefficients, γ_n and γ_t, are evaluated carefully. In this study, even though cohesion is included, the results obtained

from the two models are still close. Van der Waals force included in the Modified Gran Hertz model did not seem to play a great role in the packing process. This might be because particle sizes are too large for van der Waals force to take effect. When the efficiency of the two models are considered, the simulations with the Gran-Hooke-History model ran faster than the simulation with the Modified Gran-Hertz-History model. So the linear Gran-Hooke-History model is more efficient than the Modified Gran-Hertz-History model.

2.7 Conclusion

A study on packing structures of particle system with different radii and size distributions using two different models are carried out by the Discrete Element Method. The simulation results including RDF and force distribution, porosity and coordination number are presented. It was observed that the particles with Gaussian distribution always have the lowest packing density while the particles with uniform size distribution have the medium packing density and mono-sized particles normally have the highest packing density. For the particles packing under cohesive effect, size distributions result in the same tendency of packing density but has much less variation with particle size. Coordination number is not affected by cohesion significantly but particle size and size distribution do influence the result. The differences in porosity, coordination number, RDF and magnitude of mean net force between the two models used are not substantial which show that any of the models can be used for simulation of particle packing. However when efficiency is considered the Gran-Hooke-History model is found to be more efficient than the Modified Gran-Hertz-History model. Therefore, Gran-Hooke-History model can be the model of choice for simulating micro-sized particles.

3 SMOOTHED PARTICLE HYDRODYNAMICS SIMULATION OF GRANULAR SYSTEM UNDER CYCLIC COMPRESSIONS

3.1 Introduction

This chapter presents the study on the states of two-dimensional granular materials subjected to consecutive isotropic jamming cycles. The granular system is cyclically and isotropically compressed with small strain steps, starting from a packing fraction below jamming, to a packing fraction above jamming. The Smoothed Particle Hydrodynamics (SPH) method used to carry out the numerical study is presented in the next section along with the description of the physical model. The evolution of global stress in the granular system and the effect of local microstructure is discussed in the subsequent sections.

3.2 Methods and Physical Models

In this study the granular materials are simulated using the Smoothed Particle Hydrodynamics (SPH) method [32-35]. SPH is a meshless method where the governing equations are solved by discretizing the granular particles into a finite set of SPH particles or integration points. The field variables such as density and velocity at a point of interest are calculated by integrating over the SPH particles. The SPH method can handle large deformation and has been applied to hyper-velocity impact [34], explosion [36] and fluid dynamics [37] problems. When SPH is applied to high velocity impact problems exact detection of boundary and contact forces can be ignored because of their insignificant contribution. However, for low velocity impact or small deformation, as discussed by previous researchers [38], several problems can arise without proper boundary treatment. Some of them include ghost stress, which arises due to incorrect

inclusion of boundary particles within a smoothing length, false tensile force during separation and normalization of kernel not satisfied. To avoid such problems, a method to detect boundary SPH particles and a contact force model is developed and employed for studying granular materials. This method was originally proposed by [38] using a contact mechanics model developed for finite element method. In this section the SPH method will be described first, followed by discussion on some modifications added to provide better results and the kinematic contact algorithm for the granular particles.

As discussed earlier, in SPH field quantities at a point are obtained by integral interpolation of neighboring points.

$$f(\mathbf{r}) = \int f(\mathbf{r}')\ \delta(\mathbf{r}-\mathbf{r}')\,\mathrm{d}\mathbf{r}' \tag{3.1}$$

where f (r) is a field quantity determined at the position vector r, while δ is the Dirac delta function. The above equation can be approximated by

$$f(\mathbf{r}) = \int f(\mathbf{r}')\ W(\mathbf{r}-\mathbf{r}', h)\,\mathrm{d}\mathbf{r}' \tag{3.2}$$

where W (**r – r'**, h) is called the kernel or smoothing function and f (r) is now determined by weighted interpolation of surrounding field quantities. The smoothing length, h defines the domain of influence of the kernel function, W (**Figure 3-1**). The kernel function, W is chosen such that it satisfies two conditions. The first is the normalization condition that states,

$$\int W(\mathbf{r}-\mathbf{r}', h)\,\mathrm{d}\mathbf{r}' = 1 \tag{3.3}$$

The integration of the smoothing function should produce unity.

The second condition is the Delta function property which states that the kernel function approaches the delta function as smoothing length, h approaches zero.

$$\lim_{h\to 0} W\left(\mathbf{r}-\mathbf{r}',h\right)\mathrm{d}\,\mathbf{r}' = \delta\left(\mathbf{r}-\mathbf{r}'\right) \tag{3.4}$$

For numerical efficiency a third condition is imposed on the kernel function which is the compact condition.

$$W\left(\mathbf{r}-\mathbf{r}',h\right) = 0 \qquad \text{when} \quad \left|\mathbf{r}-\mathbf{r}'\right| > kh \tag{3.5}$$

The quantity kh define the effective (non-zero) area of the smoothing function. This area is called the support domain. The parameter k is chosen such that sufficient amount of the function falls within the support domain and the error due to interpolation is small.

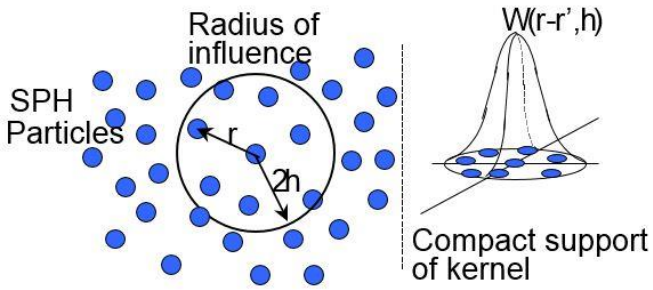

Figure 3-1 The support domain of the smoothing function, W

By discretizing the entire system into a finite number of particles that carry individual mass and occupy individual space, the integral equation can be approximated by summation interpolant.

$$f_i \approx \sum_{j=1}^{N} f\left(\mathbf{r}_j\right)\, W\left(\mathbf{r}-\mathbf{r}_j,h\right)\frac{m_j}{\rho_j} \tag{3.6}$$

where m_j and ρ_j are the mass and density of particle j at $\mathbf{r}_j$. The gradient and divergence of *f* is given as

$$\nabla f_i \approx \sum_{j=1}^{N} f\left(\mathbf{r}_j\right)\, \nabla_i W\left(\mathbf{r}-\mathbf{r}_j,h\right)\frac{m_j}{\rho_j} \tag{3.7}$$

$$\nabla \bullet \mathbf{f}_i \approx \sum_{j=1}^{N} \mathbf{f}\left(\mathbf{r}_j\right) \bullet \nabla_i W\left(\mathbf{r}-\mathbf{r}_j, h\right) \frac{m_j}{\rho_j} \tag{3.8}$$

The above SPH formulations are used to discretize the governing equations.

3.3 Equations of motion

The mass, momentum and energy conservation equations come from continuum mechanics model and are given as:

$$\frac{D\rho}{Dt} = -\rho \frac{\partial u^\alpha}{\partial x^\alpha} \tag{3.9}$$

$$\frac{Du^\alpha}{Dt} = \frac{1}{\rho} \frac{\partial \sigma^{\alpha\beta}}{\partial x^\beta} \tag{3.10}$$

$$\frac{De}{Dt} = \frac{\sigma^{\alpha\beta}}{\rho} \frac{\partial u^\alpha}{\partial x^\beta} \tag{3.11}$$

where ρ the density, u^α the velocity component, $\sigma^{\alpha\beta}$ the total stress tensor, and e is the specific internal energy.

The SPH approximation for mass, momentum and energy equation take the following form [39],

$$\frac{D\rho_i}{Dt} = \sum_{j=1}^{N} m_j \left(u_i^a - u_j^a\right) \frac{\partial W_{ij}}{\partial x_i^\alpha} \tag{3.12}$$

$$\frac{Du_i^\alpha}{Dt} = \sum_{j=1}^{N} m_j \left(\frac{\sigma_i^{\alpha\beta}}{\rho_i^2} + \frac{\sigma_j^{\alpha\beta}}{\rho_j^2} \right) \frac{\partial W_{ij}}{\partial x_i^\beta} \tag{3.13}$$

$$\frac{De_i}{Dt} = -\frac{1}{2} \sum_{j=1}^{N} m_j \left(\frac{\sigma_i^{\alpha\beta}}{\rho_i^2} + \frac{\sigma_j^{\alpha\beta}}{\rho_j^2} \right) \left(u_i^a - u_j^a\right) \frac{\partial W_{ij}}{\partial x_i^\beta} \tag{3.14}$$

where m is the mass of individual particle and W_{ij} is the kernel function. Several different kernel functions have been used in the SPH literature. The most popular one is the cubic spline function proposed by [40], which has the following form:

$$W(R,h) = \alpha_d \times \begin{cases} \frac{2}{3} - R^2 + \frac{1}{2}R^3 & 0 \le R < 1 \\ \frac{1}{6}(2-R)^3 & 1 \le R < 2 \\ 0 & R > 2 \end{cases} \tag{3.15}$$

where α_d is the normalization factor which is $15/7\pi h^2$ in two-dimension and R is the distance between particles *i* and *j* normalized as $R = r/h$. Unlike DEM where the contact forces are the main simulation variable and stress within particles are unknown, the SPH solution produces density, velocity, stress, and strain at each timestep directly. Constitutive models for stress and strain for actual materials can also be directly implemented in the SPH method.

To improve the numerical stability of the SPH method certain terms are added to the discretized governing equations. They are the artificial viscosity term, which is added to the momentum equation, the artificial stress term also added to the momentum equation to prevent tensile instability and the velocity smoothing technique [33] to smooth out any unexpected numerical peaks in the velocity. They are discussed in the following sections.

3.3.1 Artificial Viscosity

In SPH literature a dissipative term, $\prod_{ij}$, which is also called artificial viscosity, is introduced into the governing equation to prevent large unphysical oscillation in the numerical solution and to improve numerical stability. The artificial viscosity is incorporated into the momentum equation in the following way:

$$\frac{Du_i^{\alpha}}{Dt} = \sum_{j=1}^{N} m_j \left(\frac{\sigma_i^{\alpha\beta}}{\rho_i^2} + \frac{\sigma_j^{\alpha\beta}}{\rho_j^2} - \prod_{ij} \delta^{\alpha\beta} \right) \frac{\partial W_{ij}}{\partial x_i^{\beta}} \tag{3.16}$$

The most widely applied artificial viscosity derived by Monaghan [41] is used in this paper.

$$\prod_{ij} = \begin{cases} \dfrac{-\alpha \bar{c}_{ij} \mu_{ij} + \beta \mu_{ij}^2}{\bar{\rho}_{ij}} & u_{ij} \cdot x_{ij} < 0 \\ 0 & u_{ij} \cdot x_{ij} \geq 0 \end{cases} \tag{3.17}$$

where

$$\mu_{ij} = h \frac{u_{ij} \cdot x_{ij}}{\left| r_{ij} \right|^2 + \varepsilon h^2}, \quad \bar{c}_{ij} = \frac{1}{2}\left(c_i' + c_j' \right), \quad \bar{\rho}_{ij} = \frac{1}{2}\left(\rho_i + \rho_j \right) \tag{3.18}$$

$$x_{ij} = x_i - x_j, \quad v_{ij} = u_i - u_j \tag{3.19}$$

In the above equation, α and β are constants and taken as unity, c' is the sound speed and ε is 0.01.

The energy equation takes the form of

$$\frac{De_i}{Dt} = -\frac{1}{2} \sum_{j=1}^{N} m_j \left(\frac{\sigma_i^{\alpha\beta}}{\rho_i^2} + \frac{\sigma_j^{\alpha\beta}}{\rho_j^2} - \prod_{ij} \delta^{\alpha\beta} \right) \left(u_i^a - u_j^a \right) \frac{\partial W_{ij}}{\partial x_i^{\beta}} \tag{3.20}$$

3.3.2 Tensile Instability

In SPH, for solid body deforming under tension numerical instability arises and material can fail unrealistically. This happens because under tension the SPH particles attract each other and tend to clump together. Monaghan [42] and Grey et al. [43] successfully introduced artificial stress method to overcome this problem of tensile

instability. Their method involves adding another term to the momentum equation. The additional term comes from the dispersion relations.

$$\frac{du_i}{dt} = \sum_j m_j \left(\frac{\sigma_i^{\alpha\beta}}{\rho_i^2} + \frac{\sigma_j^{\alpha\beta}}{\rho_j^2} - \Pi_{ij} + \left(R_i^{\alpha\beta} + R_j^{\alpha\beta} \right) f_{ij}^{\,n} \right) \frac{\partial W_{ij}}{\partial x_i^{\beta}} \tag{3.21}$$

where *n* is the exponent which depends on the smoothing kernel, f_{ij} is the repulsive force term which is given in terms of the kernels by [42] as:

$$f_{ij} = \frac{W_{ij}}{W\left(\Delta p, h\right)} \tag{3.22}$$

where Δp is the initial particle spacing. In this paper, *h* is assumed to be constant so that $W\left(\Delta p, h\right)$ is also constant. It is found that best result can be obtained by setting $h = 1.5\Delta p$. The [43] suggested a value of 4 for *n* for best result so that value is used in this work.

For the two-dimensional case used in this paper, the components of the artificial stress tensor $R_i^{\alpha\beta}$ for particle *i* in the reference coordinate system *(x, y)* are computed from the principal components $R_i'^{xx}$ and $R_i'^{yy}$ by the coordinate transformation:

$$R_i^{xx} = R_i'^{xx} \cos^2 \theta_i + R_i'^{yy} \sin^2 \theta_i \tag{3.23}$$

$$R_i^{yy} = R_i'^{xx} \sin^2 \theta_i + R_i'^{yy} \cos^2 \theta_i \tag{3.24}$$

$$R_i^{xy} = \left(R_i'^{xx} - R_i'^{yy} \right) \sin \theta_i \cos \theta_i \tag{3.25}$$

where the angle θ_i is defined as,

$$\tan 2\theta_i = \frac{2\sigma_i^{xy}}{\sigma_i^{xx} - \sigma_i^{yy}} \tag{3.26}$$

where σ_i^{xx}, σ_i^{yy} and σ_i^{xy} are components of stress tensor of particle *i* in the reference frame *(x, y)*. The diagonal components of the artificial stress tensor in principle axes are calculated as [43],

$$R_i'^{xx} = \begin{cases} -\dfrac{\varepsilon\sigma_i'^{xx}}{\rho_i^2} & if\ \sigma_i'^{xx} > 0 \\ 0 & otherwise \end{cases} \tag{3.27}$$

$$R_i'^{yy} = \begin{cases} -\dfrac{\varepsilon\sigma_i'^{yy}}{\rho_i^2} & if\ \sigma_i'^{yy} > 0 \\ 0 & otherwise \end{cases} \tag{3.28}$$

where ε is a constant and is taken as 0.3 which as suggested by [43] is the best value for elastic solid. $\sigma_i'^{xx}$ and $\sigma_i'^{yy}$ are the principal stresses of particle *i*. They are obtained as,

$$\sigma_i'^{xx} = \sigma_i^{xx}\cos^2\theta_i + 2\sin\theta_i\cos\theta_i\sigma_i^{xy} + \sigma_i^{yy}\sin^2\theta_i \tag{3.29}$$

$$\sigma_i'^{yy} = \sigma_i^{xx}\sin^2\theta_i - 2\sin\theta_i\cos\theta_i\sigma_i^{xy} + \sigma_i^{yy}\cos^2\theta_i \tag{3.30}$$

3.3.3 Velocity Smoothing

The velocities *v* of the particles obtained by time integration of the momentum equation are corrected in order to smooth out any unexpected numerical peaks. The correction is done by [33],

$$\hat{u}_i^{\alpha\beta} = u_i^{\alpha\beta} + \tilde{\varepsilon}\sum_{j=1}^{N}\frac{m_j}{0.5\left(\rho_i + \rho_j\right)}\left(u_j^{\alpha\beta} - u_i^{\alpha\beta}\right)W_{ij} \tag{3.31}$$

The corrected velocities are used to update the position of the particles, while the uncorrected velocities are used for time integration of the momentum equation at the following step.

3.3.4 Equations of State

Pressure, density and internal energy of a material are related by the equation of state of the system. In this paper the Mie-Gruneisen equation for solids [44] is used to calculate the pressure arising from the deformation of the material.

Table 3-1 gives the material properties and constants for Mie-Gruneisen EOS of lead.

The required equations are

$$p = \left(1 - \frac{1}{2}\Gamma\eta\right) p_H(\rho) + \Gamma\rho e \tag{3.32}$$

where

$$\eta = \frac{\rho}{\rho_0} - 1 \tag{3.33}$$

$$p_H(\rho) = \begin{cases} a_0\eta + b_0\eta^2 + c_0'\eta^3, & \eta > 0 \\ a_0\eta, & \eta < 0 \end{cases} \tag{3.34}$$

$$a_0 = \rho_0 c'^2 \tag{3.35}$$

$$b_0 = a_0\left[1 + 2(S-1)\right] \tag{3.36}$$

$$c_0 = a_0\left[2(S-1) + 3(S-1)^2\right] \tag{3.37}$$

Table 3-1 Material Properties

	ρ (g/cm^3)	c' (×10^4 m/s)	S	G (GPa)	E (GPa)	Γ
Lead	11.34	1.19	1.80	5.6	16	2.00

where ρ_0 is the density, c' is the speed of sound in the material, E and G are respectively bulk and shear moduli and S and Γ are material parameters needed to calculate the Mie-Gruneisen equation of state. The stress rate obtained from the constitutive relation must be invariant with respect to rigid body rotation when large deformation is involved. The Jaumann stress rate is adopted for this purpose as,

$$\dot{s}^{\alpha\beta} - s^{\alpha\gamma}\dot{R}^{\beta\gamma} - s^{\gamma\beta}\dot{R}^{\alpha\gamma} = 2G\dot{e}^{\alpha\beta} \tag{3.38}$$

where $\dot{R}^{\beta\gamma}$ is the rotation rate tensor defined as,

$$\dot{R}^{\beta\gamma} = \frac{1}{2}\left(\frac{\partial v^{\beta}}{\partial x^{\gamma}} - \frac{\partial v^{\gamma}}{\partial x^{\beta}}\right) \tag{3.39}$$

and $\dot{R}^{\alpha\gamma}$ has the same equation except β is replaced by α.

3.3.5 Contact Model

The contact model used here is that derived by [38] for SPH low velocity impact problem. They derived the weak form of the contact problem using the virtual work principal and solved it by penalty method that involves both a penetration and a penetration rate.

The SPH form of the variational equation for the contact problem is given by [38],

$$\sum_{i}^{N}\left[\dot{u}_i^{\alpha}\sum_{j\in M_i}\rho_i W_{ij}V_jV_i + \sum_{j\in M_i}\sigma_j^{\alpha\beta}\nabla W_{ij}V_jV_i + \sum_{j\in M_i}\left(\lambda_1\dot{p}_n + \lambda_2 p_n\right)\mathrm{n}_i W_{ij}A_1V_j\right]\delta u_i^{\alpha} = 0 \tag{3.40}$$

where M_i represents those particles within a distance 2h of a particle i, and A_i is the contact area. p_n is the penetration and $\dot{p}_n$ is the penetration rate. λ_1 denotes the penalty parameter for the penetration rate and λ_2 is the penalty parameter for the penetration. The inside of the bracket must be zero for allowable virtual velocity δu_i^{α}. Therefore the momentum equation for two bodies in contact can be written as [38],

$$m_i \dot{\mathrm{u}}_i = -\mathrm{F}_i^{\mathrm{int}} - \mathrm{F}_i^{con} \tag{3.41}$$

where

$$\begin{aligned} m_i &= \sum_{j \in M_i} \rho_i W_{ij} V_j V_i \\ \mathrm{F}_i^{\mathrm{int}} &= \sum_{j \in M_i} \sigma_j^{\alpha\beta} \nabla W_{ij} V_j V_i \\ \mathrm{F}_i^{con} &= \sum_{j \in M_i} \left(\lambda_1 \dot{p}_n + \lambda_2 p_n \right) \mathrm{n}_i W_{ij} A_i V_j \end{aligned} \tag{3.42}$$

3.3.6 Contact Force

The authors in [38] uses the one dimensional elastic wave theory to obtain the expression for contact force. Their equation for penalty parameters are,

$$\lambda_1 \dot{p} + \lambda_2 p = \left(\frac{\rho_j c_j'}{\rho_j c_j' + \rho_i c_i'} \rho_i c_i' \right) \dot{p} + \left(\frac{E_i E_j}{E_i + E_j} \frac{1}{d_o} \right) p \tag{3.43}$$

where ρ_i and ρ_j are densities of SPH particle i and j in contact, c_i' and c_j' are their respective sound speeds, E_i and E_j are their respective elastic moduli and d_o is the diameter of the SPH particles.

3.3.7 Contact Detection

To find the boundary particles a color parameter, $\tilde{\psi}_i$ is introduced for each SPH particles. A particle will be designated as a boundary particle if the summation of $\tilde{\psi}_i$ is less than 0.85~0.90 of the original index value [37, 38].

$$\tilde{\psi}_i \neq \sum_{j \in N(i)} \tilde{\psi}_j m_j W_{ij} / \rho_j \tag{3.44}$$

The boundary normal vector is obtained from the gradient of the color parameter.

$$n_i = \pm \left(\nabla \tilde{\psi} / \left| \nabla \tilde{\psi} \right| \right)_i \tag{3.45}$$

where

$$\left(\nabla \tilde{\psi} \right)_i = - \sum_{j \in M_i} \tilde{\psi}_j m_j \nabla W_{ij} / \rho_{ij} \tag{3.46}$$

The following criterion is used to detect the contact [38].

$$\left| \mathrm{r}_{ij} \right| \leq \sqrt{Max \left(\frac{d_i}{2}, \frac{d_j}{2} \right)^2 + \left(\frac{d_i + d_j}{2} \right)^2} \tag{3.47}$$

where $\left| \mathrm{r}_{ij} \right|$ is the center to center distance between two SPH particles and d_i and d_j are their respective diameters.

To obtain the penetration and penetration rate for two SPH particles in contact by taking into account the curvature of the surface [38] proposes a way to find the average normal vector for the two surfaces in contact. If θ is the angle formed with the normal vectors of particle i and j then the average normal vector for the two particles in contact is given by,

$$
\begin{aligned}
&|\theta| = \angle\left(-\mathrm{n}_i, \mathrm{n}_j\right) \\
&\text{(i)}\ \ |\theta| < \theta_c \quad \text{if Max}\left(\mathrm{r}_{ij}\cdot\mathrm{n}_i, -\mathrm{r}_{ij}\cdot\mathrm{n}_j, \frac{\mathrm{n}_i-\mathrm{n}_j}{\left|\mathrm{n}_i-\mathrm{n}_j\right|}\right) \\
&\qquad\qquad \text{then}\ \ \mathrm{n}_{\mathrm{av}} = \left(\mathrm{n}_i, -\mathrm{n}_j, \frac{\mathrm{n}_i-\mathrm{n}_j}{\left|\mathrm{n}_i-\mathrm{n}_j\right|}\right) \\
&\text{(ii)}\ \ |\theta| \geq \theta_c \quad \mathrm{n}_{\mathrm{av}} = \left(\frac{\mathrm{n}_i-\mathrm{n}_j}{\left|\mathrm{n}_i-\mathrm{n}_j\right|}\right) \\
&\qquad\qquad \text{then}\ \ \mathrm{n}_{\mathrm{av}} = \left(\mathrm{n}_i, -\mathrm{n}_j, \frac{\mathrm{n}_i-\mathrm{n}_j}{\left|\mathrm{n}_i-\mathrm{n}_j\right|}\right) \\
&\theta_c \approx 70^o
\end{aligned}
\tag{3.48}
$$

where θ_c is the critical angle. The penetration and penetration rate for contact between particles is given by

$$
\begin{aligned}
p_{n_{av}} &= \left(R_i + R_j - \left|\mathrm{r}_{ij}\cdot\mathrm{n}_{\mathrm{av}}\right|\right) \\
\dot{p}_{n_{av}} &= \left(\mathrm{u}_i - \mathrm{u}_j\right)\cdot\mathrm{n}_{\mathrm{av}}
\end{aligned}
\tag{3.49}
$$

The force of contact is then obtained by,

$$
\mathrm{F}_i^{con} = \sum_{j\in M_i}\left(\lambda_1\dot{p}_{n_{av}} + \lambda_2 p_{n_{av}}\right)\mathrm{n}_i W_{ij} A_i V_j \tag{3.50}
$$

3.4 Validation

The above SPH contact model is used to simulate impact of two identical disks each of radius 50 mm and the number of SPH particle in each disk is 91. The material is lead whose properties are given in

Table 3-1. The Mie-Gruneisen equation of state is used. The disks move with an equal but opposite initial velocity of 10 m/s.

First the contact detection algorithm is tested to see if the boundary particles can be single out from the inner particles. **Figure 3-2** shows that the boundary particles have a much larger color gradient, $\nabla\tilde{\psi}$ than the particles inside.

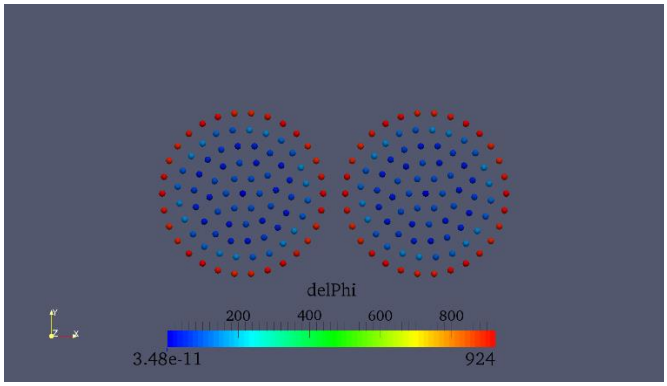

Figure 3-2 The boundary particles indicated by color gradient, $\nabla\tilde{\psi}$

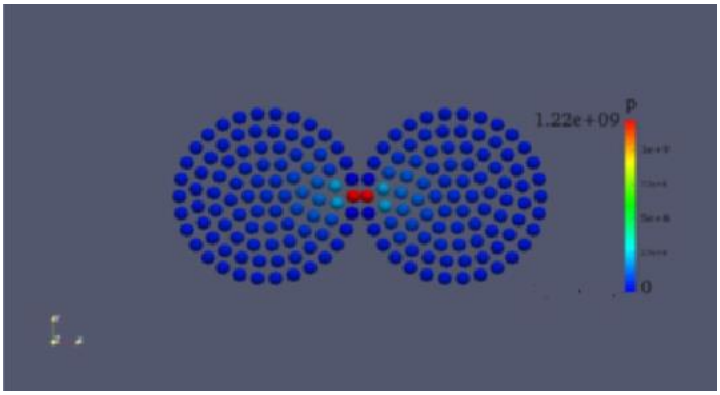

Figure 3-3 Pressure distribution of two colliding disks

Figure 3-4 shows the time history of the total contact force on the particles. The current result is compared with the Hertz solution for collision of two disks. The total force in Hertz model is a function of deformation given by,

$$P_{contact} = K\delta^{n_1} \tag{3.51}$$

$$K = \frac{1}{1.36^{n}} E^{*} L^{n_2} \tag{3.52}$$

where

$$\frac{1}{E^*} = \frac{1-\left(\sigma_1^p\right)^2}{E_1} + \frac{1-\left(\sigma_2^p\right)^2}{E_2}$$

where δ is the deformation. Applying Newton's 2nd law and the contact force relation, the maximum deformation and maximum force due to impact can be calculated as:

$$\begin{aligned} \delta_{\max} &= \left(\frac{n_1+1}{2} \frac{m_{eff}}{K} u_0^{\,2} \right)^{\frac{1}{n_1+1}} \\ F_{\max} &= K \left(\frac{n_1+1}{2} \frac{m_{eff}}{K} u_0^{\,2} \right)^{\frac{n_1}{n_1+1}} \end{aligned} \tag{3.53}$$

where

$$m_{eff} = \frac{m_i m_j}{m_i + m_j}$$

The time for collision between two disks or cylinder with unit length is given as:

$$t_{\max} = \frac{2\delta_{\max}}{u_0} \int_0^1 \frac{d\left(\delta / \delta_{\max}\right)}{\sqrt{1-\left(\delta / \delta_{\max}\right)^{(1+n_1)}}} \tag{3.54}$$

Using n_1 = 10/9 and n_2 = 8/9 an excellent match with the data is obtained (**Figure 3-4** (a)).

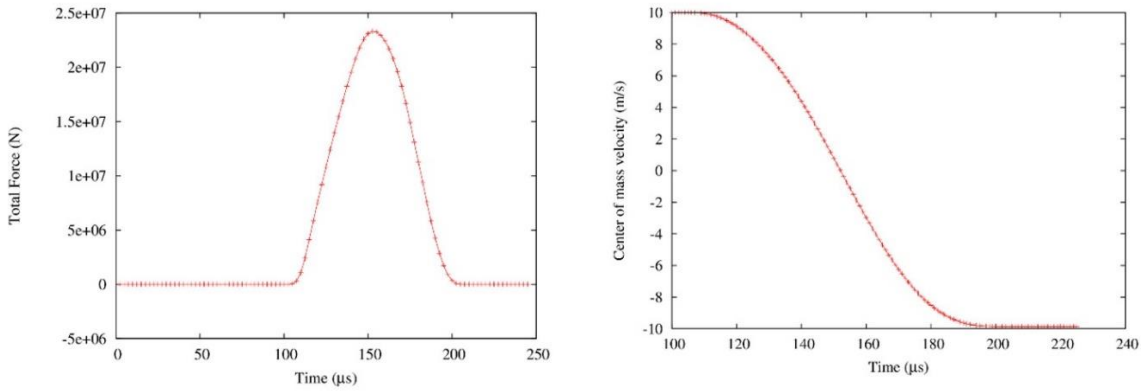

(a) (b)

Figure 3-4 Total contact force-time histories of the impacting disks

Figure 3-4 (b) shows the average velocity-time history of the two colliding disks. It can be seen that the final rebound velocity is equal to the initial velocity of impact. Therefore the kinetic energy is conserved before and after the collision.

3.5 Physical Model

At the beginning of simulation 2,400 mono-sized disks are placed within the two-dimensional square box. The box size, disk size and their material properties are given in **Table 3-2** and

Table 3-1. The disks are placed such that there is no initial contact with the wall of the container or among the disks. The initial packing fraction for the system is 0.8. Gravity is neglected in this study. Two sides of the container are kept stationary while the two other sides are displaced with a linear velocity. The left and bottom walls move backward and forward with an amplitude of 20 mm in each cycle (see **Figure 3-5**). The time period for the cycle is 2.5 millisecond. However, each cycle consists of several steps where the walls are kept stationary to relax the system. The time step used for the simulation is 0.1 microsecond. The moving walls perform several compression cycles where the system is quasi-statically compressed or expanded.

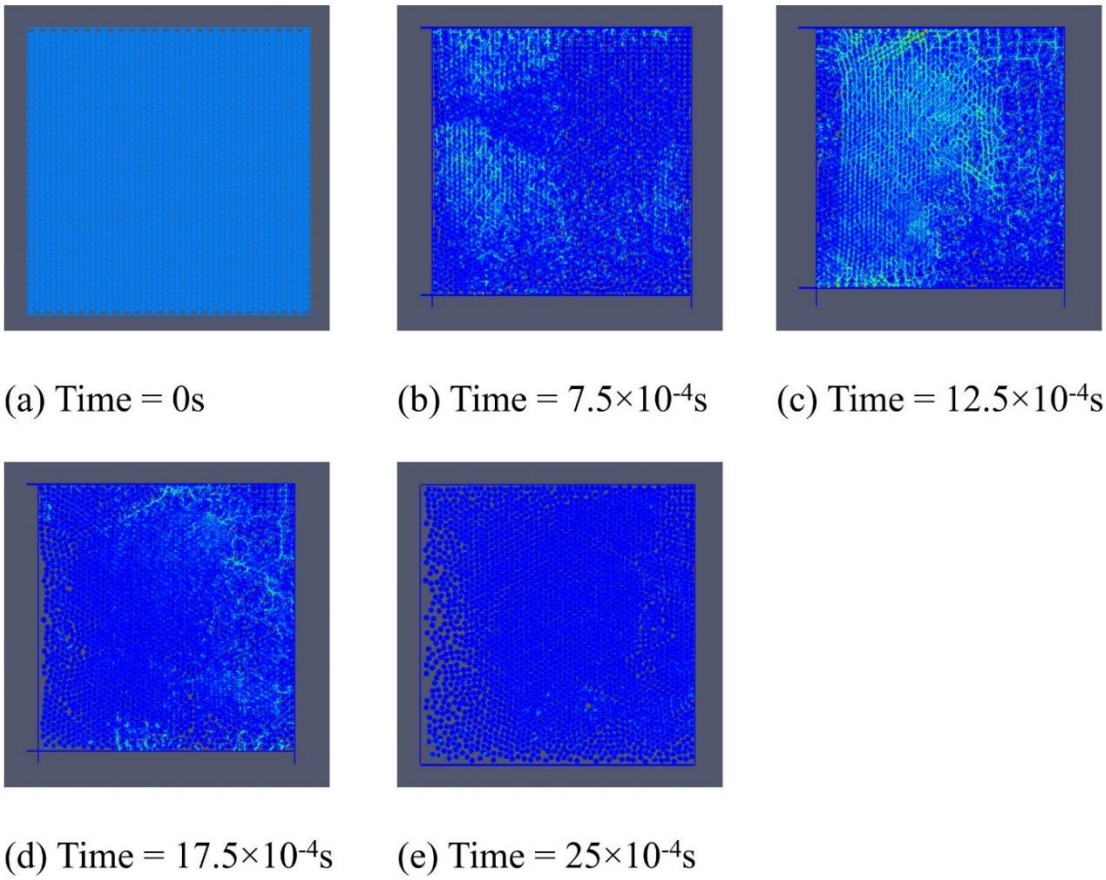

Figure 3-5 One full cycle of compression and expansion showing also the force chain networks.

Figure 3-6 gives a closer view of the disks and the force chains. Each disk consists of 61 SPH particles arranged in an optimum packing configuration [45]. The radius of each SPH particle is about 0.35 mm.

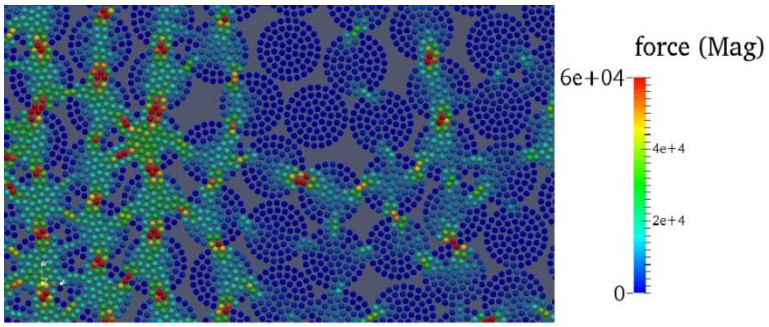

Figure 3-6 A closer look of the disks and force chains.

The walls are also made of SPH particles. For the case of walls square lattice configuration is used and the lattice spacing is twice that of the SPH particle radius. Each wall has two layers of SPH particles.

Table 3-2 Simulation Parameters

Parameters	Values
Box size, m×m	0.2942×0.2942
Time step	1×10^{-7} s
Granular particle numbers	2400
Granular Particle radius	3.026×10^{-3} m
Number of SPH particles per disk	61
SPH Particle radius	3.4868×10^{-4} m

3.6 Results and discussion

3.6.1 Coordination number, Packing fraction and Distribution of contact forces

For a granular system to reach mechanical equilibrium or "jammed," the system needs to satisfy a minimum number of contacts that is theoretically related to the degrees of freedom of the system. The isostatic conjecture [46-52] for frictionless system of N particles in dimension Dim states that for mechanical equilibrium there must be at least Z = 2Dim contacts on average per particle (since there are NZ/2 independent forces and Dim×N force balance constraints). However, the average coordination number from simulation or experiment is usually lower than 2Dim due to the presence of rattlers,

which are particles that do not contribute to the force chain. They may have zero or some contacts, but those contacts do not add to the mechanical stability of the packing. One way to identify rattlers is to count their contacts. For this frictionless simulation case, particles with less than four contacts are defined as rattlers [53-58]. The corrected coordination number, Cc, which is the ratio of the total number of contacts of particles with at least 4 contacts and the number of those particles, shown in **Figure 3-7** (a), follows perfectly the isostatic conjecture. The only zero value of Cc is recorded at the beginning when there is no contact. On the other hand, **Figure 3-7** (b) shows the nice and regular oscillations of the average packing fraction as the system is compressed to a maximum value and expanded. Here the system is compressed to a maximum value of 0.91.

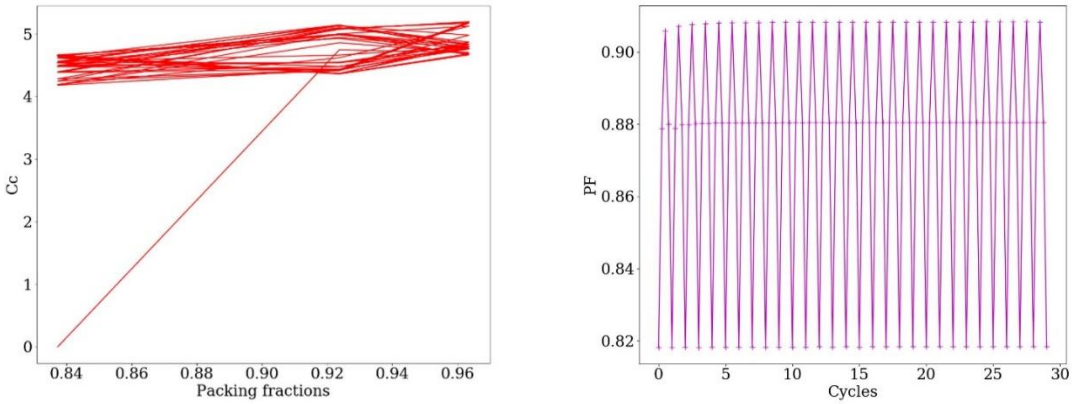

Figure 3-7 (a) Corrected coordination number vs packing fraction for all cycles. (b) Packing fractions change with loading cycles.

The distribution of contact forces for different compression cycles is shown in **Figure 3-8**. Unlike DEM where the force acts at a single point, in SPH the contact force for a single granular particle is found by integrating forces on the individual SPH particles

over the area of contact. Previous studies [59] of granular materials have pointed out that the probability distribution of contact forces decreases exponentially with increase of contact forces, Fn, above the average value, <Fn>. The data shown in **Figure 3-8** for a packing fraction of 0.91, show, this, indeed is the case for present simulation. A black dashed line is added in **Figure 3-8** (b) to aid in visualization The force distributions for all cycles fall on a nearly straight line in the semi-logarithmic plot for probability distribution indicating that the probability distributions of the normalized contact forces follow nearly an exponential decay, which is consistent with previous studies [59]. **Figure 3-8** (a) and (b) also show that the force distributions are nearly constant for loading cycles.

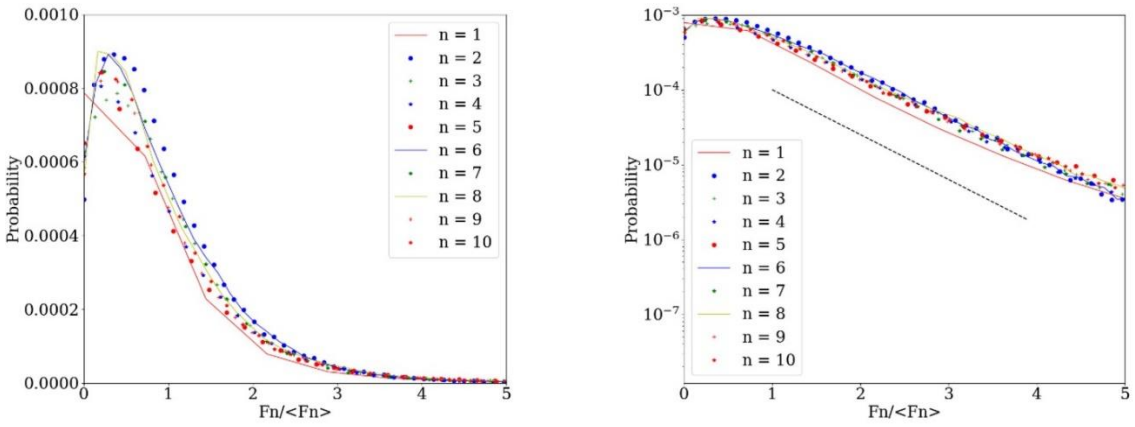

Figure 3-8 Probability distribution of contact forces. The dashed black line in (b) is added as a visual guide only.

3.6.2 Global pressure response

The global pressure on the granular system is computed by first computing the Cauchy stress tensor for the granular system. The Cauchy stress is given by [60]:

$$\sigma_{ij} = \frac{1}{2Area}\sum\left(F_i x_j + F_j x_i\right) \tag{3.55}$$

where *Area* is the area of the confining container; F_i, F_j are the components of the concentrated force *F* on the boundary that is applied on the disks at points $\left(x_i, x_j\right)$. The summation is taken over all such forces. Pressure, p, is then the trace of the stress tensor.

Global pressure response of the system shown in **Figure 3-9** where the total normalized pressure for a packing fraction of 0.85 is shown in **Figure 3-9** (a). **Figure 3-9** (b) indicates pressure, normalized by maximum, for the most compressed states only for different packing fractions. As can be seen, the global pressure decreases with compression step. **Figure 3-9** (b) shows that the global pressure evolves differently for different packing fractions. For packing fraction of 0.9 the global pressure shows very little change with change compression steps whereas lower packing fractions show remarkable change in the global pressure. It can be noted that for all packing fractions in this study, the system is jammed during part of each cycle, however, the stress relaxes to a somewhat lower value. This may be because the cyclic compression of the disks allows the entire structure to slowly rearrange themselves and attain a state of less global pressure for same packing fraction.

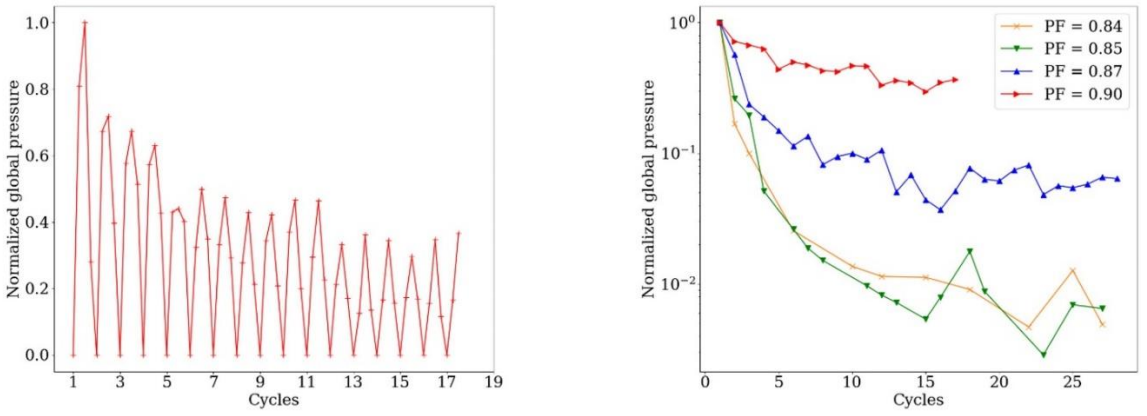

(a) (b)

Figure 3-9 Pressure evolution over the compression cycles

The next and subsequent part of this study focused on finding the origin of this evolution of the global pressure.

3.6.3 Bulk structural change and dynamic heterogeneity

The global stress evolution in the granular system can be associated with bulk structural change within the assembly. If such a bulk rearrangement exists, then it is expected to show up in the motion of the particles tracked over time or cycles. To probe the effect of particle motion, the mobility of particles is considered; it is defined as the displacement of the particle for a given time delay τ (here, time represents the number of compression cycles), relative to the mean displacement of all particles. **Figure 3-10** shows mobilities for three different time delays, τ = 1, τ = 7 and τ = 17, in compression simulation on disks. Particles with similar mobility are represented by similar colors in **Figure 3-10**. Specifically, the colors correspond to the following fractional changes relative to all the particles: red, 0.90 ± 0.1; yellow, 0.70 ± 0.10; green, 0.50 ± 0.10; cyan, 0.30 ± 0.10; and blue, 0.10 ± 0.10.

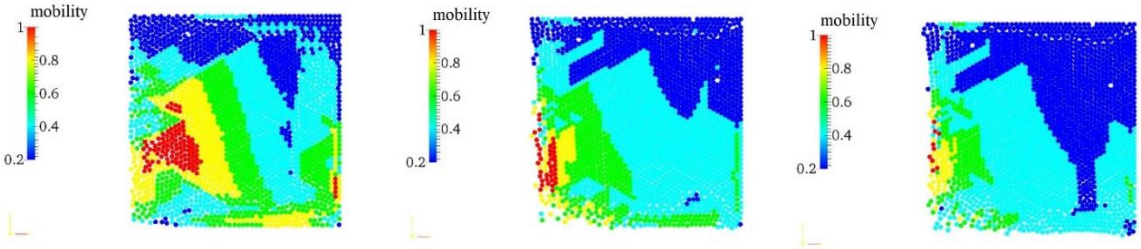

(a) Cycle 1 (b) Cycle 7 (c) Cycle 17

Figure 3-10 Mobility of the particles (disks) for different cycles. The initial packing fraction of the system is ϕ = 0.8. The time delay τ equals (a) 1 cycles (b) 7 cycles and (c) 17 cycles.

The particle mobility, shown in **Figure 3-10**, reveals that particles with similar mobility form large clusters and these clusters or regions grow with time. This indicates heterogeneous structural change both in time and space. The dense structure of these clusters suggests small local rearrangements of the particles. The number of particles with least mobility increases with time whereas particles with highest mobility decrease; however, this change occurs in a collective form which further suggests local rearrangement of particles. **Figure 3-11** shows the histogram of the particles based on their mobility for the given cycles, which also confirms the above observations.

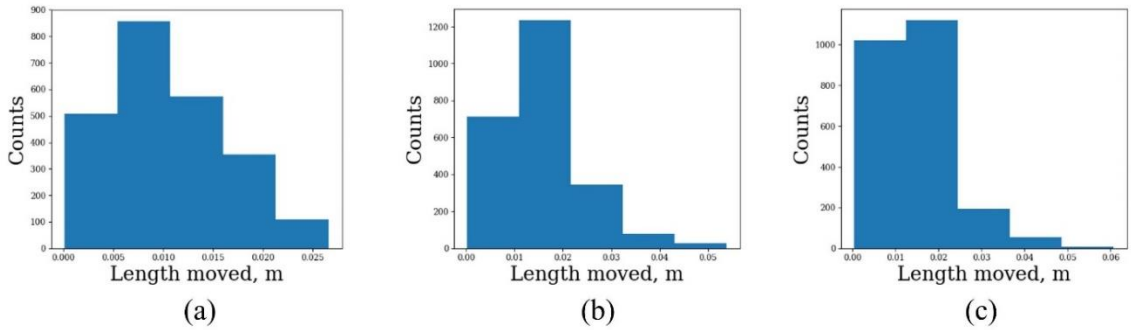

Figure 3-11 Histogram of the mobility of the particles (disks) for different cycles. The initial packing fraction of the system is PF = 0.8. The time delay τ equals (a) 1 cycle (b) 7 cycles and (c) 17 cycles.

As an alternative approach to quantifying these heterogeneous dynamics, the four-point susceptibility $\chi_4(\tau)$, which indicates the extent of temporal correlation of dynamics at any pair of spatial points is studied [1]:

$$\chi_4(\tau) = N\left[\left\langle Q_s(\tau)^2\right\rangle - \left\langle Q_s(\tau)\right\rangle^2\right] \tag{3.56}$$

where $Q_s(\tau)$ is defined as

$$Q_s(\tau) = (1/N)\sum_{i=1}^{N} w\left(\left|r_i(t) - r_i(0)\right|\right), \textit{ with}$$
$$w = \begin{cases} 1 & \textit{if } \left|r_i(t) - r_i(0)\right| < l, \\ 0 & \textit{otherwise.} \end{cases} \tag{3.57}$$

where N is the number of particles, and $r_i(t)$ indicates the particle positions at time t, for a length scale l (the unit of length scale, l, is the radius of the disks). The averages are taken over all the particles and over all starting times. $Q_s(\tau)$, which is referred to as the self-overlap order parameter, is a measure of particle mobility and is quantified by a length scale l. $Q_s(\tau)$ and $\chi_4(\tau)$ vs cycles are plotted in **Figure 3-12** (a) and (b), respectively. As can be seen, $Q_s(\tau)$ varies from 1 to 0 as the time delay τ increases. On the other hand, $\chi_4(\tau)$ has a maximal point for each length scale, which basically characterizes a time delay τ^*, by which the particles, on average, move more than the length scale l.

As seen in **Figure 3-12** (b), $\chi_4(\tau)$ is maximum for the characteristic length scale $l^\dagger \simeq l/20$ for a packing fraction of 0.93. The characteristic $l^\dagger$ for each $\chi_4(\tau)$ plot of different packing fractions can be examined and the corresponding maximal $\tau^\dagger$ can be found. **Figure 3-12** (c) shows the maximum $\chi_4(\tau)$ curve for different packing fractions. The plot suggests that the typical length scales for l are just fraction of a particle diameter. Also, the plot provides a characteristic time scale $\tau^\dagger$ by which the particles, on average, move more than the length scale l. The characteristic time scale, $\tau^\dagger$, is typically 25 cycles for any packing fractions. Hence the particles can be considered largely confined. However, their small movement is enough to modify the force network and relax the system stress.

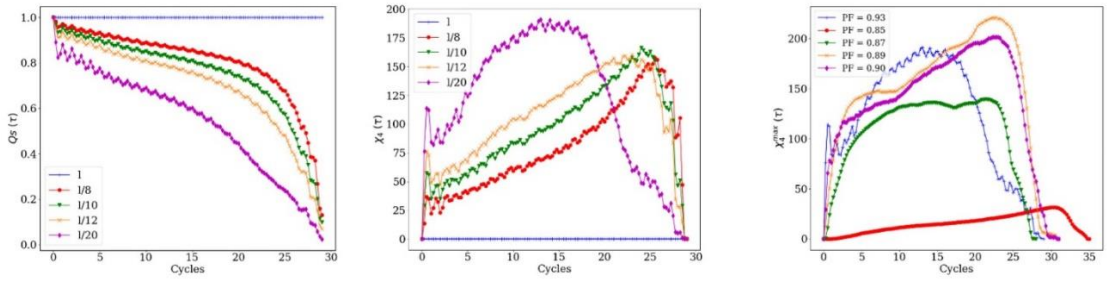

(a) (b) (c)

Figure 3-12 (a) $Q_s(\tau)$ vs cycles for packing fraction 0.93. (b) $\chi_4(\tau)$ vs cycles for packing fraction 0.93. (c) Maximum $\chi_4(\tau)$ curve for different packing fractions (PF).

3.6.4 Structural deformations in compressed states

The heterogeneous dynamics study in the previous section inspires a deeper look at the meso-scale structural change that can give rise to change in global stress. On such an endeavor, the granular system is probed using Falk-Langer [61] measures of affine and non-affine deformations. A cutoff radius of 2.5d is used for the FL analysis. This typically includes 10-15 neighboring particles, including the particle of interest. The deformation of these particles is followed for a time equal to $\tau^{\dagger}$ obtained from the previous study.

Unlike FL analysis, the particles displacements are measured with respect to the center of mass of the assembly within the cutoff radius. If r_i and r_i' are the locations of all the particle *i* with respect to the center of mass of the assembly for the initial and final steps then a 2x2 matrix, E' can be obtained from the least-square fit of the equation:

$$r_i' = E' \bullet r_i \tag{3.58}$$

The matrix E is the best-fit linear map that affinely transforms the particles from the first position to the next one. The matrix E' can be written in terms of a symmetric matrix, F, and a rotational matrix, R_θ, as,

$$E' = F'R_\theta \tag{3.59}$$

From the symmetric matrix, F', the strain matrix can be obtained as,

$$\varepsilon = F' - I \tag{3.60}$$

The affine shear strain and affine deformation can then be obtained from the eigenvalues (ε_1 and ε_2 where $\varepsilon_2 \geq \varepsilon_1$) of the local strain matrix, ε:

Affine shear strain: $$\delta\varepsilon = \varepsilon_2 - \varepsilon_1 \tag{3.61}$$

Affine dilation: $$2\bar{\varepsilon} = \varepsilon_1 + \varepsilon_2 \tag{3.62}$$

Non-affine deformation can be obtained as: $D_{\min} = \left(\sum \left(r_i' - E \bullet r_i\right)^2\right)^{\frac{1}{2}}$ (3.63)

Figure 3-13 represents data for affine and non-affine deformations for different packing fractions over several compression cycles in the granular system. The deformation data presented are summed over all particles and normalized by their initial mean value. Both affine and non-affine deformations fall quickly to a fixed value and fluctuates around it. The rate of decrease of normalized average affine shear strain is much higher for lower packing fractions than that for higher packing fractions. This possibly suggests a much longer relaxation time scale for systems with higher packing fractions. Similar trend is observed for normalized average affine dilation. The higher packing fraction of the system allows the particles to dilate and maintain their deformation. As for the normalized non-affine squared displacement the trend is not so clear. For packing fraction below 0.89 the graph approaches zero quite rapidly. However, for higher packing fractions the graph fluctuates around a mean value suggesting that the non-affine deformation persists throughout the entire loading cycles.

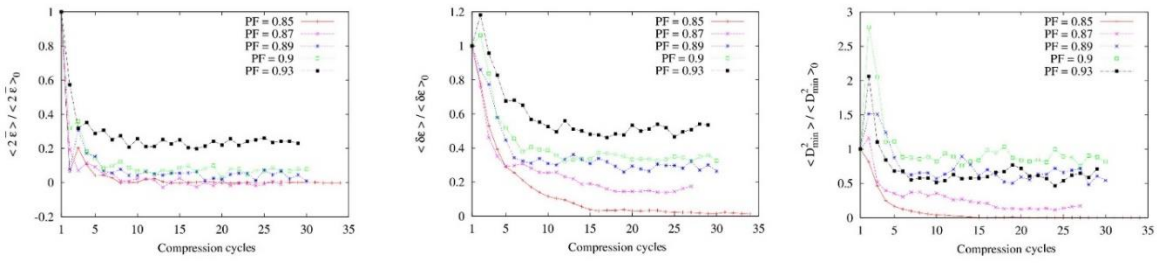

Figure 3-13 Deformation of the particles for different cycles (a) normalized average affine dilation (b) normalized average affine shear strain (c) normalized non-affine mean squared displacement

The affine and non-affine deformations are also correlated, which is demonstrated in **Figure 3-14**. The graph suggests that there is a monotonic increase in non-affine displacement with affine shear strain. However different packing fraction occupy different areas of the graph with some overlap. This suggests a relation between systems of different packing fractions.

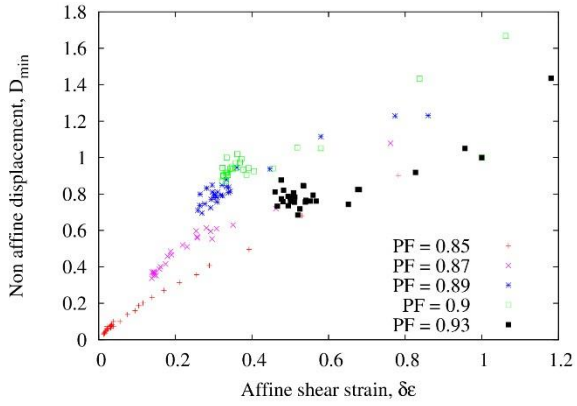

Figure 3-14 Correlation of affine and non-affine deformations for various packing fractions.

The intensity plot of the non-affine mean squared displacement is shown in **Figure 3-15** for three different cycles revealing regions with higher non-affine deformations

compared with the rest of the system. At the beginning of loading cycle, most non-affine deformations occur away from the moving walls. As the number of compression cycles increases the non-affine deformations occur more near the wall as indicated by the dark (blue) region in the intensity plot for higher cycle. **Figure 3-15** can be compared with **Figure 3-10** where the particles are categorized by their mobility.

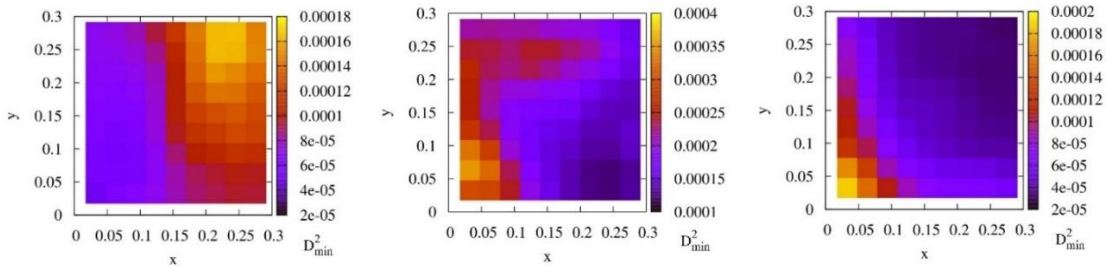

(a) Cycle 1 (b) Cycle 7 (c) Cycle 17

Figure 3-15 Intensity plots of $D^2_{\min}$ for various cycles during simulation. The data shown are for packing fraction, ϕ = 0.87. Darker (blue) regions indicate low $D^2_{\min}$ and brighter (red) regions indicate high $D^2_{\min}$.

At the beginning of loading cycle particles near the wall move with the wall and affine deformation presides over non-affine deformation. The particles at the top right corner are forced to rearrange themselves in a more compact structure, thus more non-affine deformations occur at that region. For higher cycles, the particles at the top right can do little in terms of structural rearrangement so the non-affine deformation zone moves down near the walls where particles with higher mobility still have some room to rearrange themselves into more compact structures.

3.6.5 Linking initial micro-structure to plastic rearrangement

The non-affine deformations as discussed in previous section give rise to plastic rearrangement of the particles in the structure. This plastic rearrangement causes a

change in the global stress response of the system. In this section the non-affine deformations of the particles are studied by relating it to the initial micro-structure. More specifically, the question addressed in this section is whether one can predict the global response of the system having prior information about the initial micro-structure (local packing fraction).

First, to get the local packing fraction, the entire system is decomposed into Voronoi cells with radical Voronoi tessellation method. For this purpose, the efficient "pyvoro" software is used developed by Joe Jordan which is a python extension of "voro++" code developed by Chris Rycroft [62]. A sample of the Voronoi tessellation is shown in **Figure 3-16** (a). The local packing fraction at each loading cycle is then calculated by the formula,

$$\phi_i = \frac{V_i}{V_c} \tag{3.64}$$

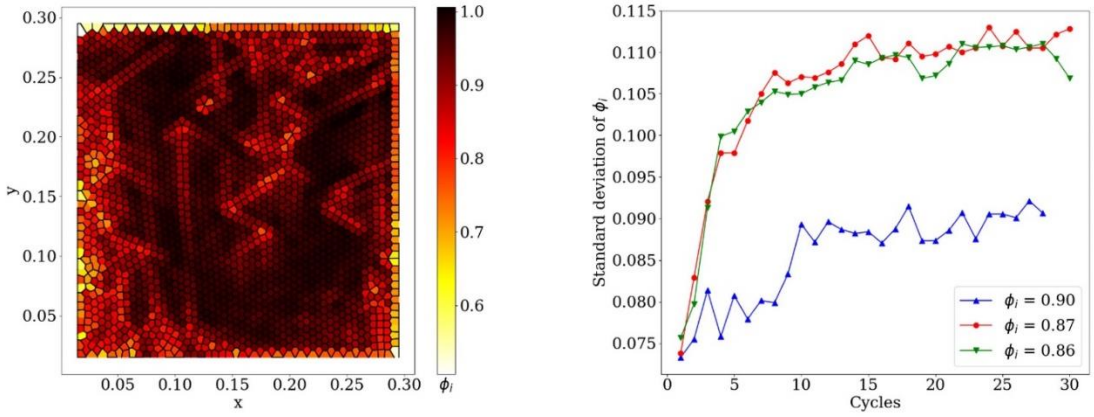

(a) (b)

Figure 3-16 (a) Voronoi tessellation and local packing fraction shown colored by magnitude (b) standard deviation of local packing fraction for different load cycles.

where ϕ_i is the packing fraction around each particle *i*, V_i is the area of particle *i* and V_c is the area of the Voronoi cell around particle *i*. The local packing fraction field is shown

in **Figure 3-16** (a) where the intensity of the color in each cell varies according to the relative packing density. One can immediately recognize from the figure that not all areas have the same packing density. There are regions of high and low local packing fraction. The standard deviation of local packing fraction for different global packing fraction is also shown in **Figure 3-16** (b). The standard deviation for different cycles is very similar for global packing fraction 0.86 and 0.87 but very different from 0.90. The standard deviation for all three rises with loading cycles and approaches a maximum value. As the walls press down on the particles during loading cycle the average packing fraction of the granular system increases and reaches a maximum value. However due to particle rearrangement in subsequent loading cycles the local packing fractions become more diverse as indicates by the increase in standard deviation of the local packing fraction. However, the increase in diversity is not much for PF = 0.90 as for PF = 0.86 and 0.87. It can be recalled from **Figure 3-9** (b) that the global pressure shows negligible relaxation for packing fractions above 0.9. It is worth studying if there is a correlation between the initial micro-structure or local packing fraction distribution and the non-affine plastic deformation of the particles.

Figure 3-17 shows three two-dimensional histogram plots of $D^2_{\min}$ and ϕ_i for PF = 0.87 at 3, 7 and 11 load cycles. A white dashed line is drawn in the plot to help visualize the correlation between the two variables but is not a best fit of the data. A least-square mean fit is found to be very sensitive to the higher and lower end values. The plots reveal that the two quantities, $D^2_{\min}$ and ϕ_i, are indeed related. Despite having a significant dispersity in data, a lower value of ϕ_i usually means a higher value of $D^2_{\min}$ and vice versa.

To further verify the correlation between $D^2_{\min}$ and ϕ_i, the Pearson correlation coefficient, the standard correlation coefficient for two variables, is calculated for all N = 2400 particles.

$$\mathrm{Corr}\left(D^2_{\min}, \phi_i\right) = \frac{\sum_{i=1}^{N}\left(\left(D^2_{\min}\right)_i - \left\langle D^2_{\min}\right\rangle\right)\left(\phi_i - \langle\phi_i\rangle\right)}{\sqrt{\sum_{i=1}^{N}\left(\left(D^2_{\min}\right)_i - \left\langle D^2_{\min}\right\rangle\right)^2}\sqrt{\sum_{i=1}^{N}\left(\phi_i - \langle\phi_i\rangle\right)^2}} \tag{3.65}$$

where $\left(D^2_{\min}\right)_i$ means the non-affine squared deformation for particle *i*, and $\langle\ \rangle$ means average value. No correlation is indicated if the correlation coefficient is 0 and -1 means perfect negative correlation. The correlation coefficient for all load cycles and for three different packing fractions is shown in **Figure 3-18**. The correlation coefficient increases somewhat monotonically in negative value after the first load cycle and reaches a maximum of about -0.55. The plot confirms the negative correlation between $D^2_{\min}$ and ϕ_i suggested by **Figure 3-18**. The negative correlation suggests that particles with low local porosity undergo more non-affine plastic deformation than others. Interestingly, the correlation coefficients are very similar for different packing fractions. However, from **Figure 3-16** (b) it is seen that the standard deviation for packing fraction 0.90 is much lower than that for other packing. At high global packing fraction the local packing density field is more uniform than for low global fraction. This allows one to make connection between global packing fraction and stress relaxation in terms of the non-affine plastic deformation. For higher packing fractions there are not enough particles with low local packing density to undergo plastic deformation and allow the system to relax.

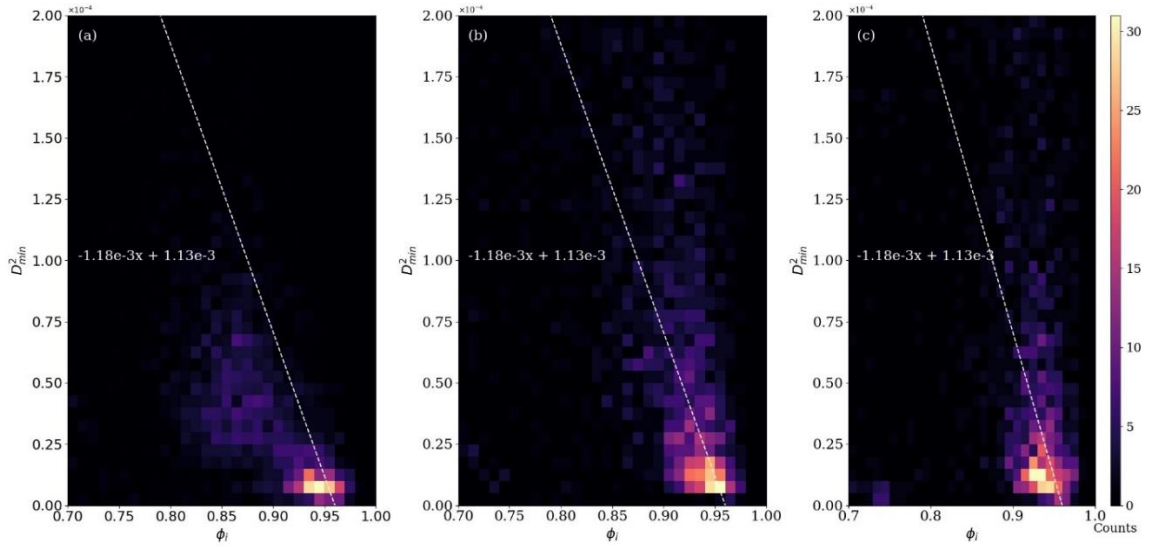

Figure 3-17 Density plot of $D^2_{\min}$ and ϕ_i for different cycles (a) 3 cycles (b) 7 cycles (c) 11 cycles. The dashed white lines are given as a visual guide but are not best fit of the data.

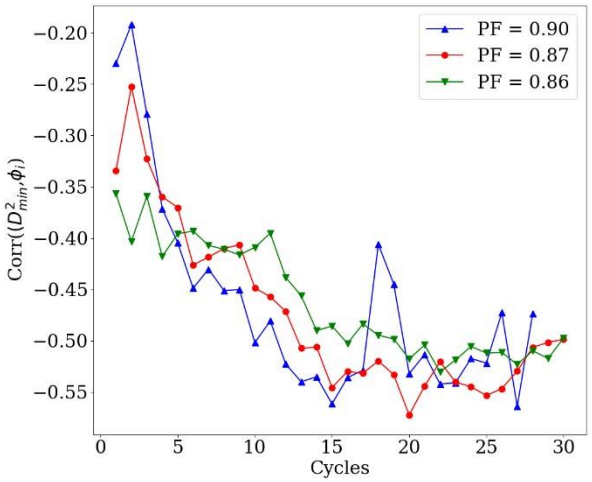

Figure 3-18 Correlation coefficient for $D^2_{\min}$ and ϕ_i at each load cycle for various packing fractions.

3.6.6 Contact Network analysis

Finally, a contact network analysis is carried out to have a deeper look on the structural rearrangement of the particles based on their connectivity. In contact network

analysis each node of the contact network represents an individual particle and a contact between two particles is represented by an edge. The contact network so formed is undirected and unweighted. The contact networks at the beginning of the compression cycles show fewer connections and subnetworks and fewer closed paths compared to the contact network when the system is strongly jammed. The strongly jammed configuration exhibits many closed path triangles or cycles. In order to quantify the network some complex network parameters are defined below.

In an unweighted complex network the degree of a node is the number of edges adjacent to it, or the number of particles it is in contact with. It can be calculated from the adjacency matrix:

$$k_i = \sum_j a_{ij} \tag{3.66}$$

where a_{ij} are elements of the adjacency matrix. An adjacency matrix $\tilde{A}$ is a matrix whose non-zero elements a_{ij} are such that a_{ij} = 1 if nodes or particles i and j are in contact and zero otherwise. The node degree can be averaged over all nodes or particles to give a measure of the average number of contacts per particle. The clustering coefficient gives a measure of the local connectivity of a node by enumerating the number of 3-cycle closed paths or triangles associated with it and its contacting neighbors. It can be calculated from the adjacency matrix as,

$$c(i) = \frac{1}{k_i(k_i - 1)} \sum_{j,h \in V(i)} a_{ij} a_{jh} a_{hi} \tag{3.67}$$

where k_i is the vertex degree defined above and $V(i)$ is the set of neighboring vertices of i. The clustering coefficient ranges from 0 (no contacting neighbors) to 1 (all particles and their contacting neighbors are fully connected with each other). Each $c(i)$ is averaged

over all particles to obtain the average clustering coefficient which gives an insight about the number of 3-cycles in the network.

The average degree and average clustering coefficient of the contact networks as shown in **Figure 3-19** (a) and (b). Both plots are created by averaging over all particles in a given load step. The average quantities in both figures show peaks at maximum compression and troughs when fully unloaded. The average degree gradually increases for all global packing fractions with the increase in load cycles showing that the particles are getting more closely packed. For PF = 0.90 the average degree peaks to about 3.5 which is close to the isostatic limit. For other packing fractions the peak values are lower. Similar behavior is observed for average clustering coefficient. Increase in average clustering coefficient means that there are more 3-cycles in the network, which, as found by other researchers, increase the number of force chains in the system [63]. It is also found that the global pressure usually depends on the maximum normal contact force higher than the average force [63]. Hence increase in force chains or force bearing particles means the global pressure can relax for the system.

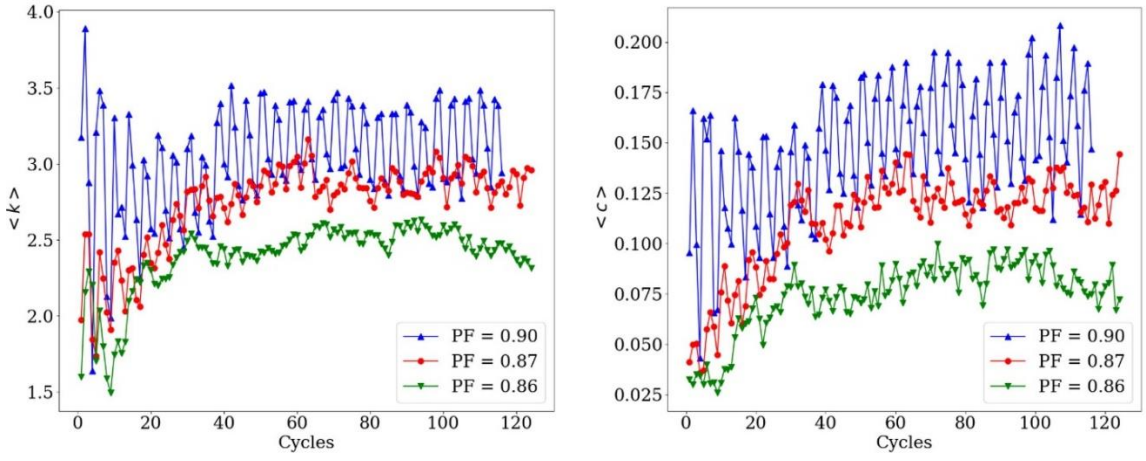

(a) (b)

Figure 3-19 (a) Average degree vs cycles. (b) Average clustering coefficient vs cycles.

It would be interesting to investigate if there is a correlation between the local packing fraction defined in the previous section and the degree of particles. One can assume that, since higher the connectivity of the particle higher is its degree, that particles with high degree are situated in a region with high packing fraction. The density plots of **Figure 3-20** show, this, indeed is the case. Again, the white dashed line is not a best fit of the data but added as a visual guide for the plot. The plots show the relation between the particle degree and local packing fraction for three different load steps, 3, 11 and 19 load cycles.

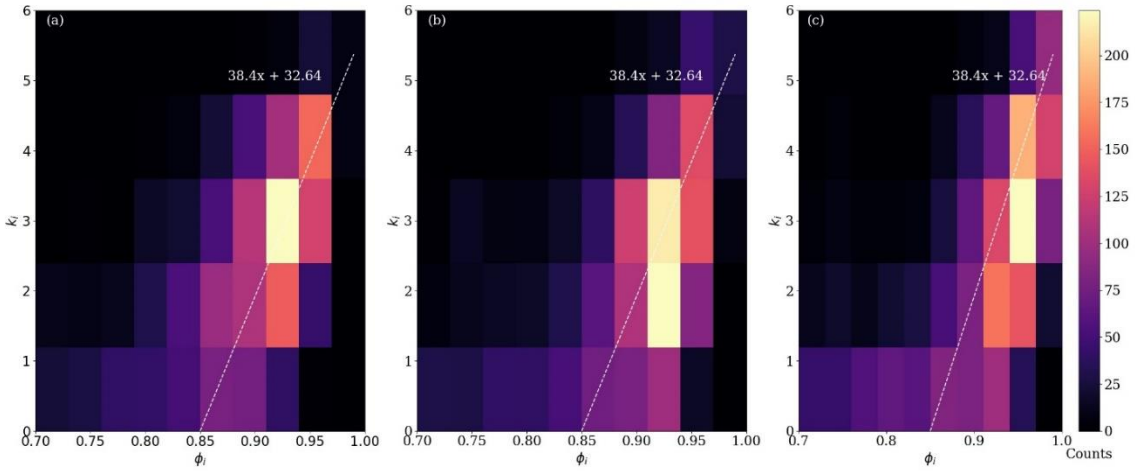

Figure 3-20 Density plot of k_i and ϕ_i for different cycles (a) 3 cycles (b) 11 cycles (c) 19 cycles. The dashed white lines are given as a visual guide but are not best fit of the data.

To further confirm the correlation, the correlation coefficients for k_i and ϕ_i are plotted for each cycle and shown in **Figure 3-21** (a), which shows that there is a high amount of correlation exists between the two for all cycles. In the previous section it was

shown that $D^2_{\min}$ and ϕ_i are negatively correlated and the correlation coefficient increases with cycles. **Figure 3-21** (b) shows the correlation coefficient for $D^2_{\min}$ and k_i for different load cycles. The quantities $D^2_{\min}$ and k_i are negatively correlated as shown in **Figure 3-21** (b) which is not surprising given the fact that k_i and ϕ_i are positively correlated. Thus, a connection can be made between the Falk-Langer deformation analysis of section 3.4 and the complex network analysis of section 3.6 in that higher non-affine deformation or plastic rearrangement is usually related to particles with lower degree of connectivity and local packing fraction.

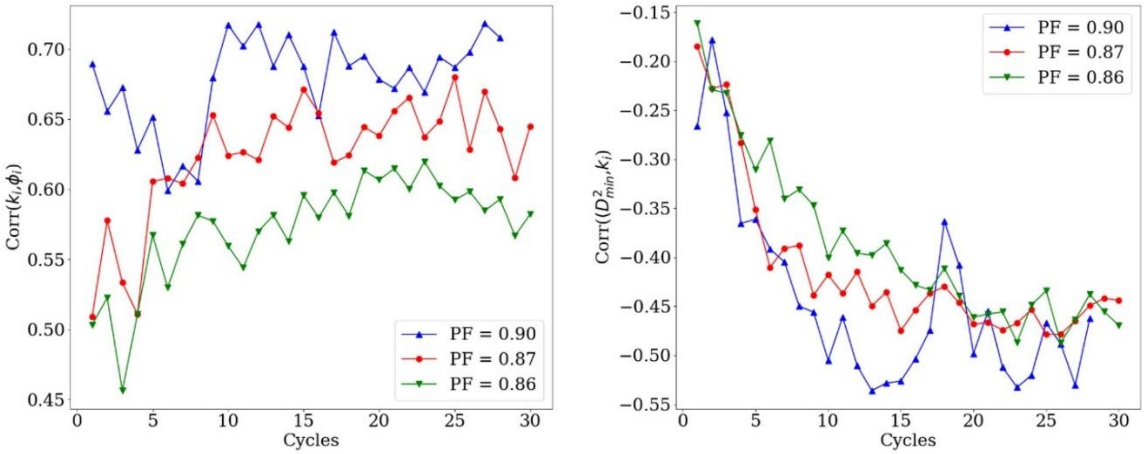

(a) (b)

Figure 3-21 (a) Correlation coefficient for k_i and ϕ_i and (b) correlation coefficient for $D^2_{\min}$ and k_i at each load cycle for various packing fractions.

It is also worth studying the 3-cycle population of the contact network as they are important in stabilizing the contact network. These cycle structures are found by computing the population of the various minimal cycles in the contact network. A minimal cycle basis of a graph is a set containing the shortest cycles based on minimum length or number of edges. There are several algorithms proposed by other researchers to

obtain a minimal cycle basis for a complex network. Here, the fast and improved algorithm based on Mehlhorn and Michail [64] is implemented to find the minimal cycle basis for the contact network. **Figure 3-22** (a) shows the contact network at 26 compression cycles for PF = 0.90 when the system is strongly jammed. The particles are represented as nodes and contacts as edges. **Figure 3-22** (b) shows only the minimal cycles of the same network with the rattlers removed.

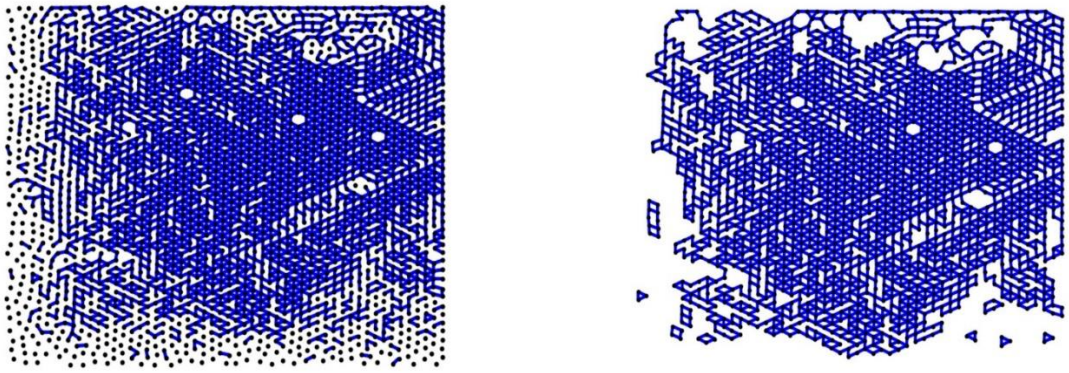

(a) (b)

Figure 3-22 (a) Contact network with nodes as particles and edges as contact at 26 compression cycle. (b) Same network with rattlers removed.

According to the clustering coefficient, population of 3-cycles and other higher order substructures is expected to peak when the system is in strongly jammed configurations. This is indeed the case as shown in **Figure 3-23** (a) where the 3-cycle and 4-cycle structures oscillate throughout the loading cycles. Only low-order cycles, namely, 3, 4 and 5 cycles are shown in **Figure 3-23** (a). Cycles greater than 5 have negligible populations. As shown in **Figure 3-23** (a) the population of 4 cycles shows oscillations but the oscillations are small compared to 3 cycles and the oscillations of 5 cycles are even smaller. There is a gradual rise in the 3 cycles population throughout the

compression cycles at the strongly jammed state indicated by a rise in the peak values of oscillations. This means that the granular systems rearrange themselves in a way which gives rise to more 3-cycles in the network in the jammed state as the number of compression cycle increases.

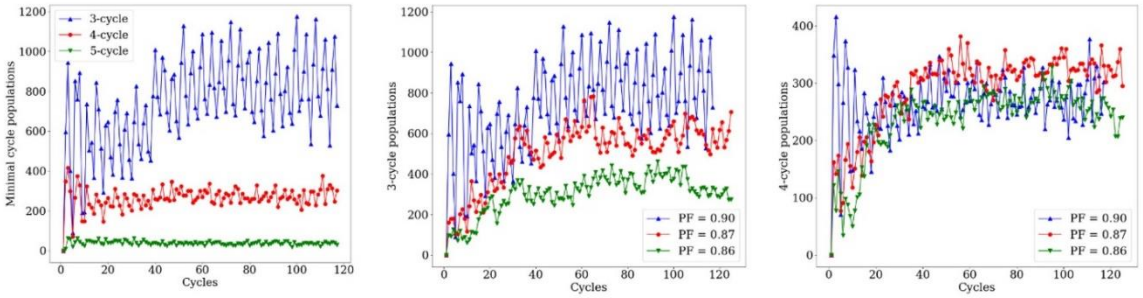

(a) (b) (c)

Figure 3-23 (a) Population of 3-cycles, 4-cycles and 5-cycles for PF = 0.90. (b) 3-cycle populations only and (c) 4-cycle populations only for all loading cycles for various PF.

Figure 3-23 (b) and (c) compare the populations of the 3-cycles and 4-cycles for different global packing fraction. The population of 3-cycles rises for all packing fractions and higher packing fractions have higher number of 3-cycles in the network. On the other hand, the populations of 4-cycles are quite similar for the three packing fractions shown in **Figure 3-23** (c) at higher load cycles. Hence, enrichment of 3-cycle population can be considered as a marker for successive compressive loading of a granular system.

3.7 Conclusion

In this study, Smooth Particle Hydrodynamics (SPH) method is used to simulate the cyclic compression of deformable two-dimensional disks assembly and to study their jamming behavior. The results obtained show that the average coordination number

varies with packing fraction during jamming which conforms to the isostatic conjecture. Force distribution shows familiar exponential behavior as the average force on the system is increased. Stress relaxation is seen to occur after several compression cycles which is marked by a decrease in global pressure. Structural rearrangement, that can give rise to stress relaxation, is revealed by grouping of particles with similar relative mobilities and χ_4 measures which also provide a characteristic time scale $\tau^{\dagger}$ for which the particles on average move more than a characteristic length scale $l^{\dagger}$. The meso-scale structural deformations are studied by Falk-Langer analysis. Active regions of non-affine deformations are found, and locations of these regions change over cycles. The local packing fraction of the granular system is obtained by employing radical Voronoi tessellation method. The standard deviation of the local packing fraction is seen to increase with load cycle but at a different rate for different global packing fraction. This suggests that the local packing fraction becomes more diverse with increasing compression cycle. For high global packing fraction the diversity is less pronounced. The correlation coefficient between non-affine squared deformation and local packing fraction suggests that the two quantities are negatively correlated for both high and low packing. This infers that at high enough global packing fraction there is not much room for the system to relax its stress state. Finally, complex network analysis is performed to study the contact network properties of the system. The average degree and average clustering coefficient obtained from the complex network analysis show peaks at maximum compressions, but the peak values increase with cycles. The degree per particle is found to be positively correlated with local packing fraction and negatively correlated with the non-affine squared deformation. An enrichment of 3-cycle population is

observed for all global packing fraction with increase in compression cycle. Thus, the number of 3-cycle population can be considered as an important parameter to characterize the system behavior in cyclic compression of granular system.

4 NUMERICAL INVESTIGATION OF EVAPORATION INDUCED SELF-ASSEMBLY OF SUB-MICRON PARTICLES SUSPENDED IN WATER

4.1 Introduction

In many applications granular materials are surrounded by fluid and the solid particles and fluid influence each other's behavior. Fluid behavior can be predicted by finite volume Volume of Fluid (VOF) simulation whereas DEM can be used to model particle behavior. For a system with both granular material and fluid a coupling between the two method called VOF-DEM is desirable to simulate the particle-fluid system. VOF-DEM method can further be classified into two categories: resolved VOF-DEM and unresolved VOF-DEM.

In resolved VOF-DEM the particles are larger than the fluid control volume and meshing for VOF is done around the particles. The method provides a better resolution of the fluid field and the force on each particle is calculated individually. This method is only suitable for cases with small number of particle due to computational expense required for large number of particles. In contrast, the unresolved VOF-DEM, which is used in this work, is capable of handling large number of particles. The particles are significantly smaller than the mesh cells and there can be more than one particle in a cell. In this chapter the unresolved VOF-DEM technique is used to study the deposition pattern of suspended particle as the surrounding liquid film evaporates. The particles and fluid exchange momentum and heat with each other during the process.

4.2 Equations of motion

The governing equation for the fluid phases consists of a set of volume averaged mass and momentum balance equations in an Eulerian description. The fluid phases are considered incompressible and in the CFD domain the particle phase is characterized by void fraction field α_f. The liquid and the vapor phases are denoted by α_1 and α_2 respectively.

The mass and momentum equations for the fluid and solid phases are given in the following sections.

4.2.1 Fluid Phase

$$\frac{\partial\left(\rho\alpha_f\right)}{\partial t}+\nabla\cdot\left(\rho\alpha_f\mathbf{U}\right)=0 \tag{4.1}$$

$$\frac{\partial(\alpha_1\alpha_f)}{\partial t}+\nabla\cdot\left(\alpha_1\alpha_f\mathbf{U}\right)+\nabla\cdot\left(\alpha_1\alpha_f\mathbf{U}_r\left(1-\alpha_1\right)\right)=\dot{S}_v \tag{4.2}$$

$$\frac{\partial}{\partial t}\left(\alpha_f\rho\mathbf{U}\right)+\nabla\cdot\left(\alpha_f\rho\mathbf{U}\otimes\mathbf{U}\right)=-\nabla\cdot\left(\alpha_f p_{\rho gh}\right)-\mathbf{g}\cdot\mathbf{r}\nabla\left(\alpha_f\rho\right)+\nabla\cdot\left(\alpha_f\tau\right)+\alpha_f\sigma_K\nabla\alpha_1-\mathbf{F}_d \tag{4.3}$$

where

$$\alpha_1\alpha_f+\alpha_2\alpha_f=\alpha_f \tag{4.4}$$

$$\alpha_1+\alpha_2=1 \tag{4.5}$$

$$\alpha_f p_{\rho gh}=\alpha_f p-\alpha_f\rho\mathbf{g}\cdot\mathbf{r} \tag{4.6}$$

$$\tau=\mu\left(\nabla\mathbf{U}+\left(\nabla\mathbf{U}\right)^T\right)-\frac{2}{3}\left[\mu\left(\nabla\cdot\mathbf{U}\right)I\right] \tag{4.7}$$

where ρ is the average fluid density, $\mathbf{U}$ is the average velocity of fluid, $\dot{S}_v$ represents source terms due to phase change, σ_K is the surface tension effect at the interface, p_{rgh} is

the dynamic pressure, $\mathbf{F}_d$ is the drag force term, μ is the mean viscosity and $\mathbf{g}$ is the acceleration due to the gravity. The third term on the left side of equation (3.2) is the compressibility term added to obtain sharp interfaces [65] and $\mathbf{U}_r$ is the relative velocity between two fluid phases.

4.2.2 Solid Phase

$$m_i \dot{\mathbf{u}}_{ip,} = \mathbf{F}_{ij}^{\ n} + \mathbf{F}_{ij}^{\ t} + \mathbf{F}_{coh} + m_i \mathbf{g} + \mathbf{F}_d + \mathbf{F}_b \tag{4.8}$$

$$I_i \dot{\boldsymbol{\omega}}_i = \mathbf{Trq}_{ij}^{\ r} + \mathbf{Trq}_{ij}^{\ t} \tag{4.9}$$

where m_i is the mass of the ith particle, $\mathbf{u}_{p,i}$ is the velocity of the ith particle, I_i is the moment of inertia of the particle and $\boldsymbol{\omega}_i$ is the angular velocity of the ith particle. $\mathbf{F}_{ij}^{\ n}$ and $\mathbf{F}_{ij}^{\ t}$ are normal and tangential force due to contact, $\mathbf{F}_{coh}$ is the cohesive force between two particles, $m_i\mathbf{g}$ is force of gravity, $\mathbf{F}_d$ is the drag force due to relative fluid motion and $\mathbf{F}_b$ is the buoyant force. $\mathbf{Trq}_{ij}^{\ r}$ is the torque due to rolling friction and $\mathbf{Trq}_{ij}^{\ t}$ is the torque due to tangential force.

4.2.3 Drag Force

The drag force accounts for the force acting on the particle due to relative motion between particle and fluid. The drag model used is suitable for particles in the near sub-micron range [66].

$$\mathbf{F}_d = \frac{18\mu}{d^2 C_c}\left(\mathbf{U} - \mathbf{u}_p\right) \tag{4.10}$$

where

$$C_c = 1 + \frac{2\lambda'}{d}\left(1.257 + 0.4e^{-(1.1d/2\lambda')}\right) \tag{4.11}$$

where λ' is the mean free path of water which is 2.5×10^{-10} m and d is the diameter of the particle.

4.2.4 Buoyant Force

$$\mathbf{F}_b = -\mathbf{g}\rho V \tag{4.12}$$

where V is the volume of the particle.

4.2.5 Contact Forces

The interaction among particles and between particle and wall is considered using the Gran-Hertz-History model described in Sections 2.3.1 to 2.3.3 of Chapter 2. The model takes into account the normal contact force, the tangential contact force, viscous damping force and cohesive force.

The torque due to rolling friction and tangential force is also considered using the torque equations described in section 2.3.4.

4.3 Energy Equation

4.3.1 Fluid Phase

The energy equation for fluid phase is [67]:

$$\frac{\partial}{\partial t}\left(\rho c_p \alpha_f T_f\right) + \nabla\cdot\left(\rho c_p \alpha_f U T_f\right) = -\nabla\cdot\left(\alpha_f \, \mathrm{k}_f \, \nabla T_f\right) + \dot{S}_q + \frac{h_s A_s}{V_c}\left(T_f - T_s\right) \tag{4.13}$$

where c_p is the mean specific heat capacity of the fluid, k_f is the mean thermal conductivity of the fluid, $\dot{S}_\mathrm{q}$ is the source term due to evaporation, h_s is the mean convection heat transfer coefficient for particle, A_s is the surface area of the particle, V_c is the volume of the CFD cell and T_f and T_s is the temperature of fluid and particle respectively.

The convection heat transfer coefficient h_s is calculated using the Nusselt number correlation for particles in a stream of fluid [67].

$$Nu_s = 2 + 0.6\alpha_f{}^n Re_s^{1/2} Pr^{1/3} \qquad \text{Re}_s < 200 \qquad (4.14)$$

$$Nu_s = 2 + 0.5\alpha_f{}^n Re_s^{1/2} Pr^{1/3} + 0.02\alpha_f{}^n Re_s^{0.8} Pr^{1/3} \qquad 200 < \text{Re}_s < 1500 \qquad (4.15)$$

$$Nu_s = 2 + 0.000045\alpha_f{}^n Re_s^{1.8} \qquad \text{Re}_s > 1500 \qquad (4.16)$$

where n = 3.5, $Nu_s = h_s d/k_f$, $Re_s = \rho d|\mathbf{U}\text{-}\mathbf{u}_p|/\mu$ and $Pr = \mu c_p/k_f$.

4.3.2 Solid Phase

Heat transfer between particles is also taken into consideration [20].

$$\dot{Q}_{cond,i-j} = h_{c,i-j}\Delta T_{i-j} \qquad (4.17)$$

$$h_{c,i-j} = \frac{4k_{si}k_{sj}}{k_{si}+k_{sj}}\left(A_{contact,i-j}\right)^{1/2} \qquad (4.18)$$

where $h_{c,i\text{-}j}$ is heat transfer coefficient due to conduction, $\Delta T_{i\text{-}j}$ is the temperature difference between particle i and j, k_{si} is the thermal conductivity of particle i and $A_{contact,\ i\text{-}j}$ is the contact area for particle i and j.

The particle temperature is finally calculated as follow:

$$m_s c_{ps}\frac{dT_{s,i}}{dt} = h_s A_s\left(T_f - T_s\right) + \sum_{contacts\ i-j}\dot{Q}_{cond,i-j} \qquad (4.19)$$

4.3.3 Phase Change

The heat flux at the phase boundary for deviation of interfacial temperature T_i from T_{sat} is given as [68],

$$q_{ev} = h_{ev}\left(T_i - T_{sat}\right) \tag{4.20}$$

where q_{ev} is the heat flux due to evaporation and h_{ev} is the interfacial vaporization heat transfer coefficient. It is given by [68],

$$h_{ev} = \frac{2C_e}{2 - C_e} h_e^{\,2} \sqrt{\frac{M_w}{2\pi R_{gas}}} \frac{\rho_2}{T_{sat}^{\,3/2}} \tag{4.21}$$

where C_e is the evaporation coefficient, h_e is the enthalpy of vaporization, ρ_2 is the density of vapor, R_{gas} is the universal gas constant and M_w is the molecular mass of water. The gradient of the volume fraction field α_1 is zero everywhere except at the interface. The interfacial area can be calculated by taking the volume integral of the magnitude of the α_1 field over a region encompassing the interface [68]. This gives us a way to define the evaporation source term $\dot{S}_q$ and $\dot{S}_v$ based on equation (22). And the temperature source term due to evaporation is

$$\dot{S}_q = q_{ev} \int_V \left|\nabla \alpha_1\right| dV / V \tag{4.22}$$

The mass source term due to evaporation is

$$\dot{S}_v = \dot{S}_q / \rho_f h_e \tag{4.23}$$

4.4 Particle Relaxation Time

In coupled calculations the ability of a particle to follow the fluid flow also needs to be considered when deciding the time step. The particle relaxation time provides a measure for this quantity.

$$\tau_p = \frac{\rho_s d^2}{18\mu_l}\left(1+0.15\,\mathrm{Re}_s^{0.687}\right)^{-1} \tag{4.24}$$

Crowe et al [69] derive this time value by considering the equation of motion of a spherical particle in the limit of low Reynolds number flow.

4.5 Algorithm

The algorithm for solving the coupled VOF-DEM is as follows:

1. The particles' positions, velocities and temperatures are determined by DEM.
2. Void fraction and mean particle velocities for each cell in the CFD mesh are determined.
3. Based on the information of α_f and particle fluid relative velocity the momentum exchange term is calculated.
4. VOF solver solves the fluid flow.
    a. The alpha transport equation is first solved.
    b. The momentum equation matrix is constructed.
    c. The velocity field is predicted without considering the pressure gradient at this stage.
    d. The pressure equation is solved.
    e. The velocity field is corrected with the new pressure field and the phase fraction alpha is updated.
    f. The transport equations for turbulence quantities are solved.
5. The fluid forces acting on the particles are calculated and sent to the DEM solver.
6. At the same time the data for the heat transferred to the particles is sent to DEM.

7. The whole process is repeated from 1.

4.6 Physical Model

In this study 4500 particles each with a radius of 5 µm are initially suspended in liquid water film without touching each other. The size of the CFD domain is 6 mm × 6 mm × 6 mm. Liquid water filled the container to a height of 0.5 mm. To prevent the influence of side walls, periodic boundary condition is applied in lateral directions. The time step for the DEM case is 1×10^{-8} s whereas the time step for the CFD case is 1×10^{-5} s which means that for each CFD iteration DEM runs for 1000 iterations. Smaller time step for DEM is applied to prevent any unrealistic overlap between particles during collisions. The entire CFD domain is kept at a temperature of 373.15 K initially with the exception of bottom wall which is kept at a temperature of 378.15 K for all the time.

Figure 4-1 shows the initial configuration of the fluids and particles.

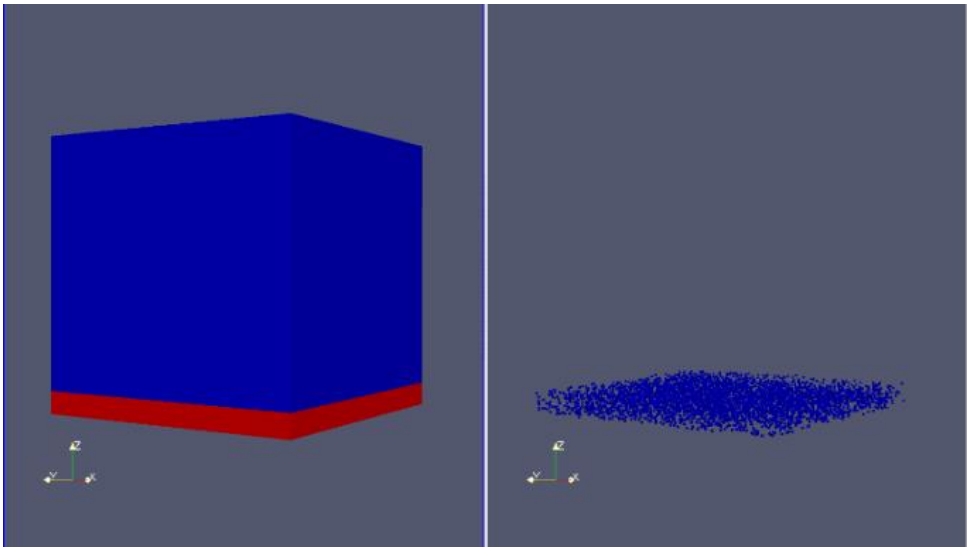

Figure 4-1 Fluid and particle configuration at time t = 0 s

4.7 Material Properties and Simulation Parameters

Table 4-1 Simulation parameter and properties

Parameters	Values	Parameters	Values
CFD domain size, mm×mm×mm	6×6×6	Specific heat of water (liquid), c_{p1}	4219 J/kg K
CFD cell size, mm×mm×mm	0.1×0.1×0.1	Specific heat of vapor, c_{p2}	2060 J/kg K
CFD time step	1×10^{-5} s	Specific heat of particle, c_{ps}	450 J/kg K
DEM time step	1×10^{-8} s	Surface tension of water, σ	0.07 N/m
Particle number	4500	Evaporation coefficient, C_e	0.1
Particle radius	5×10^{-6} m	Saturation temperature, T_{sat}	373.15 K
Particle density, ρ_s	7.87×10^{3} kg/m^3	Young's modulus, E	200×10^{9} N/m^2
Water (liquid) density, ρ_1	958.4 kg/m^3	Restitution	0.75

		coefficient, e	
Vapor thermal conductivity, k_{f2}	0.0246 W/m K	Poison ratio, σ	0.29
Particle thermal conductivity, k_s	80 W/m K	Surface energy density, γ	0.280 J/m^2
Universal gas constant, R	8.314 J/mol K	Water (liquid) viscosity, μ_1	2.82×10^{-4} N s/m^2
Mean free path of water, λ	2.5×10^{-10} m	Vapor viscosity, μ_2	1.27×10^{-5} N s/m^2
Surface tension of water, σ	0.07 N/m	Molecular mass of water, M	18.052×10^{-3} kg
Vapor density, ρ_2	0.586 kg/m^3	Evaporation coefficient, C_e	0.1
Sliding friction coefficient, μ_s	0.42	Rolling friction coefficient, μ_r	2×10^{-4}
Water (liquid) thermal conductivity, k_{f1}	0.691 W/m K		

4.8 Results and Discussion

Figure 4-2 shows evaporation of water film from the surface. Liquid water is found to be completely evaporated at about 2.17 sec which means that evaporation still continues after the particles settle down. Particles are found to be completely settled at

around 1 s which is much longer than the theoretical value to fall down if there is no water film. This is expected since there are drag force and buoyant force acting on the particles.

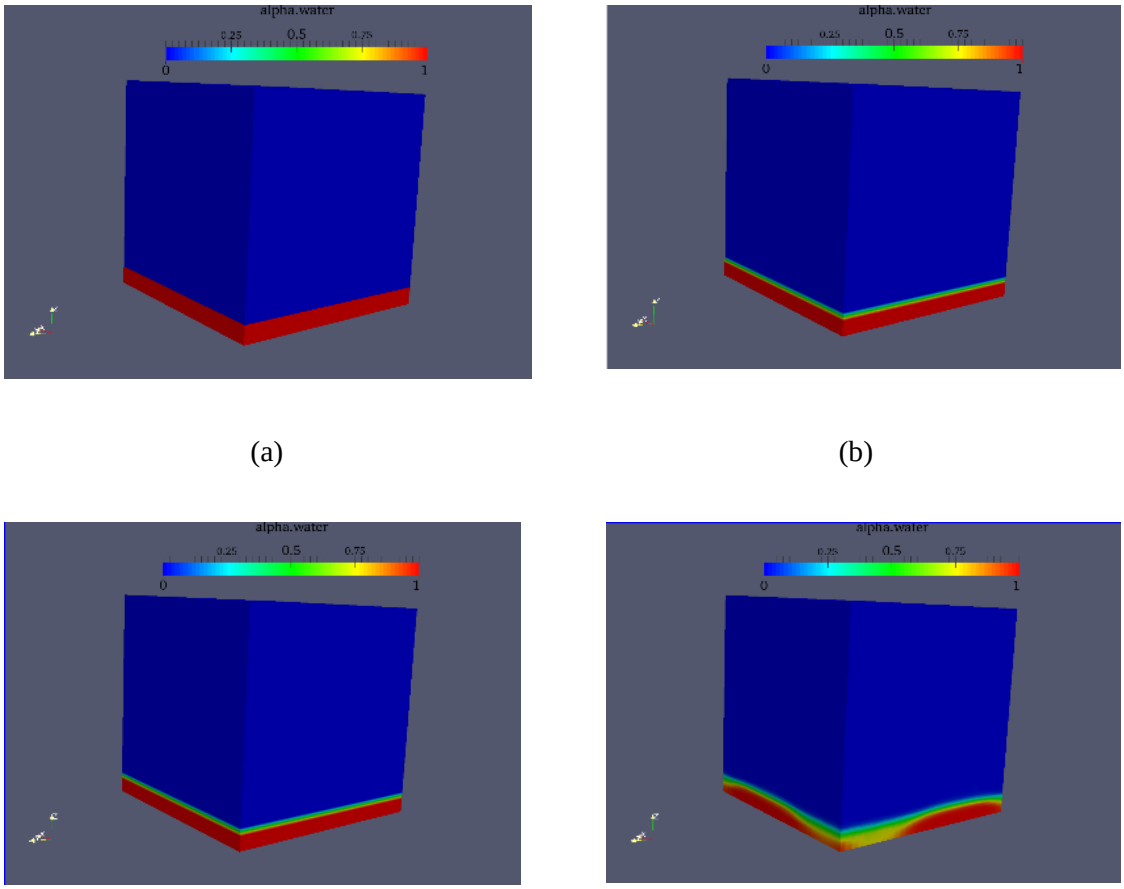

Figure 4-2 Volume fraction alpha1 at (a) 0 s (b) 0.529 s (c) 1.39 s and (d) 2.04 s

Figure 4-3 shows the packing structure of the particles after they settled down at the bottom of the container. It can be seen that packing configuration tends to form a pattern with the particles agglomerated in a special way. This clustering of particles continues as the water continues to evaporate.

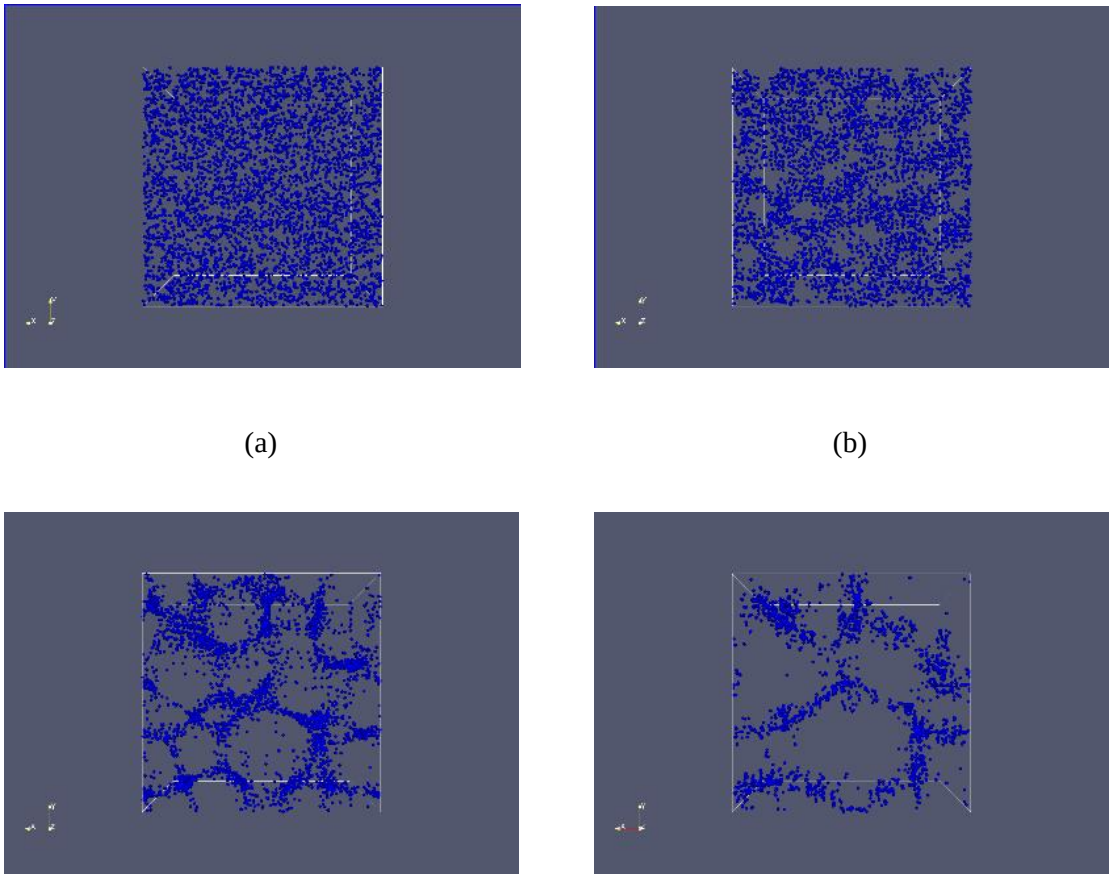

Figure 4-3 Arrangement of particles at (a) 1 s (b) 1.9 s (c) 2.0 s and (d) 2.1 s

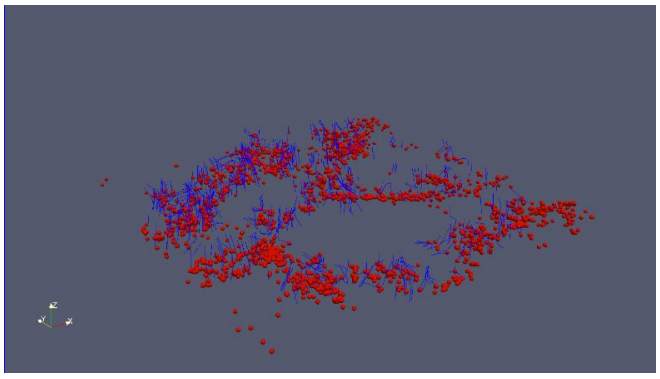

Figure 4-4 Streamlines of resultant implicit forces on particles

Figure 4-4 shows the streamlines (blue lines) of the resultant forces acting on the particles at 2 s. It can be seen that lines are prominent around the particle clusters. To characterize the packing structure of the particles, the distribution of coordination number and radial distribution function (RDF) are taken into account. To define particles that are touching each other a critical distance equal to $1.01(r_1+r_2)$, where r_1 and r_2 are the radii of two particles, is set.

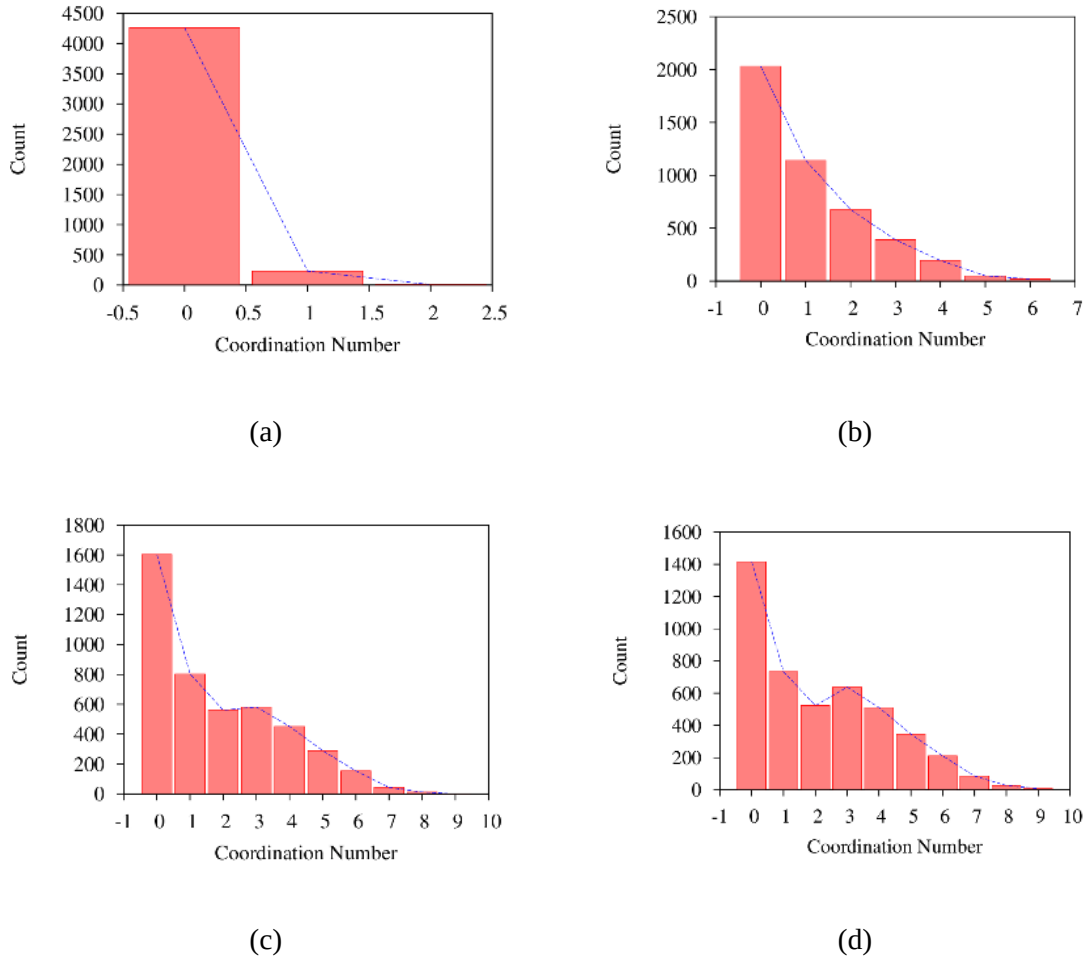

Figure 4-5 Distribution of coordination number at (a) 1 s (b) 2.05 s (c) 2.135 s and (d) 2.167 s

Coordination numbers of the particles are calculated based on the assumption that if the center-to-center distance between two particles is less than this critical distance then the particles are considered as touching each other.

Figure 4-5 shows the distribution of coordination number at various times. At time equal to 1 s particles settled down at the bottom but they are barely touching each other. This can be easily seen from the **Figure 4-5** (a) where most particles are shown to have a zero coordination number. At time equal to 2.05 s there is a gradual rise in coordination number which shows that some particles are touching and coming closer to each other. At times equal to 2.135 s and 2.167 s coordination numbers as high as 8 or 9 are observed. This means that some particles are sitting in a closed packed region.

Another parameter which is used to analyze the packing structure is the radial distribution function (RDF). It describes the probability to find a particle in a shell *dr* at a distance r from another reference particle.

$$g(\mathrm{r}) = \frac{V}{N}\frac{dN(\mathrm{r})}{4\pi r^2 dr} \tag{4.25}$$

where V represents the total volume occupied by particles, N is the total number of particles, and $dN(r)$ is the number of particles in a shell of width dr at distance r from the reference particle. RDF at time equal to 1 s shown in the **Figure 4-6** (a) shows no peak since the particles are not touching each other. At time 2.05 s RDF shows peaks indicating the fact that particles are now forming clusters. A closer look at the peaks reveals that there are actually three peaks. The first peak is at $2r$ which corresponds to the one to one contact configuration. The second and third peak are at $2\sqrt{2}r$ and $4r$ which correspond to the edge-sharing-in-plane equilateral triangle and three particles centers in

a line contact type. The peak values of RDF continue to change as the particle packing structure changes.

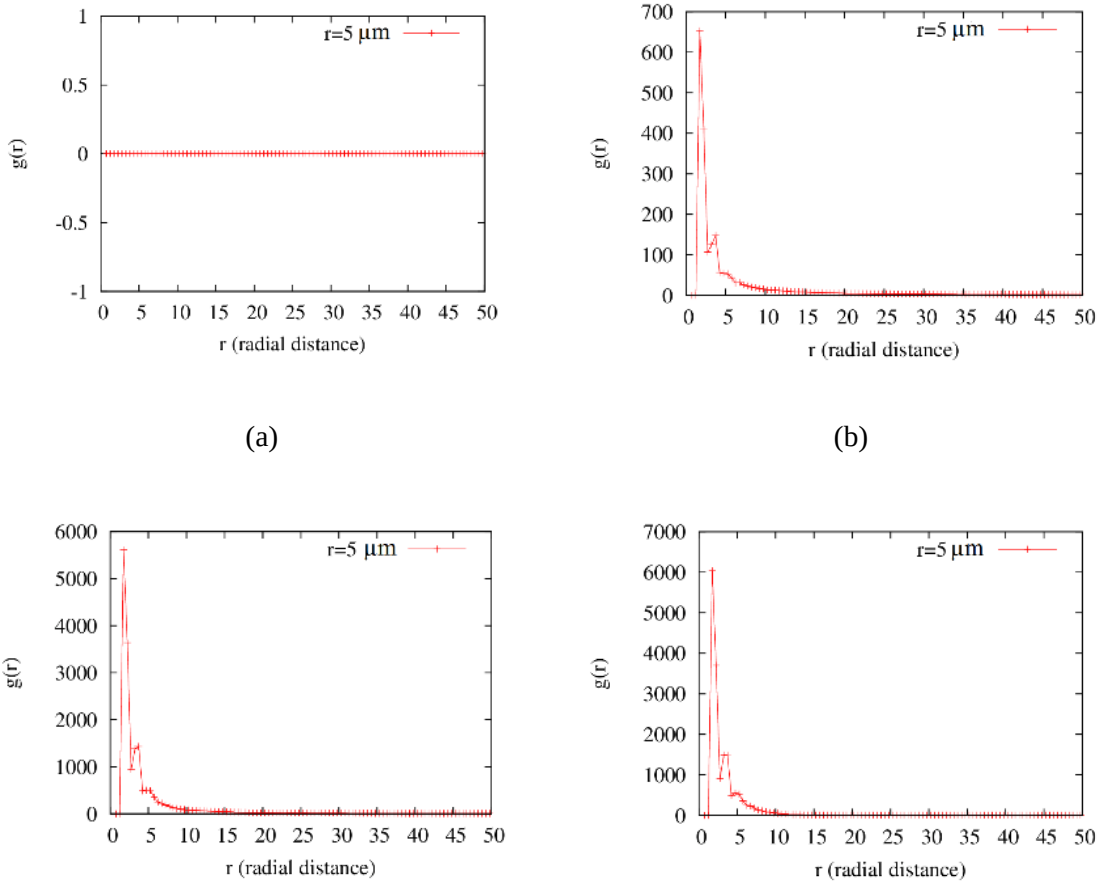

Figure 4-6 Radial distribution function (RDF) at (a) 1 s (b) 2.05 s (c) 2.135 s and (d) 2.167 s

4.9 Conclusion

A numerical investigation on evaporation induced self-assembly of sub-micron particles is carried out using a coupled VOF-DEM approach. The interaction between fluid and particle is thoroughly considered by taking into account the momentum exchange and heat transfer between particle and fluid. In the simulation liquid water film

is allowed to evaporate and leave the particles at the container alone. Interesting patterns are seen to emerge as the liquid water film evaporates. The resulting packing structure is analyzed in terms of the range of coordination number and radial distribution function which also indicate the self-assembly of the particles.

5 EVAPORATION INDUCED SELF-ASSEMBLY OF ROUGH COLLOIDS: A VOF-DPD STUDY

5.1 Introduction

This chapter discusses modifications to the study in the previous chapter. A new evaporation model is developed that calculates the mass flux at the interface directly from the concentration gradient of species.

After the introduction, the first part of the paper deals with the development of the finite volume solver that accounts for phase change and heat transfer. The boundary condition used to achieve pinning is also discussed. Then the coupling between the LS and the VOF method is discussed. After that, the coupling between the DPD and the fluid solver is discussed followed by some validation test results. Finally, the results for the self-assembly process are presented and discussed. To analyze the texture of the deposited pattern, a First Order Statistics (FOS) method is presented and discussed.

5.2 Methodology

5.2.1 Volume of Fluid (VOF) Model

In the VOF method, the liquid and vapor or gaseous phases are treated as a "single" fluid whose properties change sharply at the phase boundary. A volume fraction variable α is used to denote the liquid fraction which changes as follows,

$$\alpha = \begin{cases} 0 & \text{In gaseous phase (air or vapor)} \\ 0 < \alpha < 1 & \text{In cells with the liquid interface} \\ 1 & \text{In liquid phase} \end{cases} \tag{5.1}$$

Source terms are added to the advection equation for α to account for evaporation and change in density due to external heating.

$$\frac{\partial \alpha}{\partial t} + \nabla \cdot \left(\alpha \mathbf{U} \right) = \frac{\dot{m}}{\rho} - \frac{\alpha}{\rho} \frac{D\rho}{Dt} \tag{5.2}$$

where $\mathbf{U}$ is the fluid velocity, $\dot{m}$ is the evaporation flux and ρ is the fluid density. This equation is solved in two steps. In the first step, the interface is tracked and advected, without the source terms, using the "isoAdvector" library developed by Roenby et al. [70]. The "isoAdvector" method reconstructs the interface using a geometric approach and is shown to be superior to the MULES (Multidimensional Universal Limiter with Explicit Solution) scheme [71], available in OpenFOAM, in terms of interface sharpness, volume conservation, and efficiency. In the second step, the source terms are included to solve the alpha equation,

$$\frac{\partial \alpha}{\partial t} = \frac{\dot{m}}{\rho} - \frac{\alpha}{\rho} \frac{D\rho}{Dt} \tag{5.3}$$

A single momentum equation is solved for the entire system,

$$\frac{\partial \left(\rho \mathbf{U} \right)}{\partial t} + \nabla \cdot \left(\rho \mathbf{U}\, \mathbf{U} \right) = \nabla \cdot \mu \left(\nabla \mathbf{U} + \nabla \mathbf{U}^{\mathrm{T}} \right) - \nabla p_{rgh} - \mathrm{g} \cdot \mathbf{r} \nabla \rho \tag{5.4}$$

where $p_{rg} = p - \rho \mathrm{g} \cdot \mathbf{r}$, p is the pressure, g is the gravitational acceleration and $\mathbf{r}$ is the position vector.

The continuity equation for the VOF model considers the volume change at the interface due to evaporation and the density variation,

$$\frac{1}{\rho} \frac{D\rho}{Dt} + \nabla \cdot \left(\mathbf{U} \right) = \dot{m} \left(\frac{1}{\rho_L} - \frac{1}{\rho_G} \right) \tag{5.5}$$

The energy equation for the VOF model is,

$$\rho c_p \left(\frac{\partial T}{\partial t} + \mathbf{U} \bullet \nabla T \right) = \nabla \bullet \left(k \nabla T \right) + \beta \frac{Dp}{Dt} - \sum_{i=1}^{N_s} \mathbf{j}_i c_{p,i} \nabla T - \sum_{i=1}^{N_{sL}} \dot{m}_i h_{v,i} \tag{5.6}$$

where the second term on the right is the source term due to density variation, the third term is the source term for sensible heating, and the fourth term is the source term due to evaporation. k is the thermal conductivity of the fluid, β is the thermal expansion coefficient, c_p is the specific heat and h_v is the enthalpy of vaporization. The third term, $\mathbf{j}_i$ are the diffusion fluxes which depend on the mole fraction gradients of the species.

The species equations for the gaseous and liquid phases are:

$$\frac{\partial \rho \tilde{\omega}_i^G}{\partial t} + \nabla \bullet \left(\rho \mathbf{U} \tilde{\omega}_i^G \right) = -\nabla \bullet \mathbf{j}_i^G \tag{5.7}$$

$$\frac{\partial \rho \tilde{\omega}_i^L}{\partial t} + \nabla \bullet \left(\rho \mathbf{U} \tilde{\omega}_i^L \right) = -\nabla \bullet \mathbf{j}_i^L + \dot{m}_i \tag{5.8}$$

where ω is the mass fraction with superscripts *G* and *L* denoting gas and liquid. The mass evaporation flux can be calculated from the interface concentration gradient of the vapor at the liquid-vapor interface. In order to do so, the diffusion coefficients need to be accounted for first. The diffusion coefficients D_i for each species comprising the mixture are calculated as [72, 73],

$$D_i = \frac{\sum_{j \neq i} y_i M_{w,j}}{M_w \sum_{j \neq i} \frac{y_i}{D_{i,j}}} \tag{5.9}$$

where the diffusion coefficients are calculated based on the binary diffusion coefficients, $D_{i,j}$ and the mole fractions, y_i which is also used to calculate the diffusion velocities, $\mathbf{v}_{d,i}$.

$$\mathbf{v}_{d,i} = -D_i \frac{\nabla y_i}{y_i} \tag{5.10}$$

The diffusion flux is then obtained as [73],

$$\mathbf{j}_i = \rho\, \tilde{\omega}_i \mathbf{v}_{d,i} = -\rho\, \tilde{\omega}_i D_i \frac{\nabla y_i}{y_i} = -\rho\, D_i \frac{M_{w,i}}{M_w} \nabla y_i \tag{5.11}$$

where $M_{w,i}$ is the molar mass of species *i* and M_w is the overall molar mass.

5.2.2 Thermodynamic equilibrium

For high fidelity modeling of the phase change process, it is important to consider the equilibrium thermodynamics of the system at the phase boundary. The vapor-liquid equilibrium condition at the interface of a two-phase system is [73, 74]:

$$p_i^0(T)\, x_i \tilde{\phi}_i\left(T, p_i^0\right) e^{\int_{p_i^0}^{p} \frac{v_{L,i}}{RT} dp} = p y_i \hat{\phi}_i\left(T, p, y_i\right) \tag{5.12}$$

where $p_i^0(T)$ is the vapor pressure of species *i*, $\tilde{\phi}_i\left(T, p_i^0\right)$ is the gas-phase fugacity coefficient for the pure species, and $\hat{\phi}_i\left(T, p, y_i\right)$ is the gas-phase mixture fugacity coefficient. The exponential term is the Poynting correction where the molar volume $v_{L,i}$ is calculated as:

$$v_{L,i} = \frac{M_{w,i}}{\rho_L} \tag{5.13}$$

The x_i and y_i are the liquid and gas mole fractions of species *i*. The above equation is rearranged to found y_i,

$$y_i = \frac{p_i^0(T)\, \tilde{\phi}_i\left(T, p_i^0\right) e^{\int_{p_i^0}^{p} \frac{v_{L,i}}{RT} dp}}{p \hat{\phi}_i\left(T, p, y_i\right)} x_i \tag{5.14}$$

as well as the equilibrium gaseous mass fraction, ω_i,

$$\tilde{\omega}_i = \frac{M_{w,i}}{M_w} y_i \tag{5.15}$$

This saturation mass fraction is assigned to the whole liquid phase and then advected in the gas phase through Eq. (7) according to the scheme used in [75].

5.2.3 Evaporation rate

The volumetric rate of evaporation for each liquid species, $\dot{m}_i$ is directly calculated by equating the gas and liquid species mass fluxes (sum of diffusive and convective) across the interface [72]:

$$\dot{m}\tilde{\omega}_i^L + \mathbf{j}_i^L \bullet \nabla\alpha = \dot{m}\tilde{\omega}_i^G + \mathbf{j}_i^G \bullet \nabla\alpha \tag{5.16}$$

For mono-component liquids, $\mathrm{j}_i^L = 0$ and $\omega_i^L = 1$, hence,

$$\dot{m} = \dot{m}\tilde{\omega}_i^G + \mathbf{j}_i^G \nabla\alpha \tag{5.17}$$

The total evaporation rate, $\dot{m}$, is then [76],

$$\dot{m} = \frac{\mathbf{j}_i^G}{1-\tilde{\omega}_i^G}\nabla\alpha \tag{5.18}$$

which is also the $\dot{m}_i$ for mono-component liquids. If the dot product $\mathbf{j}_i^G \bullet \nabla\alpha$ is negative, $\dot{m}$ will be negative indicating evaporation, otherwise, there will be condensation ($\dot{m} > 0$). For multi-component liquids, the total evaporation rate is obtained by summing over all the liquid species, N_{sL} on both sides of the species balance equation.

$$\dot{m} = \frac{\sum_{i=1}^{N_{sL}} \mathbf{j}_i^G}{1-\sum_{i=1}^{N_{sL}} \tilde{\omega}_i^G}\nabla\alpha \tag{5.19}$$

For multi-component liquids, the evaporation flux of each liquid species, $\dot{m}_i$ required for the liquid species equation can be found once the total evaporation flux is found,

$$\dot{m}_i = \mathbf{j}_i^G \nabla\alpha + \dot{m}\tilde{\omega}_i^G \tag{5.20}$$

Now, the calculation of the dot product $j_i^G \bullet \nabla\alpha$ requires special consideration because the term $|\nabla\alpha|$ is zero everywhere except at the interface cells. On the other hand, the diffusion flux, j_i^G, must be computed at the gas/vapor cells adjacent to the interface cells. Using an algorithm developed by Saufi et al. in [73], every cell at the interface is paired with the closest gaseous phase cell along the interface normal to calculate the volumetric evaporation rate according to equation (21). **Figure 5-1** shows the schematic of the procedure.

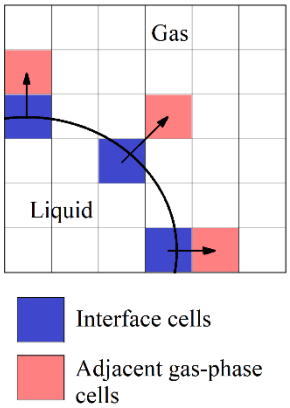

Figure 5-1 Scheme for calculating $j_i^G \bullet \nabla\alpha$

$$\dot{m}_{\text{int}} = \frac{\sum_{i=1}^{N_{sL}} \mathbf{j}_{i,adj}^G}{1 - \sum_{i=1}^{N_{sL}} \tilde{\omega}_{i,\text{int}}^G} |\nabla\alpha|_{\text{int}} \tag{5.21}$$

where the subscript int refers to the interface cells.

When solving α equation (3) using the evaporation source term, it is possible for α to reach negative values in certain cells, particularly if $\dot{m}$ is high. Following the procedure developed in [73], the total evaporation rate $\dot{m}$ is multiplied with a special function of α which forces $\dot{m}$ to zero when α approaches zero.

$$\dot{m} = Kf\left(\alpha\right)\frac{\sum_{i=1}^{N_{sL}} \mathbf{j}_{i,adj}^{G}}{1-\sum_{i=1}^{N_{sL}} \tilde{\omega}_{i,\text{int}}^{G}}\left|\nabla\alpha\right|_{\text{int}} \tag{5.22}$$

where $f\left(\alpha\right)$ is the special function,

$$f\left(\alpha\right) = \sqrt{\alpha\left(1-\alpha\right)} \tag{5.23}$$

and *K* is the normalization constant obtained by integrating $\dot{m}$ over cell volumes.

$$K = \frac{\int_V \dot{m}dV}{\int_V f\left(\alpha\right)\dot{m}dV} \tag{5.24}$$

5.2.4 Fluid properties

The thermodynamics and transport properties of gases (diffusion coefficients, thermal conductivity, heat capacities, and viscosity) are calculated based on the correlations available in the OpenSMOKE++ library [77]. The liquid properties (vapor pressure, density, conductivity, heat capacity, viscosity, and vaporization heat) are evaluated based on the correlations provided by the built-in OpenFOAM database [78]. The mixture properties, on the other hand, are evaluated based on the mixing rule commonly employed in VOF [72, 73, 75, 76]. The viscosity, for example, is,

$$\mu = \mu_L\alpha + \mu_G\left(1-\alpha\right) \tag{5.25}$$

5.2.5 Contact-line pinning

It is important to pin the contact-line of the droplet for the entire evaporation time to create a strong radially outward flow and create a coffee-ring pattern of the polymer deposits. However, the wall boundary conditions provided in OpenFOAM do not have the option to pin the contact line of the droplet for the entire simulation. OpenFOAM uses a Neumann BC to correct the contact angle in the case of a constant contact angle BC.

The idea is to rotate the gradient of the volume fraction at the boundary face to align the interface to a given contact angle given by the boundary condition.

$$\mathbf{n}_I \bullet \nabla\left(\alpha_I\right)_b = \cos\theta \tag{5.26}$$

where $\mathbf{n}_I$ is the interface normal, $\nabla\left(\alpha_I\right)_b$ is the gradient of α at the interface at the boundary face and θ is the contact angle. It also has a dynamic contact angle BC which calculates the interface velocity before correcting the contact angle depending on the contact model at every time step.

However, a Neumann BC alone cannot fix the contact line at the boundary face. For the contact line to remain pinned, the value of the volume fraction at the boundary face should not change with time. A Neumann BC does not fix the volume fraction but only the gradient. Dupont et al. used a momentum balance method to pin the contact line for their code JADIM [79]. Their method involves calculating an intermediate velocity U*. They achieve pinning by computing the angle θ* that cancels the local momentum balance by taking into account the surface tension force in the cells adjacent to the wall and intersected by the interface. On the other hand, Linder [80] used a mixed BC for implementing a dynamic contact angle model with hysteresis. His model has a switching factor that switches his BC from Neumann to Dirichlet based on the current calculated contact angle. If the current contact angle is within the hysteresis, the Dirichlet BC is switched on fixing the volume fraction at the boundary face. With this, he achieved hysteresis and some pinning during droplet motion.

Inspired by the work of Linder [80], a Dirichlet BC is used in this study to fix the contact line at the boundary face. This is much simpler to implement than the method

outlined by Dupont et al. [79] and the contact line remained pinned throughout the evaporation stage.

5.2.6 Coupling Volume of Fluid with Level Set method (CVOFLS)

One of the common problems of the VOF method is the emergence of spurious current near the interface of dissimilar phases. Spurious or parasitic currents are artificial oscillations in the velocity field in the vicinity of the interface in multi-phase flow problems, which arise from an imbalance between discretized forces at the interface. They are also accompanied by unwanted pressure fluctuations. As shown later in this paper, the polymer particles arrange themselves around the liquid interface based on the interface forces on the particle. The spurious current will create spurious forces on the particle near the interface which is unacceptable. Hence, the VOF method used in this work is coupled with the level set method following the procedure developed by Albadawi et al. [81] where the level set function is reinitialized after the volume fraction values. The initial level set function is defined by

$$\psi_0 = \left(2\alpha - 1\right)\Gamma \tag{5.27}$$

where Γ is a non-dimensional number and its value is defined by using the grid spacing Δx as,

$$\Gamma = 0.75\Delta x \tag{5.28}$$

The initial level set function is then used to calculate the following reinitialization equation to improve curvature computations of the interface and its normal direction:

$$\begin{aligned} &\frac{\partial \psi}{\partial t} = Sign\left(\psi_0\right)\left(1 - \left|\nabla \psi\right|\right) \\ &\psi\left(\mathbf{x}, 0\right) = \psi_0\left(\mathbf{x}\right) \end{aligned} \tag{5.29}$$

where ψ is the Level Set function and *Sign*() is the sign function.

Next, the density-scaled balanced surface tension force model proposed by Yokoi [82] is used to calculate the surface tension force,

$$F_{\sigma,\psi} = \sigma k_{\psi} \nabla H^{scaling} \tag{5.30}$$

where σ is the surface tension of liquid, k_{ψ} is the interface curvature and $H^{scaling}$ is the non-symmetrical smoothed Heaviside function given as

$$H^{scaling} = \begin{cases} 0 & \psi < -\varepsilon_{\text{int}} \\ \frac{1}{2}\left[\frac{1}{2} + \frac{\psi}{\varepsilon_{\text{int}}} + \frac{\psi^2}{2\varepsilon_{\text{int}}^2} - \frac{1}{4\pi^2}\left(\cos\left(\frac{2\pi\psi}{\varepsilon_{\text{int}}} \right) - 1 \right) + \frac{\varepsilon_{\text{int}} + \psi}{\varepsilon_{\text{int}}\pi} \sin\left(\frac{\pi\psi}{\varepsilon_{\text{int}}} \right) \right] & |\psi| \le \varepsilon_{\text{int}} \\ 1 & \psi > \varepsilon_{\text{int}} \end{cases} \tag{5.31}$$

and ε_{int} is the interface thickness given as,

$$\varepsilon_{\text{int}} = \varepsilon_c \Delta x \tag{5.32}$$

where ε_c is the interface thickness coefficient take as 1.5 following Albadawi et al. [81].

5.2.7 DPD Model

The acceleration of the ith particle is modeled by the following Langevin equation [83, 84],

$$\begin{aligned} m_i \dot{\mathbf{u}}_i = m_i \left(\dot{\mathbf{U}} + \left(\mathbf{u}_i \bullet \nabla \right) \mathbf{U} \right) + \mathbf{F}_{ij}\left(r_{ij} \right) + \mathbf{F}_{si}\left(r_{si} \right) \\ + \mathbf{F}^{\text{n}}{}_{ij} + \mathbf{F}^{\text{t}}{}_{ij} + \mathbf{F}_{ci}\left(r_i \right) + \mathbf{F}_{di}\left(\mathbf{u}_i \right) + \mathbf{F}_{bi} \end{aligned} \tag{5.33}$$

where m_i is the mass of the ith particle, $\mathbf{u}_i$ is the velocity of the ith particle, the first term on the right-hand side is the hydrodynamic force, and $\mathbf{F}_{ij}$ is the sum of the conservative forces between pairwise interaction between particles i and j. $\mathbf{F}_{\text{si}}$ is the long-range force between the substrate and particle i, $\mathbf{F}^{\text{n}}{}_{ij}$ and $\mathbf{F}^{\text{t}}{}_{ij}$ are the normal and tangential forces

due to substrate roughness, $\mathbf{F}_{ci}$ is the force on particle i by the liquid interface, $\mathbf{F}_{di}$ is the drag force due to relative velocities of fluid and particle i, and $\mathbf{F}_{bi}$ is the Brownian force.

5.2.7.1 Pairwise Force

The pairwise force is given by the pair potential U(ij) as,

$$\mathbf{F}_{ij}\left(r_{ij}\right) = -\nabla \sum_{i \neq j}^{N} U\left(r_{ij}\right) \tag{5.34}$$

where the pair potential $U\left(r_{ij}\right)$ is defined, according to the DLVO theory, as a sum of two potentials, the Coulomb repulsion, and van der Waals interaction, respectively [83, 84].

$$U\left(r_{ij}\right) = U_c\left(r_{ij}\right) + U_{vdw}\left(r_{ij}\right) \tag{5.35}$$

In this study, the polymeric nanoparticles are assumed to be coated with atoms that dissociate in liquid and make the nanoparticles charged. This helps prevent the nanoparticles from coagulating. The Coulombic repulsion between charged colloids in aqueous solution is given by the Yukawa potential for colloids as [85],

$$U_c\left(r_{ij}\right) = \frac{64\pi k_B T \rho_\infty Rad \psi_0^2}{\kappa^2} e^{-\kappa\left(r_{ij} - 2Rad\right)} \tag{5.36}$$

where ρ_∞ is the bulk electrolyte concentration, κ is the inverse Debye screening length, and ψ_0 is the electric potential at the particle surface, which is related to surface charge as,

$$\psi_0 = \frac{\phi}{\kappa \in \in_0} \tag{5.37}$$

where ϕ is the surface charge which is taken as 1000 elementary charge per micro-meter squared, $\in$ is the permittivity of free space, and $\in_0$ is the relative permittivity of an aqueous solution.

The van der Waals interaction potential between two nanoparticles of radius *a* is given by [83-85],

$$U_{vdw}\left(r_{ij}\right)=-\frac{Ha}{6}\left[\frac{2Rad^2}{r_{ij}^2-4Rad^2}+\frac{2Rad^2}{r_{ij}^2}+\ln\left(1-\frac{4Rad^2}{r_{ij}^2}\right)\right]+U_{hc}\left(r_{ij}\right) \tag{5.38}$$

where *Ha* is the Hamakar constant and $U_{hc}\left(r_{ij}\right)$ is the hard-core repulsive potential that prevents overlap between two spheres of radius *Rad*. Table 1 gives the values of *Ha* and other constants for the potential functions.

5.2.7.2 Substrate Long-range Force

The interaction force between nanoparticles and substrate is given by the particle-wall interaction potential which has an attractive part and a repulsive part [86].

$$\mathbf{F}_{si}\left(r_{si}\right)=-\nabla U_{wall}\left(r_{si}\right) \tag{5.39}$$

where

$$\begin{aligned}U_{wall}\left(r_{si}\right)=&\frac{\varepsilon_{LJ}\sigma_{LJ}{}^6}{7560}\left(\frac{6Rad-D}{D^7}+\frac{D+8Rad}{\left(D+2Rad\right)^7}\right)\\&-\frac{\varepsilon}{6}\left(\frac{2d\left(D+Rad\right)+D\left(D+2Rad\right)\left[\ln D-\ln\left(D+2Rad\right)\right]}{D\left(D+2Rad\right)}\right)\end{aligned} \tag{5.40}$$

where ε_{LJ} is effectively a Hamaker constant for the nanoparticle-wall interaction, *Rad* is the radius of the nanoparticle, *D* is the distance from the surface of the nanoparticle to the wall (r_{si} - *Rad*), and σ_{LJ} is the size of a constituent LJ particle inside the nanoparticle. The particle-wall interaction potential is obtained by integrating over LJ particles of size sigma that make up the nanoparticle and a 3d half-lattice of Lennard-Jones 12/6 particles of size sigma in the wall.

5.2.7.3 Introducing Substrate Roughness

One of the key features of this paper is to elucidate the effect of substrate roughness on the self-assembly of the colloidal particles. There has been a number of recent research [87-89] that discussed the interaction potential or force between colloid particles or between colloid and wall with roughness. Many of these research [87-89] report an increase in repulsive force between colloid particles or between particles and walls that cannot be accounted for by DLVO theory. The DLVO theory predicts a rise in attractive force due to Van der Waals interaction triumphing over the electrostatic repulsion. However, in the presence of surface roughness, a sharp increase in repulsive force is seen for small particle separation. Some researchers have attributed this to hydration force [90, 91] while others have argued that the hydration force alone cannot explain the rise in repulsive potential [87, 89]. Two main reasons have been presented for rough particles: first, the hydration force has a short-range ~0.3 nm whereas repulsive force is found to increase long before that 8~10 nm. Second, surface roughness actually decreases the effect of hydration since the surface asperities hinder the arrangement of molecules. For all these reasons, the effect of hydration is neglected in this study. However, the surface roughness is accounted for using two methods. In the first method, the direct particle contact is accounted for by a normal contact force. The force is given by a non-linear spring-dashpot model acting normal to the contact [92] given by equation (2.5) in Chapter 2. In the second method, the tangential force is accounted for by a linear spring-dashpot model limited by the Coulomb friction law [92] given by equation ((2.8) in Chapter 2.

The above two methods allow a simple but effective way to study the effect of surface roughness in the self-assembly of nanoparticles. It can be noted that a more rigorous way to account for surface roughness would be to follow the method used by Parson et al. [87], which is to assume a probability distribution for the roughness or the asperity heights and derive the corresponding distribution for surface stress.

$$F\left(\xi\right) = 2\pi \bar{\mathrm{R}} \int_{-\infty}^{\infty} P_m\left(h_g\right) G_{smooth}\left(h_g + \xi\right) dh \tag{5.41}$$

where ξ is the average separation distance between surfaces of two particles, h_g is the asperity heights, $P_m\left(h_g\right)$ is the mean probability distribution of h_g. G_{smooth} is the interaction energy between surfaces if they are perfectly smooth. If $P_m\left(h_g\right)$ follows a normal distribution then

$$P_m\left(h_g\right) = \frac{e^{\left(-h_g{}^2/2\sigma_m^2\right)}}{\sigma_m\sqrt{2\pi}} \tag{5.42}$$

where σ_m is the mean roughness.

However, the above method would be more suitable when actual data for surface roughness for a given system is available. Also, the above method only considered elastic deformation of the asperities [87]. Some asperities can be permanently deformed leading to a loss of impact energy. Hence, a contact model accounting for the loss of energy is preferred. For this study, it is deemed sufficient to model the effect of surface roughness in a more straightforward way using the contact models described in Eqs. (44) and (45).

5.2.7.4 Drag Force

The drag force for the spherical nanoparticles is given by Stokes' drag equation.

$$\mathbf{F}_{di}\left(\mathbf{u}_i\right) = -6\pi d\,\mu_l\left(\mathbf{u}_i - \mathbf{U}\right) \tag{5.43}$$

where μ_l is the dynamic viscosity of the liquid.

5.2.7.5 Interface Force

The interface force is a combination of four forces acting in the vicinity of the interface, two of them, the interface vdW force and the hydrodynamic forces are attractive in nature, while the other two, the interface drag force and the elastic force are repulsive in nature. The elastic force is only activated when the particle tries to leave the droplet while the other three forces are long-range forces that decay away from the interface. The total interface force is a sum of the four forces which act together to keep the particles inside the droplet.

$$\mathbf{F}_{ci} = F_{\text{int}} + F_{vdW} + F_{hydro} + F_{elas} \tag{5.44}$$

5.2.7.5.1 Interface Drag

When the polymer particles approach the droplet interface, the intervening liquid layer exerts a force on the particle opposing its movements. The description and derivation of this force can be found in the references [93, 94]. In this study, a modified Taylor equation of the interface drag force that closely follows the experimental results [95] and applied in [96] is used.

$$F_{\text{int}} = 6\pi\mu_l \mathbf{u}_r \frac{\bar{\text{R}}^2}{h_{int}} \tag{5.45}$$

where $\bar{\text{R}}$ is the reduced radius of the bubble and the particle and $\mathbf{u}_r$ is the radial velocity of approach of the particle to the bubble and h_{int} is the distance between particle surfaces. To apply Eq. (3), the radial velocity of the particle is obtained by taking components of the particle velocity in the direction of the interface normal. To avoid singularity, a cutoff is defined for minimum separation distance (minimum h_{int} = 0.5 nm). Since the force

acting on the particles are only in the radial direction, the particles can slide in the tangential direction of the interface of the droplet.

5.2.7.5.2 Interface Van der Waals force

Van der Waals interaction between particle and droplet interface is considered in the simulation. In this study, a simplified equation [96] of the attractive Van der Waals force between two particles originally developed by Hamaker [21] is used:

$$F_{vdW} = \frac{H\bar{\mathrm{R}}}{6h_{\mathrm{int}}^{\ 2}} \tag{5.46}$$

where H is the Hamaker constant, and h_{int} is the separation between the particle surface and droplet interface. The interface vdW force diverges as the particle approaches the interface, and hence the cut off distance has been included in the code to prevent this by setting the force to a constant once a certain distance has been reached (0.5 nm) [96].

5.2.7.5.3 Hydrophobic force

Hydrophobic forces are attractive forces that are stronger and decay more slowly than van der Waal forces [96]. In this work, a simplified model of the hydrophobic force is used taking those characteristics into account.

$$F_{hydro} = \frac{K_H}{h_{\mathrm{int}}} \frac{\mathbf{r}}{|\mathbf{r}|} \tag{5.47}$$

where K_H is a constant related to the strength of the hydrophobic interaction and $\mathbf{r}$ is the distance vector that points in the same direction as the interface normal. A cut-off value of 0.5 nm was considered to prevent division by zero. The cut-off represents a typical value where molecular interactions start to dominate over the macroscopic properties of the particles [96].

5.2.7.5.4 Elastic Contact force

For the particle-droplet interface contact, it has been shown by other researchers that the interaction may be quantitatively described over the whole distance regime by treating the fluid interface as an elastic spring [97]. Hence, the force arising from the deformation of the interface due to particles is modeled as an elastic force which is proportional to the deformation, δ as,

$$F_{elas} = k_n \delta_{\text{int}} \tag{5.48}$$

where k_n is the elastic coefficient, and δ_{int} is measured as the distance of the center of the particle from the interface measured in the direction of the outward interface normal; δ_{int} must be positive for F_{elas} to be considered.

5.2.7.6 Brownian Force

The Brownian force $\mathbf{F}_{bi}(t)$ is a Gaussian random force with zero mean and variance given by [83, 84]:

$$\left\langle \mathbf{F}_{bi}^2 \right\rangle = \frac{2\pi\mu_l d k_B T}{\tau} \tag{5.49}$$

where k_B is the Boltzmann constant, T is the temperature, and τ is the integration time step. The Brownian force can be ignored if the Brownian random displacement of the particle is less than the particle size during the evaporation time of the liquid.

5.2.8 Algorithm

The CVOFLS-DPD solver is developed using two open-source software packages, OpenFOAM for CVOFLS and LIGGGHTS for DPD.

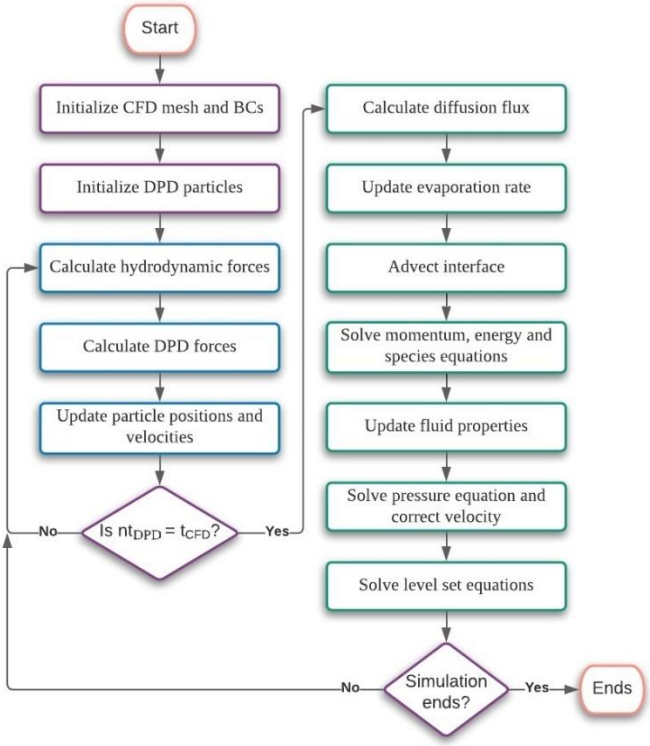

Figure 5-2 The algorithm for CVOFLS-DPD

The coupling between the two solvers is done using the CFDEM library which is also freely available. The simulation starts on the CFD side by initializing the mesh and boundary conditions. Then the DPD particles are introduced into the simulation domain. The DPD simulation uses the velocity-Verlet algorithm [98] and requires much smaller time steps than the CFD process. The time step for the DPD case is 1×10^{-9} s whereas the time step for the CFD case is 1×10^{-7} s which means that for each CFD iteration DPD runs for 100 iterations. After the DPD particle positions and velocities are updated, the CFD solver is switched on which calculates the evaporation source term and solves the transport equations. After one CFD step, using the new fluid velocity and interface, the fluid-particle forces are calculated and passed to the DPD solver. **Figure 5-2** shows the algorithm for the CVOFLS-DPD solver. The DPD steps are shown in blue, CFD steps in green and the coupling steps are shown in purple.

5.3 VALIDATION

5.3.1 Validation of the VOF Model

The VOF evaporation model is validated against the numerical results of Cuoci et al. [99] which have been validated over a wide range of operating conditions by other researchers [72, 73]. The results of Cuoci et al themselves are used to validate other solvers [73]. For the validation case, a droplet of an initial diameter 0.7 mm is placed in a two-dimensional axisymmetric simulation domain (**Figure 5-3**).

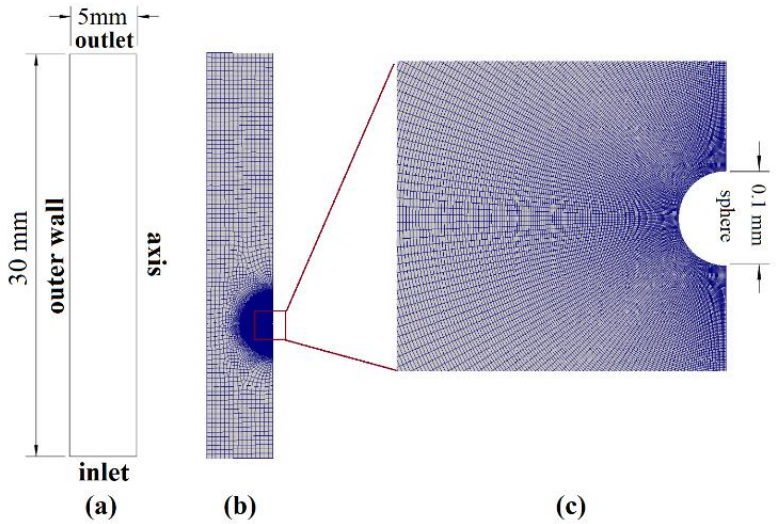

Figure 5-3 (a) Boundary names and dimensions for the validation case (b) corresponding mesh (c) small sphere at the center of drop representing a fiber

The center of the droplet is 10 mm from the inlet boundary. At the center of the droplet, a spherical fiber is introduced to match this case with the one used by Cuoci et al. [99]. The rest of the simulation domain is filled with N_2 and O_2 with a volume fraction of 0.79 and 0.21, respectively. Both the gases and the water droplet are at a temperature of 360 K and pressure of 1 atm. Boundary conditions are similar to the ones given in [73].

As mentioned before, the gas and liquid properties are directly calculated from the OpenSMOKE++ and OpenFOAM libraries respectively.

5.3.2 Results

Figure 5-4 shows the numerical results of the validation case compared with the 1D model. The dimensionless squared diameter against scaled time closely follows the 1D result, except for the initial transient period during which the squared diameter decreases linearly with time following the D^2 law. The temperature plot of **Figure 5-4** (b) also reveals an excellent match with the 1D model. The temperature of the liquid interface dropped during the evaporation process and reached the wet-bulb temperature and became steady.

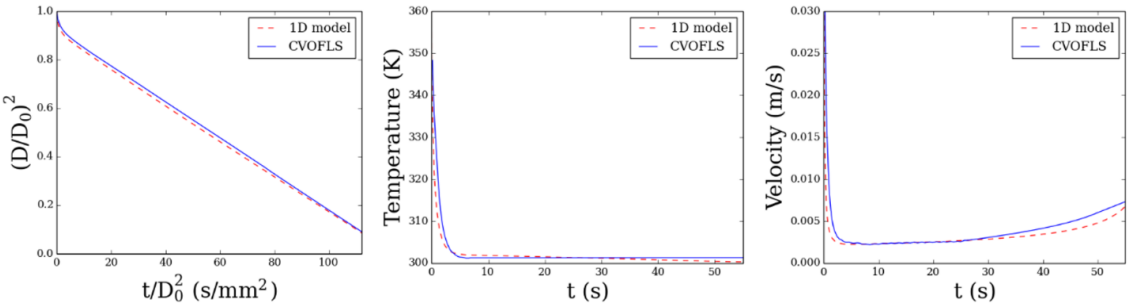

Figure 5-4 Numerical comparison of the 1D model of Cuoci et al. and CVOFLS

This is the expected outcome because during evaporation an equilibrium is reached between the incoming heat flux at the vapor-liquid interface and the enthalpy of vaporization. The fast temperature drop in the transient period is because of the initial condition (isothermal at 360 ºC). **Figure 5-4** (c) shows the vaporization velocity or the convective velocity of the gas leaving the liquid interface against time. Slight discrepancies in velocities and temperatures are observed towards the end of evaporation. This is due to the small sphere present inside the droplet. As argued by [73], the mass of

the spherical liquid droplet is lower than the 1D droplet with the same initial diameter. This gives rise to a higher equilibrium temperature and greater vaporization velocity than the 1D case as the droplet diameter approaches that of fiber. This will not be a problem when modeling evaporation for sessile droplets that do not contain fiber.

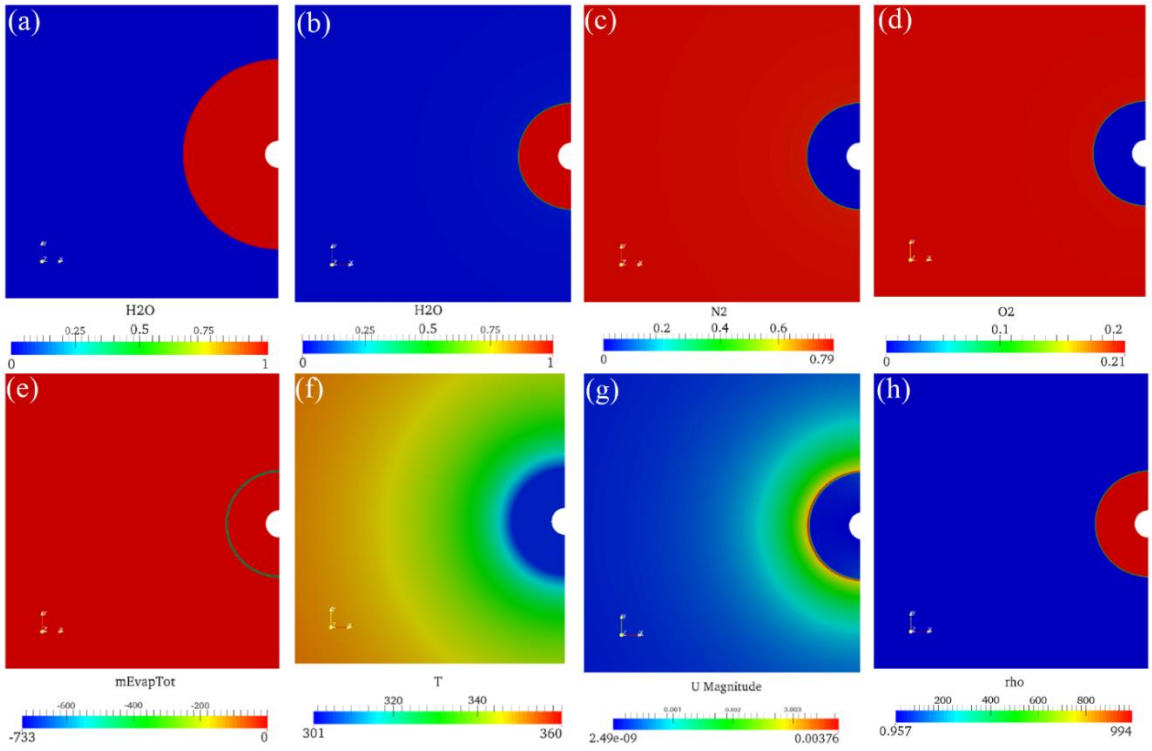

Figure 5-5 (a) H_2O volume fraction at t = 0 sec (b) t = 55 sec. Also at t = 55 sec (c) N_2 (d) O_2 (e) $\dot{m}$ (f) T (g) U and (h) ρ.

Figure 5-5 shows the distribution of species and thermodynamics parameters at time = 55 sec. It also shows the initial volume fraction of H_2O. The H_2O decreases due to evaporation whereas N_2 and O_2 remain as inert species.

The temperature and velocity fields show the expected variation in the radial direction. The $\dot{m}$ shown in **Figure 5-5** (e) reveals that phase change was occurring only around a small region around the interface.

5.3.3 Interface sharpening and spurious current reduction in CVOFLS

Two-dimensional rising bubble: To test the improvement of the CVOFLS solver over the VOF solver, a two-dimensional free rising bubble case presented by Hysing *et al.* [100] is considered. This test case was also validated by Klostermann *et al.* [101] using the open-source VOF finite volume solver in OpenFOAM. The numerical domain of the test case is a rectangle (2 m × 1 m) with top and bottom no-slip walls and side slip walls (show in **Figure 5-6**). The bubble diameter is 0.5 m and the initial center of mass of the bubble is at (0.5, 0.5). The gravitational acceleration acts in the opposite direction to the *y*-axis. This test case does not involve particles.

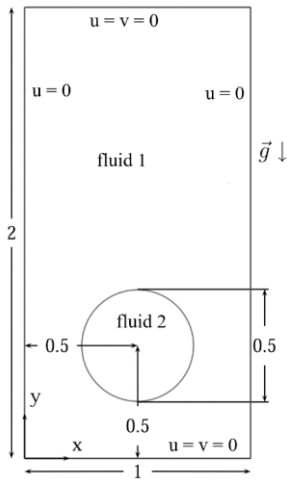

Table 5-1 Physical properties and dimensionless numbers for 2D rising bubbles

Properties (unit)	ρ_1 (kg/m^3)	ρ_2 (kg/m^3)	μ_1 (Pa s)	μ_2 (Pa s)	g (kg m/s^2)
Values	1000	1	10	0.1	0.98
Properties (unit)	σ (N/m)	***Re***	***Eo***	ρ_1/ρ_2	μ_1/μ_2
Values	1.96	35	125	1000	100

Figure 5-6 Initial configuration of the rising bubble case

The physical properties for the case are given in **Table 5-1**. First, the gravity is set to zero and the case is simulated up to 3 s which is the benchmark time for the rising bubble case. Without gravity, the bubble remains still theoretically but in practice, spurious or parasitic currents develop around the bubble. To study the effect of numerical methods used on the generation of parasitic current four cases are considered: two with only VOF based solver and two with the developed CVOFLS solver.

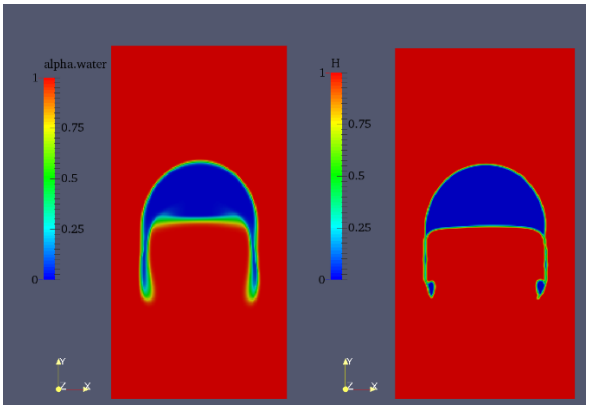

Figure 5-7 Bubble shape at t = 3 s for VOF (left) and CVOFLS (right) case

Table 5-2 Effect of the numerical model on the spurious current in the static bubble at 3s.

Numerical methods	**Grid size, 1/h**	**$\|up_{max}\|$ (m/s)**	**$\|up_{avg}\|$ (m/s)**
VOF	160	2.075e-2	1.946e-4
VOF	320	3.910e-3	1.884e-4
CVOFLS	160	2.697e-3	9.151e-5
CVOFLS	320	1.120e-3	1.167e-4

The maximum and average spurious currents at 3s are recorded in **Table 5-2** for the four cases. The table shows that the CVOFLS cases maintained low values for maximum and average parasitic currents for both grid sizes. On top of that, **Figure 5-7** shows that the interface is much sharper for the COVFLS case and captured the rising bubble deformation better than the VOF case.

5.4 Particle deposition study with CVOFLS-DPD

Finally, the deposition of nanoparticles inside a sessile liquid droplet of an initial diameter 50 µm is studied using the CVOFLS-DPD method. The particle properties for the study are given in **Table 5-3**. A repulsive potential is used to uniformly distribute the particles within the droplet. The size of the CFD domain is 400 µm × 400 µm × 200 µm. and is filled with air at 646 K. The initial temperature of the droplet is 373.15 K. The temperature of the substrate is also maintained at 373.15 K. Gravity is ignored in this

case. The time step for the DEM case is 1×10^{-9} s whereas the time step for the CFD case is 1×10^{-7} s. A smaller time step for DEM is applied to prevent any unrealistic overlap between particles during collisions. **Figure 5-8** shows the initial configuration of the fluids and particles. The rest of this paper is dedicated to the results and discussions of this system.

Table 5-3 Particle properties for DPD

Parameters	Values	Parameters	Values
Particle concentration	0.5 vol%	Hamaker constant, Ha	1.2×10^{-20} J
Particle radius, d	500×10^{-9} m	Relative permittivity, $\in_0$	80
Particle density, ρ_s	1.05×10^{3} kg/m^3	Debye Screening Length, 1/ κ	5 nm

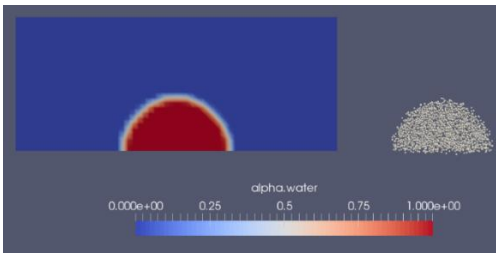

Figure 5-8 Fluid and particle configuration at time t = 0 s

5.4.1 RESULTS AND DISCUSSIONS

Figure 5-9 shows the evaporation stages of the initial water droplet without the particles. The corresponding distributions of the particles that get deposited over time are shown in **Figure 5-10**. The results are shown for three different contact angles, 60º, 90º, and 120º. The results show the distribution of the water phase fraction inside the simulation domain. **Figure 5-9** (a)s show the initial droplet sizes, (b)s show the droplets midway between drying, and (c)s show the droplets just before drying out. The liquid water can be seen to remain pinned during the entire evaporation process. The pinned condition and evaporation create a strong radially outward flow that propels the particles toward the droplet periphery. The nanoparticles inside the droplets are shown in **Figure**

5-10. None of the particles are seen to leave the droplet during the entire evaporation process. As the droplet dries up, the height and the contact angle reduce to keep the pinned radius constant which pushes the particles downward. The nanoparticle motion near the substrate is also affected by the substrate properties like adhesion and friction. Nevertheless, a ring of particles is formed during the evaporation process for all three contact angles. Later in this section, the effects of the substrate on the particle deposition are discussed. The ring width is found to be dependent on the contact angle, the thickest ring is formed with 120º and the thinnest with 60º. This conforms to the work of [11] who reported that the radial flow velocity can be scaled linearly with the evaporation flux which is smaller at the edge for a larger contact angle. Since the contact line is pinned during the entire evaporation process in this study, a ring-like deposit is still observed. This is a little different from Nguyen et al. [102] who reported an inner coffee ring deposit for a large contact angle. For their case, the contact line was initially de-pinned then pinned at a later stage of evaporation which gave rise to the inner ring deposit. However, the contact line can be pinned at a large contact angle with high surface friction as reported in [103]. They did not report any effect of initial contact angle on rim width. Hence this study gives an insight into the effect of initial contact angle with rim width. The deposition times of the particles for the three contact angles are shown in **Figure 5-11** (a). Deposition time depends on the contact angle as expected but the deposition rate has a similar pattern for all three angles. The rate increases after some time because of an increased evaporation rate due to a decrease in contact angle. This speed-up is also seen in the experimental work of [104]. However, as Marin et al. [105] reported, the system condition dictates how pronounced is the rush-hour stage of deposition. In this study, the

charged particles exert a repulsive push to the incoming deposit which actually slows down the deposition rate near the very end of the deposition time.

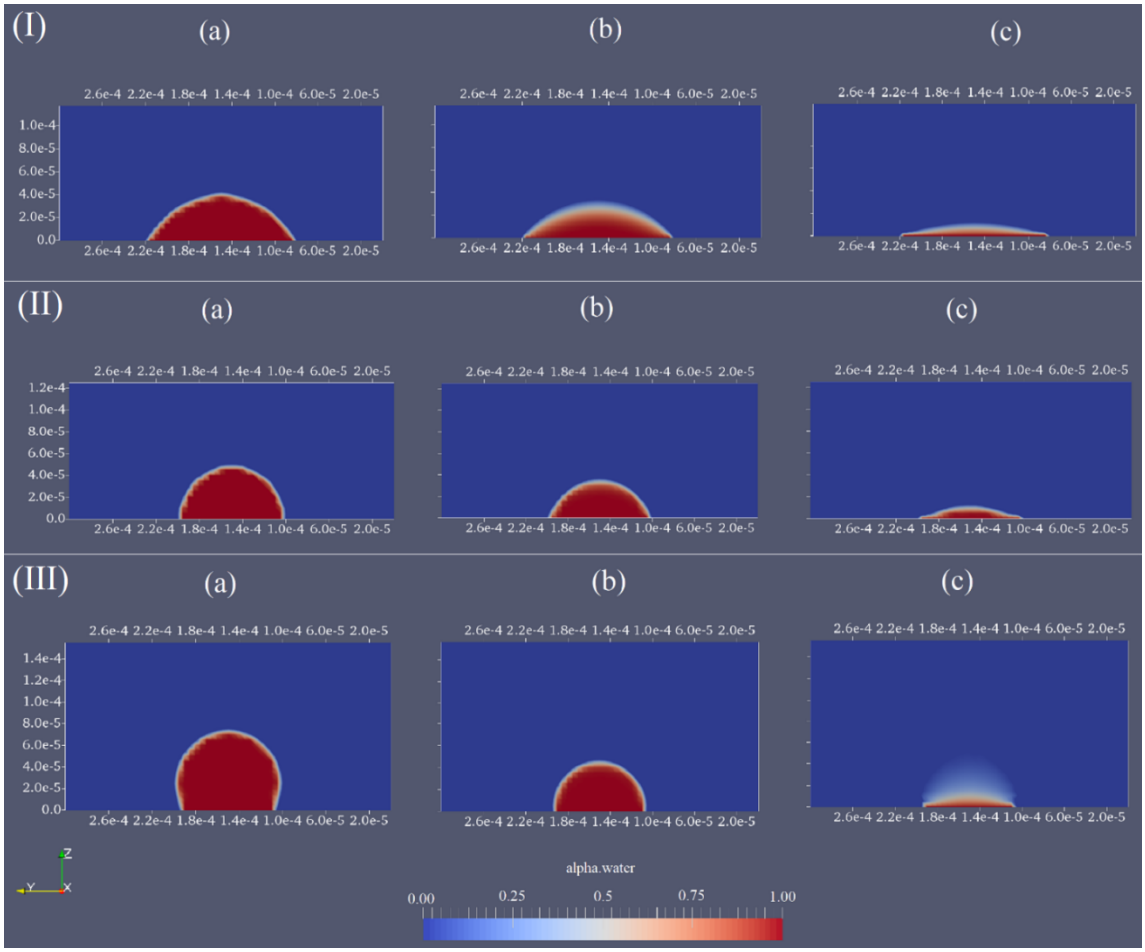

Figure 5-9 Phase fraction of water for (I) 60^0, (II) 90^0 and (III) 120^0 for (a) start (b) mid and (c) just before final dry out, respectively

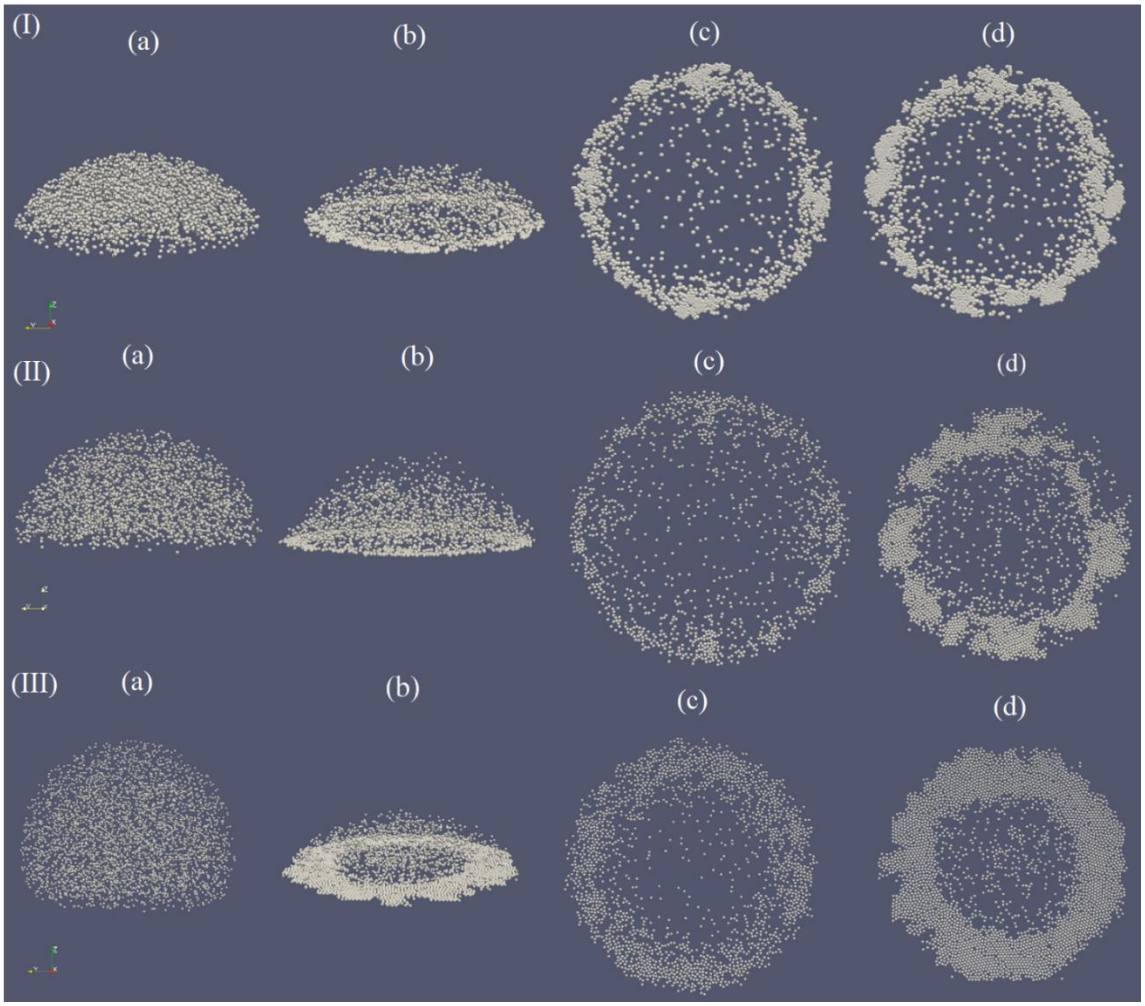

Figure 5-10 Side and bottom deposited view of particles for (I) 60^0, (II) 90^0 and (III) 120^0 for (a) start (b), (c) mid and (d) final deposits, respectively

5.4.1.1 Effect of vdW force

In order to understand the effect of vdW force, two sets of simulation cases are run, one with the vdW force turned on and the other turned off. In both these cases, the friction coefficient is set to a very low value. The deposition time plot and the deposited particle densities are shown in **Figure 5-11** (b) and (c) for contact angle 90º. The results for other angles are similar. The final deposition patterns are shown in **Figure 5-12** (a) and (c) which are also the two cases for low friction. As can be seen from **Figure 5-11** (b) the

vdW force speeds up the deposition process. The initial deposition rates are similar for both cases but then the rate increases rapidly for the vdW as opposed to non-vdW case.

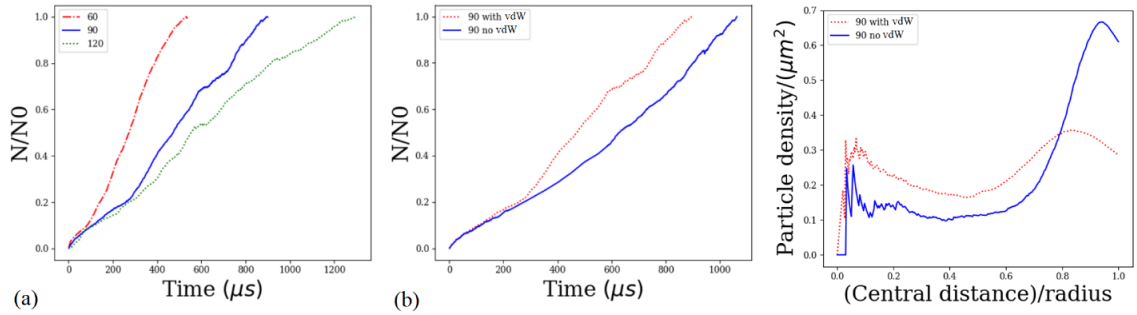

Figure 5-11 Normalized particle deposits-time plot for (a) all contact angles with VDW and (b) 90^0 only. (c) Particle number density/μm^2 against radial distance plot for 90^0

The vdW force also plays a role in the deposition pattern. As can be seen from **Figure 5-11** (c) with the vdW force the number densities of the particles at the edge are lower than the non-vdW case. A ring is still formed but the ring is thicker or wider than the non-vdW case. There is also a peak at the center of the ring indicating some central deposit. These findings are in line with experimental and numerical observations of Bhardwaj et al. [106] who reported that higher vdW attraction favors uniform deposit. In this study, the vdW force on the particles by the surface is not high enough to create a uniform deposit but high enough to speed up the deposition process and cause a thicker ring formation. Later on, it will be shown how uniform deposit can be achieved even with this moderate vdW force.

5.4.1.2 Effect of Friction

To study the effect of friction, two cases were run without the vdW, one with high surface friction and the other low with friction. The results of the final deposition are shown in **Figure 5-12** (a) and (b), and the particle densities are shown in **Figure 5-13**. The low friction with non-vdW case is similar to the one discussed in the previous

section. The deposited particles form a pronounced ring with higher edge density than the vdW case. On the other hand, a thicker ring is seen with the high friction case without vdW. With high friction, the particles cannot slide freely across the surface, hence more particles are seen deposited away from the edge. Finally, the vdW force is turned on along with the high friction force. The result is shown in **Figure 5-12** (d) which shows that the deposition pattern is even more uniform than the low friction case with vdW. For comparison, the number density of the final deposit is shown in **Figure 5-13**. The number density plot indicates a slightly high center and edge deposit and almost uniform deposit in between.

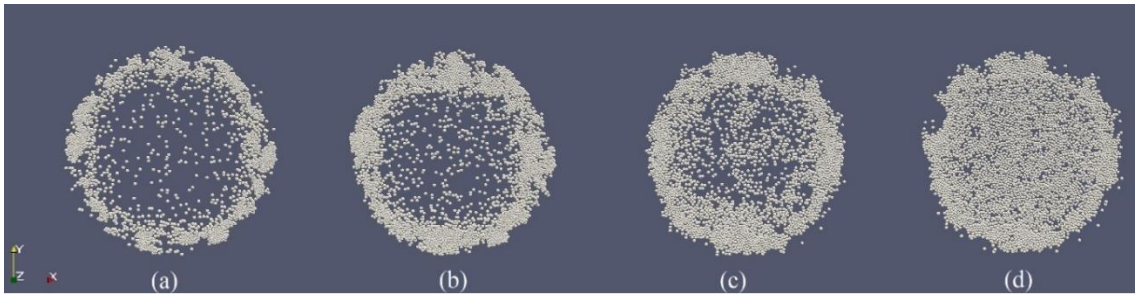

Figure 5-12 Bottom deposited view of particles for 60^0 case with (a) low friction no VDW (b) high friction no VDW, (c) low friction with VDW and (d) high friction with VDW, respectively.

This allows one to conclude that high friction and vdW are needed for a uniform deposit whereas the opposite, i.e., low friction and low vdW favors a ring-like deposit.

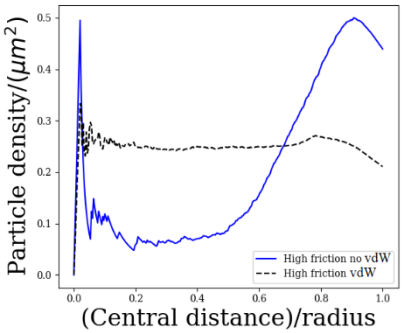

Figure 5-13 Particle number density/μm^2 - radial distance plot for high friction

cases

5.4.1.3 Local Particle Arrangement

In addition to the overall ring-like or uniform deposit, the self-assembly of the particles can also be characterized by their local arrangements or packing. For assessing the morphology of deposits as in this work, the standard procedures involve using the radial density profile and the normalized grayscale intensity profile [107, 108]. However as pointed out by [109], both of these quantities have limitations when it comes to characterizing and differentiating particle distributions. For example, a peak in the radial density profile can be correlated to a small cluster of particle aggregates or a larger aggregate, while the line profiles give information on the distribution of particles on a narrow segment. Hence it is important to implement statistical parameters that can characterize and differentiate deposits.

In this paper, the first-order statistics (FOS) has been used to fully capture the complex texture of deposit patterns. First of all, the entire system is decomposed into Voronoi cells with the radical Voronoi tessellation method. The Voronoi tessellation is done using the "pyvoro" software developed by Joe Jordan. The software is a python extension of "voro++" code developed by Chris Rycroft [62].

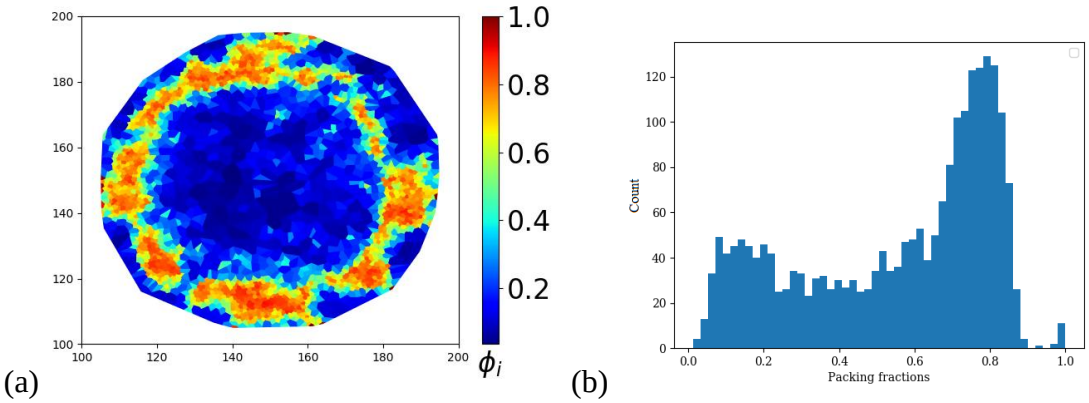

Figure 5-14 (a) Local packing fraction field and (b) corresponding histogram

The Voronoi tessellation is shown in Figure 14 (a). The local packing fraction is then calculated by:

$$\phi_i = \frac{V_i}{V_c} \tag{5.50}$$

where ϕ_i is the packing fraction around each particle *i*, V_i is the area of particle *i*, and V_c is the area of the Voronoi cell around particle *i*. The local packing fraction field is shown in **Figure 5-14** (a) where the intensity of the color in each cell varies according to the relative packing density. From the packing fraction field, one can immediately recognize regions of the high and low local concentration of particle deposits. The histogram of the local packing fraction for the final deposit for the 90^0 contact angle with low friction and no vdW force is shown in **Figure 5-14** (b). The histogram has a bimodal type distribution with the highest peak near the higher packing fraction along with a short peak on the low side. However, the spread of the peak suggests that the particles are quite dispersed at areas other than the edge.

In order to apply FOS, five different statistic measures are calculated depending on the time-dependent histogram of the local packing fraction: mean, standard deviation, integrated density, skewness, and kurtosis. The definitions for these measures are given below:

$$\text{Mean, } \mu_1 = \sum_{i=1}^{nbins} \frac{\text{bin\_middle}(i) \times \text{Count}(i)}{\sum \text{Count}} \tag{5.51}$$

$$\text{Standard deviation, } \tilde{\sigma} = \sqrt{\sum_{i=1}^{nbins} \frac{\left(\text{bin\_middle}(i) - \mu_1\right)^2 \times \text{Count}(i)}{\sum \text{Count}}} \tag{5.52}$$

$$\text{Integrated density, } I = \mu_1 \times \sum \text{Count} \tag{5.53}$$

$$\text{Skewness, } \mu_3 = \sum_{i=1}^{nbins} \frac{\left(\text{bin\_middle}(i) - \mu_1\right)^3 \times \text{Count}(i)}{\tilde{\sigma}^3 \times \sum \text{Count}} \tag{5.54}$$

$$\text{Kurtosis, } \mu_4 = \sum_{i=1}^{nbins} \frac{\left(\text{bin\_middle}(i) - \mu_1\right)^4 \times \text{Count}(i)}{\tilde{\sigma}^4 \times \sum \text{Count}} - 3 \tag{5.55}$$

where $\text{bin\_middle}(i)$ and $\text{Count}(i)$ are the middle of the *i*th bin of the histogram and its count or frequency respectively, and *nbins* is the total number of bins for the histogram. The mean and the standard deviation are measures of the average packing fraction and variation around the average respectively. The integrated density is a measure of the total number of deposits with an overall mean packing fraction. The skewness and the kurtosis are measures of the asymmetry and flatness of the histogram, respectively.

The FOS texture parameters extracted from the deposits formed at different time steps are plotted in **Figure 5-15**. The mean, standard deviation, and integrated density parameters grow due to deposited particles increasing the local packing fraction at the droplet edges. On the contrary, the Skewness and Kurtosis decrease because the packing fraction distribution of the histograms shifts from an initial sharply peaked low value to a more symmetric bimodal distribution at a higher time step.

From the results of the plot in **Figure 5-15** three different stages of deposit development are identified for all three contact angles. The first stage represents the initial stage of particle deposition where the mean, standard deviation, and integrity density increase slowly. The skewness and kurtosis show fluctuations at high values representing irregular deposition of particles. The normalized time plot indicates that this stage lasts about one-quarter of the deposition time. The second stage represents a fast deposit growing stage where the mean, standard deviation, and integrated density

continue to increase as the local packing fraction increases. Most of the particles are deposited at this stage that lasts for about another one-half time. At the last and final stage, the curves for the first three measures start to flatten out. One can see some increased differences among the curves which can be attributed to the final stage of the evaporation process when there are increased collisions among particles. The skewness and kurtosis continue to drop to low values as the packing fraction histogram becomes more bimodal in distribution.

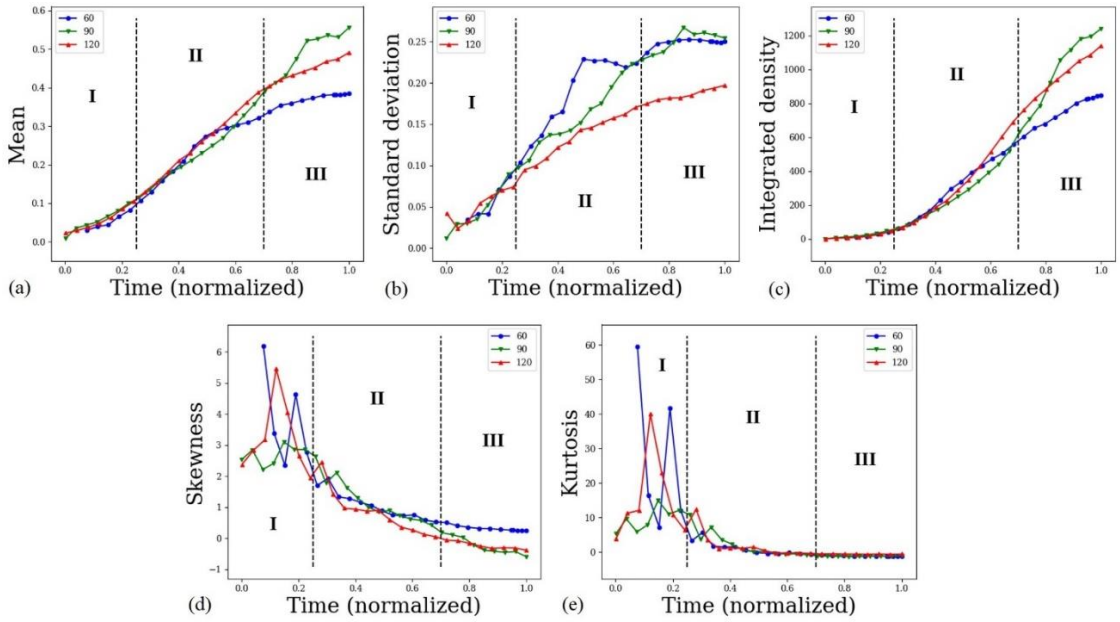

Figure 5-15 The (a) mean, (b) standard deviation, (c) integrated density, (d) skewness, and (e) kurtosis against time plots for all contact angles

5.5 Conclusion

A numerical investigation on evaporation induced self-assembly of nanoparticles is carried out using a coupled CVOFLS-DPD approach. The interaction between fluid and particle is taken into account by the hydrodynamic force, interface force, and drag force. The evaporation model of the liquid is validated against the analytical result. The

numerical method is then used to study particle deposition of an evaporating droplet. The results showed that the nanoparticles are self-assembled themselves at the bottom of the container as the liquid evaporates. Ring formation of particles for different contact angles is shown along with the evaporating liquid. The rim widths of the deposited particle rings are seen to increase with contact angles not reported in the study of [102] or [103] who also reported evaporation for large contact angles. The deposition rates of particles increase with time but slow down at the end due to the repulsion by the deposited particles conforming to the work of [104] and [105]. The effect of substrate vdW force is discussed. The vdW force speeds up the deposition process after an initial time delay. The vdW force also causes a thicker ring and lower particle density at the edge. Some central deposits are also observed with the vdW case. These observations are in-line with the experimental work of [106]. The effect of friction is then discussed. Friction impedes particle motion on the surface thereby causing thicker ring deposits. When both friction and vdW force are present a uniform particle deposit is seen to occur. FOS analysis, applied to characterize local microstructure, reveals three stages of deposit development. The first stage is the irregular deposition stage which takes one-quarter of the deposition time. The second stage is the fast-growing stage lasting for another one-half time. At the third or final stage, most particles are settled down and the stage lasts until dry up.

6 MACHINE LEARNED SUB-GRID SCALE MODELING FOR OXIDATION OF TOLUENE IN A BUBBLE COLUMN REACTOR

6.1 Introduction

Bubble or slurry column reactors have widespread industrial applications including but not limited to liquid-phase oxidation, hydrogenation, hydroformylation, carbonylation and chlorination [110-112]. Lots of recent studies have been devoted to the design of reactors, scaling up and find effective flow and mass transfer correlations for the reactors. For reactors involving fast gas-liquid reactions it has been shown that the microscale fluid dynamics and mass transfer near single bubble supersede the bubble-bubble interactions present in the reactor in terms of conversion, selectivity and yield of the products of reaction [110-113]. This is also true for reactors operating in bubbly flow regime [111-113].

There has been a number of experimental techniques developed for investigating mass transfer across gas-liquid interface of rising bubbles in recent times [114-118]. However, most of these experiments failed to provide detail information about the microscopic phenomena that occur inside the hydrodynamic and concentration boundary layer of bubbles. Numerical analysis, on the other hand, can provide important insight about the microscopic phenomena occurring near the interface.

Most numerical work present in literature can be divided into two categories single-phase simulations using a fixed bubble model [110, 113] and two-phase simulations of deformable bubbles in 2D [119, 120] and 3D [111, 121]. Some investigations into small

group of bubbles in 2D [122, 123] or 3D [124, 125] have also been carried out. Despite the recent interest, numerical analysis of reactive-diffusive-convective bubble system have been greatly hindered by the presence of inherent scale difference in such a system. The next section of this paper provides a brief discussion of the limitations of the traditional numerical schemes in handling the scale differences and presented sub-grid scale modeling as an alternative to avoid such limitations. However, existing sub-grid scale models have their own problems and challenges, and for this reason, this paper presents a machine learned sub-grid scale (ML-SGS) model suitable for reactive-diffusive-convective systems.

In this paper, the developed ML-SGS model is used to study the oxidation of liquid toluene by oxygen bubbles. Depending on system properties like viscosity, density, surface tension and bubble size and velocity, a variety of bubble shapes can exist in a bubble column reactor. As shown by previous researchers, these different bubble shapes can be mapped to a Eo-Re-Mo diagram where Eo is the Eotvos number, Re is the Reynold number and Mo is the Morton number [126-128]. The bubbles used in this work come from carefully done direct numerical simulation (DNS) of bubbles rising with terminal velocity in a quiescent liquid and represent real bubbles as closely as possible. The bubble shapes are obtained from the work of Weiner et al [129, 130]. The system dimensionless parameters are adjusted so that the bubble shapes vary from near spherical to ellipsoidal and dimpled ellipsoidal bubbles as described in literature.

The oxidation of toluene considered in this work have numerous industrial applications. Some of the products of oxidation such as Benzaldehyde (PhCHO), benzyl alcohol ($PhCH_2OH$) and benzoic acid (PhCOOH) are required materials for

pharmaceutical, perfume, flavor and color industries [131-134]. The reaction itself is complicated by radical chain propagation mechanism and require the presence of catalyst. In this paper the oxidation reaction is modeled as a parallel competitive reaction, complicated enough to demonstrate the ability of the ML-SGS model.

6.2 SGS Modeling for Reactive-Diffusive-Convective System: Needs and Challenges

A bubble rising in a bulk liquid is surrounded by a hydrodynamic boundary layer, δ_h which is much smaller than the bubble diameter, d_B for Re >> 1. For example, it has been shown that for a medium sized bubble the average hydrodynamic boundary layer scales with the bubble diameter as $\delta_h / d_B \sim \mathrm{Re}^{-1/2}$ [135-137]. On top of that, if the bubble is composed of a gas that diffuses and reacts with the bulk liquid, a concentration boundary layer is developed that is embedded within the hydrodynamic boundary layer. For Peclet number, Pe > 1, and Schmidt number, Sc > 1, it has been shown that the concentration boundary layer scales with the hydrodynamic boundary layer as $\delta_c \sim \delta_h \times \mathrm{Sc}^{-1/2}$ [135, 136]. For Sc $\geq$ 100 the numerical mesh for species transfer needs to be roughly 10-20 times smaller than the mesh for resolving hydrodynamic boundary layer. In order to overcome the problem of requiring extremely fine mesh, the direct numerical simulation of convective flow is usually combined with the SGS model for mass transfer. However, the SGS models have their own limitation. For a typical Finite Volume discretization used in many computational fluid dynamics (CFD) software, the concentration fields are defined and stored for each cell center. At each time step, the cell centered values are updated based on the source terms and the inflow and outflow fluxes

at each cell faces. However, calculating the fluxes require the field values and gradients at the cell faces. For a highly non-linear concentration profile, typical interpolation scheme like linear reconstruction leads to significant error in predicting species concentration and mass transfer. This has been illustrated in **Figure 6-1** (a) where c_Σ is the interface concentration which drops over two cell spaces away from the interface. The red line is the face gradient approximated with the cell centered values.

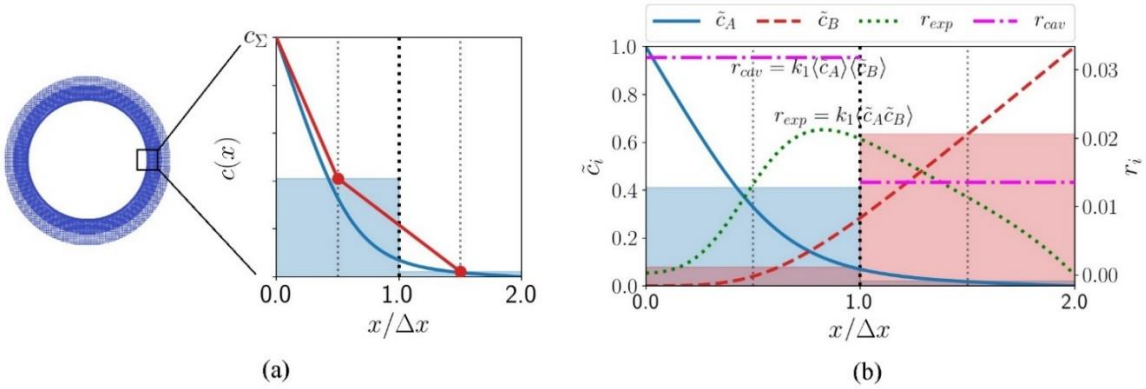

Figure 6-1 (a) Effect of low mesh resolution on approximating (a) face flux (b) reaction source term. The blue and red shaded area depicts the cell averaged concentration of A and B respectively. The pink lines denote the product of the cell-centered averages and green line denotes the average of the product. Redrawn from [129].

Another problem with insufficient mesh resolution associated with reactive system is the inaccurate computation of reaction source terms. This has been depicted in the **Figure 6-1** (b) where $\tilde{c}_A$ and $\tilde{c}_B$ are normalized concentrations of two reactants undergoing a reaction similar to the first order reaction with two reactants. When cell-centered values are used to compute the source term it results in a much higher value in the first cell than that computed with the exact profiles. This is because the product of the cell-averaged

concentrations, $\langle \tilde{c}_A \rangle \langle \tilde{c}_B \rangle$ is not necessarily the same as the average of the product, $\langle \tilde{c}_A \tilde{c}_B \rangle$.

There have been several attempts to improve the concentration profile at the boundary layer. Most of these attempts rely on the analytical solution of a simplified boundary layer problem [119, 125, 136, 138]. For example, [136] used an error function to approximate the concentration profile of a species undergoing physisorption.

$$\tilde{c}_{A,\text{model}} = 1 - \text{erf}\left(\frac{x}{\delta}\right) \tag{6.1}$$

where x is the distance from the interface and δ is an adjustable parameter which needs to be determine iteratively for each interface cells such that the cell-averaged concentration for $\tilde{c}_{A,\text{model}}$ matches the cell-centered concentration. However, for reactive-diffusive-convective system involving multiple species undergoing consecutive or parallel competitive reactions like the one discussed in this paper it becomes practically impossible to obtain simple analytical solution to predict the concentration profile [139]. In this paper, it will be shown how ML models can efficiently and accurately replace analytical and iterative solutions required for SGS modeling of convective-reactive-diffusive system such as oxidation of toluene in a bubble column. Before moving on, the work of Weiner et al has to be mentioned [140]. Weiner et al used a data driven SGS model to substitute the analytical profile. However, their work is limited to a first order decay reaction with only one species. They used a fixed bubble shape and focused on changing the flow variables only. In this study, a more complex scenario of parallel competitive reactions with multiple species is considered along with different bubble

shapes. However, the tutorial and codes and the doctoral dissertation of Weiner et al [129, 130] have been a great help for this work.

6.3 Data Generation

To generate the data required to train the ML model, a spherical oxygen bubble rising in liquid toluene is considered. **Figure 6-2** shows the initial and boundary conditions for the bubble. The simulation domain is 2D axisymmetric.

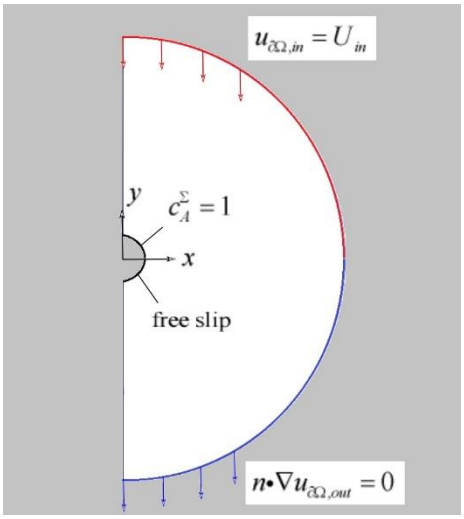

Figure 6-2 Initial and boundary conditions for the simulation for data generation.

The following dimensionless equations are solved to obtain the hydrodynamic flow field.

$$\frac{\partial \tilde{\rho}}{\partial \tilde{t}} + \tilde{\nabla} \bullet \left(\tilde{\rho} \tilde{\mathbf{u}} \right) = 0 \tag{6.2}$$

$$\frac{\partial \tilde{\rho} \tilde{\mathbf{u}}}{\partial \tilde{t}} + \tilde{\nabla} \bullet \left(\tilde{\rho} \tilde{\mathbf{u}} \otimes \tilde{\mathbf{u}} \right) = -\tilde{\nabla} \tilde{p} + \frac{1}{\mathrm{Re}} \tilde{\nabla} \bullet \left(\tilde{\nabla} \tilde{\mathbf{u}} + \tilde{\nabla} \tilde{\mathbf{u}}^{T} \right) + \frac{1}{Fr} \tilde{\rho} \tilde{\mathbf{g}} \tag{6.3}$$

The following dimensionless quantities are utilized in the above equations. The Eo and Mo numbers discussed in the introduction are also defined here,

$$\tilde{t} = \frac{t}{d_B / U_{in}}, \tilde{\mathbf{x}} = \frac{\mathbf{x}}{d_B}, \tilde{\mathbf{u}} = \frac{\mathbf{u}}{U_{in}}, \tilde{p} = \frac{p}{\rho_L U_{in}^2}, \tilde{\mathbf{g}} = \frac{\mathbf{g}}{g}, \tilde{\rho} = \frac{\rho}{\rho_L}, \tilde{\sigma} = \frac{\sigma}{\sigma_L},$$
$$\mathrm{Re} = \frac{\rho_L U_{in} d_B}{\mu_L}, \mathrm{Fr} = \frac{U_{in}^2}{g d_B}, \mathrm{Eo} = \frac{g \rho_L d_B^2}{\sigma_L}, \mathrm{Mo} = \frac{g \mu_L^4}{\rho_L \sigma_L^3} \tag{6.4}$$

Once the flow field is obtained, the species mass balance equation for each species is solved. The non-dimensional species transport equation reads,

$$\frac{\partial \tilde{c}_k}{\partial \tilde{t}} + \tilde{\nabla} \bullet \left(\tilde{c}_k \tilde{\mathbf{u}} \right) = \frac{1}{\mathrm{Pe}} \tilde{D}_k \tilde{\nabla}^2 \tilde{c}_k + \sum_{i=1,2} \nu_{k,i} \tilde{r}_i \tag{6.5}$$

where,

$$\tilde{c}_k = \frac{c_k}{c_{A|\Sigma}}, \tilde{D}_k = \frac{D_k}{D_A}, \tilde{r}_1 = Da_1 \tilde{c}_A \tilde{c}_B, \tilde{r}_2 = Da_2 \tilde{c}_P \tilde{c}_B \tag{6.6}$$

The dimensionless numbers are,

$$\mathrm{Pe} = \frac{U_{in} d_B}{D_A} = \mathrm{Re}\,\mathrm{Sc}, Da_1 = \frac{d_B k_1 c_{A|\Sigma}}{U_{in}}, Da_2 = \frac{d_B k_2 c_{A|\Sigma}}{U_{in}} \tag{6.7}$$

The subscript k in equations 4 and 5 are for each species, where Σ and l used in **Table 6-1** indicate interface and bulk.

Table 6-1 Values of properties and dimensionless numbers used in simulation.

Physical properties	Values	Physical properties	Values
Gas density, ρ_G	8.34 kg/m^3	Concentration, $\tilde{c}_{A\|\Sigma}$	1
Liquid density, ρ_L	742.58 kg/m^3	Concentration, $\tilde{c}_{B\|l}$	1
Liquid viscosity, μ_L	0.0001747 PaS	Sc_A	100
Surface tension, σ_L	0.0145 Nm	$Sc_{B,P,S}$	50
System pressure, P	1 atm	Re	100

System temperature, T	145 ^{0}C		

The next section discusses the kinetics for the oxidation of toluene and the way to obtain the reaction rate constants, k_1 and k_2. Meanwhile, **Table 6-1** shows the parameters used for data generation. The thermodynamic properties are obtained from the DIPPR database [141]. The simulation was run for $\tilde{t}$ = 1, and the concentration fields were saved every $\Delta\tilde{t}$ = 0.005.

6.4 Kinetics of the Liquid-Phase Oxidation of Toluene

The mechanism of toluene oxidation is a complicated, multistage, free-radical chain reaction with chain inhibition, propagation and chain termination steps [131-134]. The oxidation is further complicated by the requirement of specific catalysts like cobalt catalyst in acetic acid or toluene or a bromide catalyst in a non-polar solvent [133, 134]. A reaction scheme with all elementary reactions is too complicated to be of practical use. Hence, a number of simplified kinetic schemes are proposed in the literature [133, 134, 142]. In many of these schemes the Benzaldehyde (PhCHO) and Bezyl alcohol ($PhCH_2OH$) are considered as reaction intermediates and Benzoic acid (PhCOOH) and other over-oxidized compounds as final products. In this study the oxidation of toluene is modeled as a parallel competitive reaction [133, 143],

$$\begin{aligned} A + B &\xrightarrow{r_1} P \\ A + P &\xrightarrow{r_2} S \end{aligned} \tag{6.8}$$

where A denotes the dissolved oxygen, B the liquid toluene, P the desired products (Benzaldehyde and Bezyl alcohol), and S denotes the Benzoic acid and other over-oxidized final products. Rates of these reactions are given by,

$$r_1 = k_1 c_A c_B = k_{12} c_A c_B$$
$$r_2 = k_2 c_A c_P = (k_3 + k_3) c_A c_P \quad (6.9)$$

where the kinetic parameters are obtained from Hoorn et al [133] and reported in **Table 6-2**.

Table 6-2 Reaction rate constants.

Rate constants	Values
k_{12}	0.015 m^3/mol/sec
k_3	1.35 m^3/mol/sec
k_4	3.90 m^3/mol/sec

6.5 Model Creation

First, the massive amount of raw data generated from the simulation (>50 GB) is reduced to include only a narrow band (0.1 d_B) around the bubble interface important for boundary layer profile. It should be noted that the mesh around the bubble is such that all the cells are normal to the interface to reduce interpolation error. Later on, it will be shown how mesh resolution is set and convergence is studied in the Validation section of the paper. The features and labels used to create the ML models are given in **Table 6-3**.

Even though no feature extraction method is used in this work, the features used are chosen carefully based on the previous analytical work. In equation 1 it has been shown that the boundary profile was approximated as an error function. The free parameter in the error function was corrected based on the average concentration as,

$$\tilde{c}_A = \frac{1}{l}\int_0^l \tilde{c}_{A,\text{model}} dx \quad (6.10)$$

So, it can be seen that both the distance from the interface and the average concentration are required to estimate the boundary profile. The idea of using the average

concentration in cells to find the actual concentration can be deemed analogous to sharpening of a blurred image, a problem which ML models have proven to be highly effective against. It is worth noting that the normal derivative at the interface is considered separately form the normal derivative at the bulk. Using two models instead of one improves the accuracy of the predictions.

Table 6-3 Local parameters for ML; the last five rows are the labels.

Parameter	Definition
Distance from interface	$l = \left\|\mathbf{x}_l - \mathbf{x}_\Sigma\right\| / d_B$
Average concentration of reactants and products	$\left\langle \tilde{c}_{A,B,P,S} \right\rangle_l = \frac{1}{l}\int_{n=0}^{l} \tilde{c}_{A,B,P,S} dn$
Concentrations at $\tilde{\mathbf{x}}_l$	$\tilde{c}_{A,B,P,S\|l} = \tilde{c}_{A,B,P,S}\left(\tilde{\mathbf{x}} = \tilde{\mathbf{x}}_l\right)$
Normal derivatives at the interface	$\partial_n \tilde{c}_{A,B,P,S} \mid_\Sigma = \nabla \tilde{c}_{A,B,P,S} \mid_\Sigma$
Normal derivatives at the bulk cell face	$\partial_n \tilde{c}_{A,B,P,S} \mid_l = \nabla \tilde{c}_{A,B,P,S} \mid_l$
Source term for reaction A+B $\rightarrow$ P	$\dot{r}_{AB}$
Source term for reaction A+P $\rightarrow$ S	$\dot{r}_{AP}$

6.6 Training the ML Model and Incorporating the Trained Model in CFD Solver

PyTorch [144] is used to train and create the ML model whereas libTorch, the C++ API for PyTorch, is used to embed the trained models in the OpenFOAM [145] CFD solver. The ML algorithm used in this work is called Multilayer Perceptron (MLP) [146]. Each label has a separate MLP model created for it. The MLPs used to fit the training data all have 4 hidden layers, with 50 neurons per layer, and used a ReLU activation function and ADAM optimizer [144]. Each model was trained for 5000 epochs. In

addition to the data reduction discussed in previous section, the data are also sampled such that they are distributed uniformly over the entire label space. For each MLP, the number of feature-label pairs so created are of the order of 10^6. The data are then split into a training (75 %) and a validation set (25%). The training of all the models took little more than an hour on a standard CPU with 4 cores with all the weights being double precision. Using the mean squared error as the loss function the maximum validation loss is found to be 1.58×10^{-4}.

Figure 6-3 shows the histogram for the relative error for the labels associated with reactant A. As can be seen, most data points have less than 1% percent error and maximum error is less than 8%.

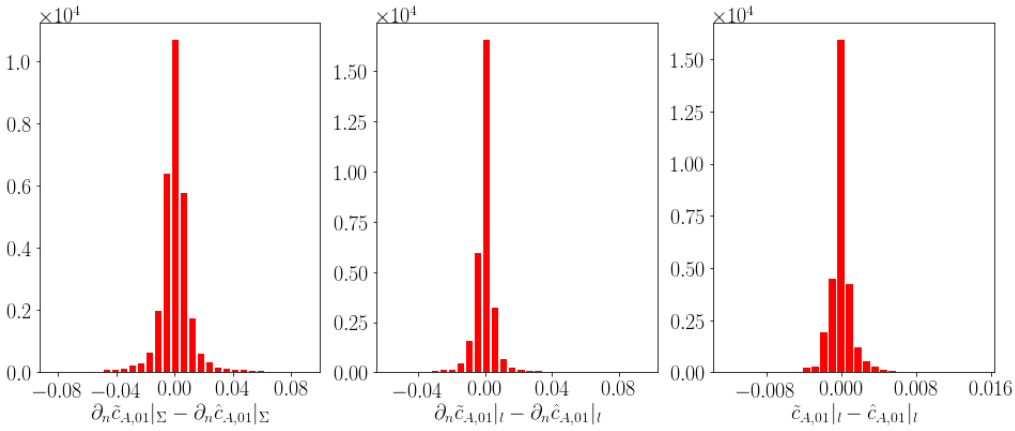

Figure 6-3 Histograms of relative errors for the labels associated with species A.

The distribution of relative error for the labels associated with other species are shown in the **Figure 6-4**. Once again the relative errors are mostly confined to a narrow range (about 1%) around the mean. The maximum relative errors for B is less than 6%, for P is less than 4% and for S is less than 6%. The maximum relative errors for the source terms $\dot{r}_{AB}$ and $\dot{r}_{AP}$ shown in **Figure 6-5** are 0.3% and 1.2% respectively.

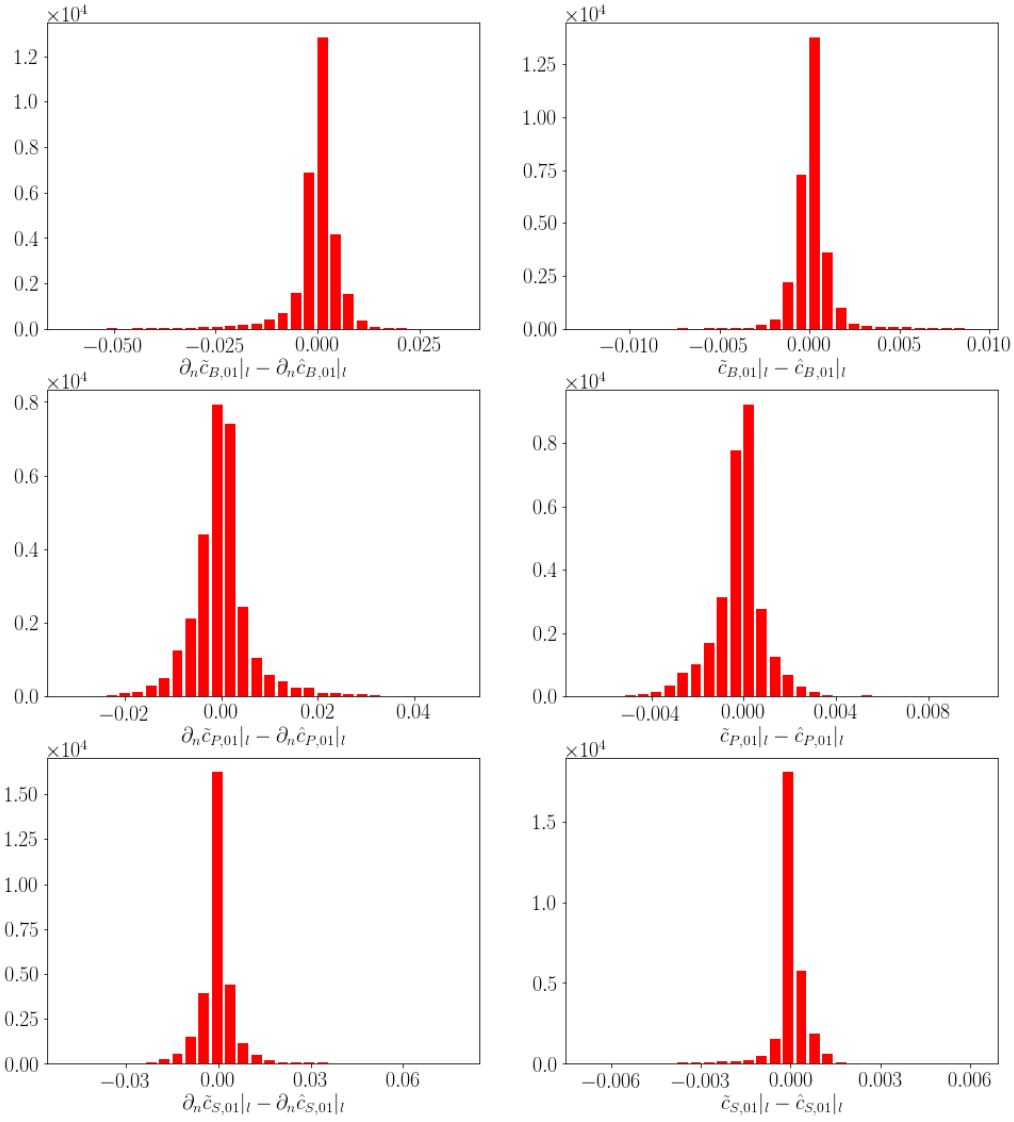

Figure 6-4 Histograms of relative errors for the labels associated with species B,P and S.

Once the trained models are available, they are imported into the OpenFOAM [145] C++ solver ML-SGS, thanks to the PyTorch's C++ API libTorch. The algorithm showed in the **Figure 6-6** is used to incorporate the trained models into the ML-SGS model. The features are extracted and scaled at each time step and feed into the pre-trained models which provides the labeled outputs. The labeled outputs are then scaled and transformed appropriately and feed into the solver pipeline to correct the species mass fluxes.

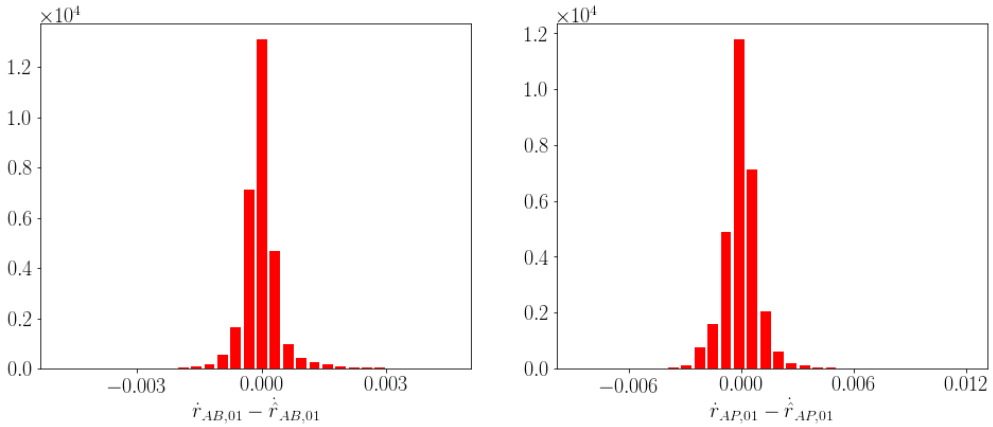

Figure 6-5 Histograms of relative errors for the labels associated with the source terms.

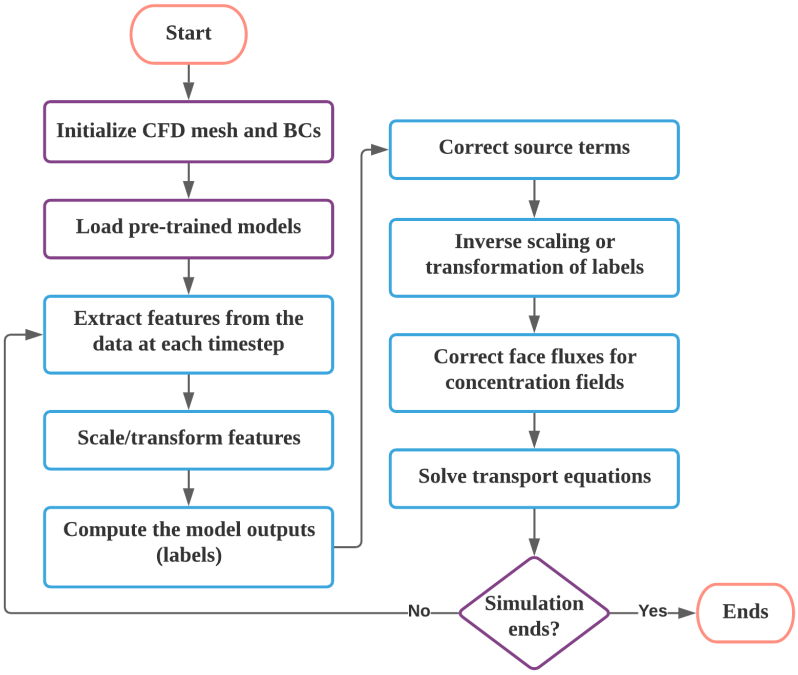

Figure 6-6 Algorithm for incorporating trained ML models into CFD solver.

6.7 Validation

Three different cases are considered for comparing the performance of the ML-SGS approach to the results obtained with solver using standard discretization. The first two cases are run with four different mesh resolution to understand the effect of mesh on the

boundary profile. The last case is run with the finest mesh only. As discussed in the section **6.2**, the concentration boundary layer thickness can be approximated by $\delta_c \sim d_B \mathrm{Pe}^{-1/2}$. Hence, the mesh resolutions are set based on the ratio $d_B \mathrm{Pe}^{-1/2} / \Delta x$ where Δx is the thickness of the first layer adjacent to the interface. From the coarsest to the finest mesh, the values for $d_B \mathrm{Pe}^{-1/2} / \Delta x$ are 0.2, 0.5, 1.4 and 5.8 respectively. They will be named as mesh 0, mesh 1, mesh 2 and mesh 3 respectively from hereby onwards. It can be noted that for mesh 0 and mesh 1 the boundary layer is embedded within the first cell layers. For mesh 2 the boundary layer is barely thick enough and for mesh 3 there are approximately five cell layers within the boundary layer. For data generation a much finer mesh is used, the $d_B \mathrm{Pe}^{-1/2} / \Delta x$ is 10.

Table 6-4 Parameters for the validation cases

Case	Re	Eo	mesh
Case 1	290	0.14	mesh 0, mesh 1, mesh 2, mesh 3
Case 2	660	0.44	mesh 0, mesh 1, mesh 2, mesh 3
Case 3	8.5	243.0	mesh 3

Even though the model is trained for a spherical bubble the validation cases all have shapes different from sphere. In fact, the shapes represent real bubbles for the specified Re, Eo and Mo number. These shapes are obtained by DNS simulation of bubbles rising in a liquid with terminal velocity [129, 130]. Note that the last bubble shape is very different from sphere and usually referred to as dimpled-ellipsoidal in literature. For the last case the dependence on Mo number is not exactly followed because the goal is to investigate the effect of different bubble shapes. Bhaga et al [127] reported to create such

conditions by introducing large bubbles into aqueous sugar solutions. The addition of sugar increases the viscosity of the liquid without significantly changing its density or the surface tension. **Table 6-4** summarizes the three cases along with the relevant parameters. Altogether nine different cases are considered for testing the ML-SGS model.

The comparison between the results of the standard model using linear flux reconstruction and the ML-SGS model for the concentration profile of the species A are given in **Figure 6-7**. The results are produced with the finest mesh, mesh 3. The difference is almost negligible in observation.

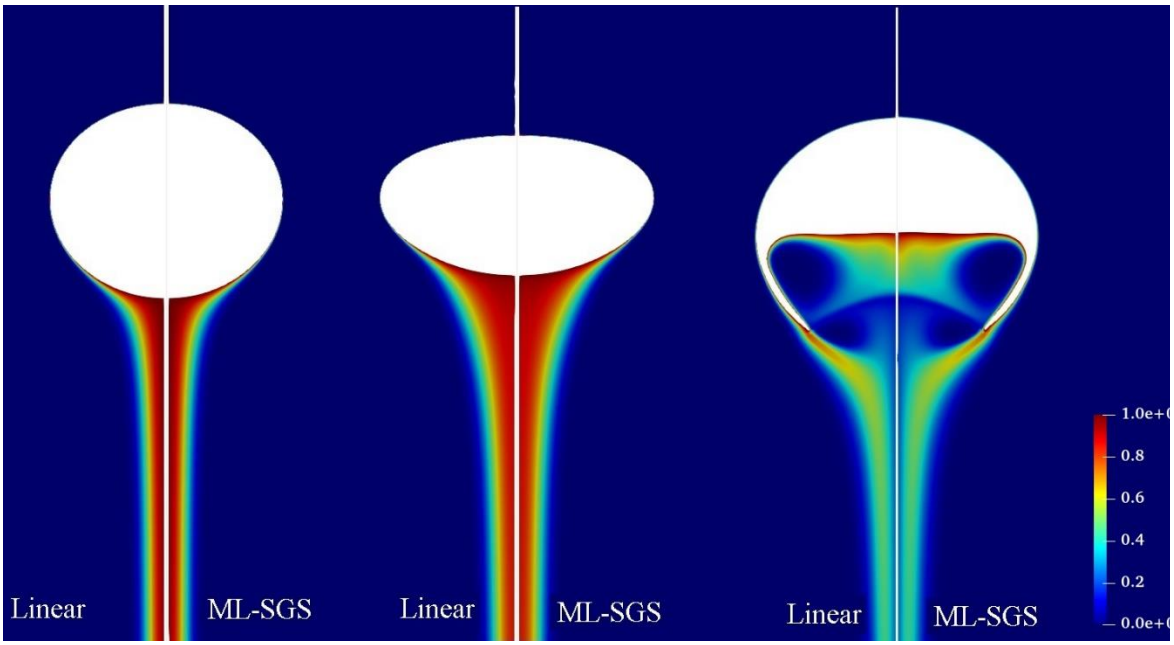

Figure 6-7 Comparison of the concentration profiles of species A for Case 1 (left), Case 2 (middle) and Case 3 (right) for the linear and ML-SGS model. All cases used mesh 3 here.

For reactive-diffusive-convective system, one parameter of interest is the local Sherwood number given by,

$$Sh_{loc} = \frac{\partial_n c_{A|\Sigma} d_B}{c_{A|\Sigma}} \tag{6.11}$$

The local Sherwood number for different polar angles along the bubble for two test cases are shown in **Figure 6-8**. As the plots show, the ML-SGS model has performed exceptionally well in predicting the local mass transfer rate for the two bubbles which are not part of the ML test case. **Figure 6-8** also shows the effect of mesh resolution on the results of the linear and ML-SGS model. Once again, ML-SGS model outperformed the standard model. Except for the coarsest mesh where the hydrodynamic profile is also probably under resolved the SGS-ML model show better accuracy over the entire polar angle range than the standard model. This is not surprising given the fact that the ML models are trained on a highly resolved mesh before being tested on the coarse meshes of the test cases.

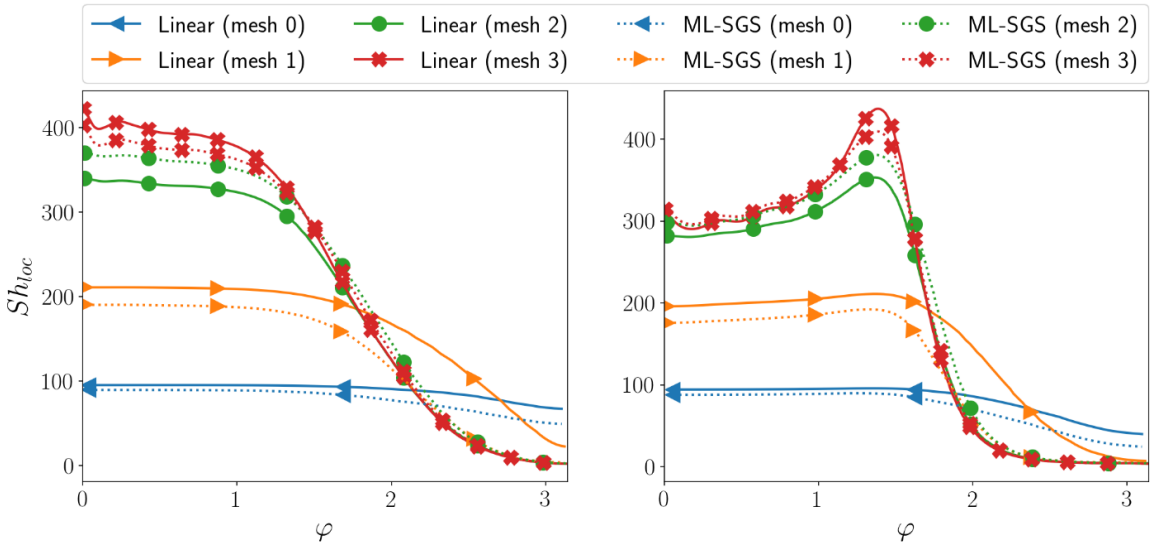

Figure 6-8 Local Sherwood number versus interface polar angles for Case 1 (left) and Case 2 (right).

Another quantity of interest in the mass transfer application is the global Sherwood number, a quantity used in most mass transfer correlations to predict overall mass transfer [147, 148].

$$Sh_{global} = \frac{1}{A_{\Sigma}} \int_{\Sigma} Sh_{loc} dA \tag{6.12}$$

where A_{Σ} is the interface area. The percentage change in global Sherwood number with respect to the one obtained from highest mesh resolution standard model is given in **Table 6-5**. Again, the numbers indicate that the ML-SGS model outperform the standard model for different meshes and also for the dimpled-ellipsoidal bubble where only the result for finest mesh is given.

Table 6-5 Percentage change in global Sherwood number from the reference value.

$\frac{Sh_{global} - Sh_{global\|ref}}{Sh_{global\|ref}} \times 100\%$	mesh 0	mesh 1	mesh 2	mesh 3
Case 1, Linear	-65.16	-39.73	-9.84	0.0
Case 1, ML-SGS	-60.84	-23.70	-0.75	-0.74
Case 2, Linear	-66.75	-43.75	-10.38	0.0
Case 2, ML-SGS	-62.48	-27.14	-1.17	-0.66
Case 3, Linear	_	_	_	0.0
Case 3, ML-SGS	_	_	_	-1.45

The model comparison for the species B, P and S are given in **Figure 6-9**. The left side represents the result obtained from the linear solver with mesh 3 and the right side shows the result of ML-SGS model (also mesh 3). The difference between the two results is negligible with naked eye. **Figure 6-7** and **Figure 6-9** also give an overview of the effect of bubble shape on the reactions.

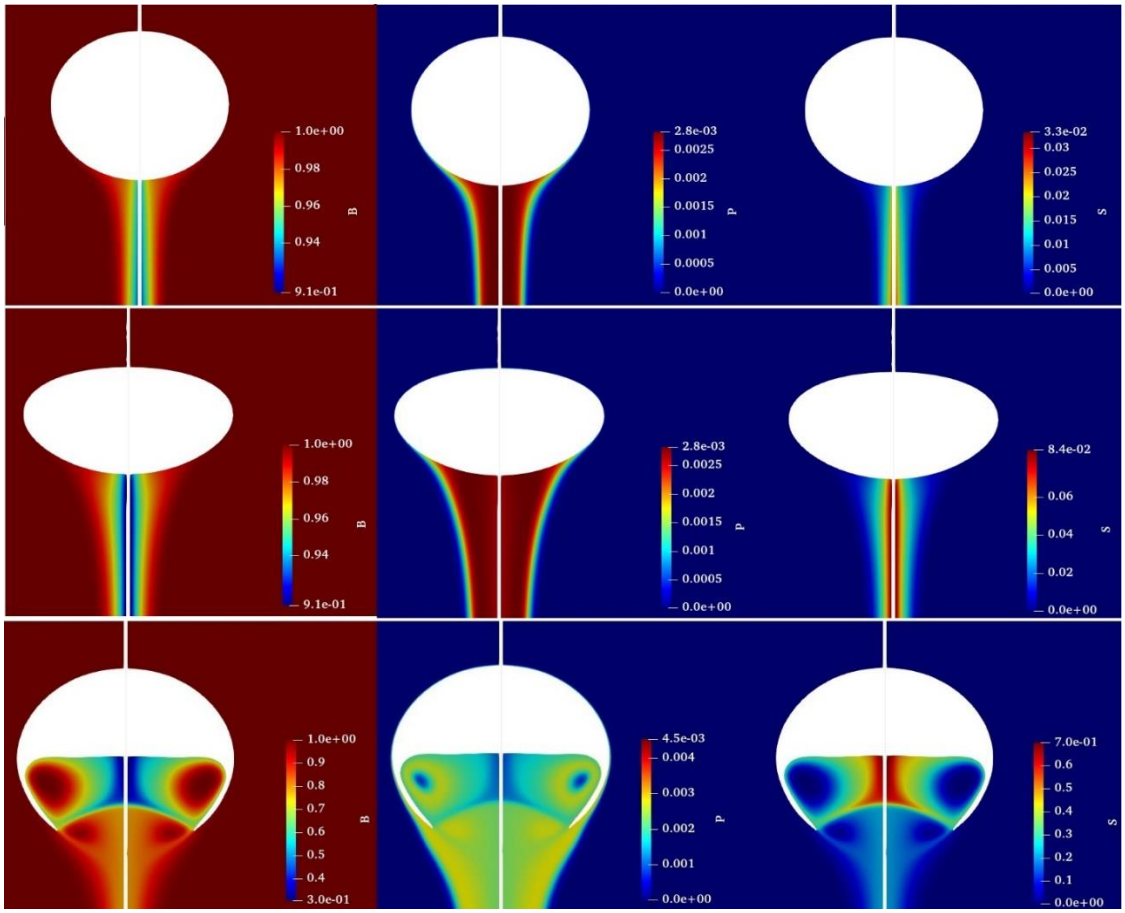

Figure 6-9 Comparison of the concentration profiles of species B, P and S for Case 1 (top), Case 2 (middle) and Case 3 (bottom) using mesh 3. All profiles have two parts: linear (left) and ML-SGS (right).

For Case 1, the bubble is nearly spherical, hence the stagnation zone is small and close to the south pole. The stagnation zone is where the tangential velocities at the interface change sign. To understand the distribution of species around the bubbles two important transport phenomena need to be accounted for: convection and diffusion. Beyond the stagnation zone, convection dominates over diffusion and carries the dissolved oxygen downstream with the flow resulting in a very thin boundary layer. The boundary layer becomes even thinner because the oxygen is consumed in the parallel reactions. At the stagnation zone, however, diffusion is dominant, and the concentration of A is higher.

Case 2 has a wider stagnation zone than Case 1 because of the shape of the bubble with a long wake as Case 1. In the core of the wake, species B has a low concentration because the convection-based exchange with the bulk liquid is minimal. The core of the wake also has a high concentration of the side product S. The dissolved oxygen also accumulates at the inner part of the bubble for the dimpled-ellipsoidal bubble. However, the inner region in this case has two recirculation zones indicated by a low concentration of A. The low concentration is because at the recirculation zone convection dominates over diffusion. Around the recirculation zone, the bulk toluene has the lowest concentration among the three bubble shapes meaning the most efficient conversion of reactant to product. This is also marked by a greater accumulation of product P around the recirculation zone. Since the two reactions are competitive in nature, a high concentration of P and a low concentration of B result in the highest concentration of the side product S for the dimpled-ellipsoidal bubble.

6.8 Conclusion

The study presents a flexible high-fidelity machine learned sub-grid scale modeling technique for studying parallel competitive reactions in a bubble column environment like the oxidation of toluene. A brief discussion of the available SGS modeling techniques is presented and reveal the needs for machine learned sub-grid scale modeling as an efficient alternative over analytical and iterative models. The study used a relatively simple system (spherical bubble) to generate all the data required for training the ML models. An algorithm is presented to incorporate the trained models into a standard computational fluid dynamics (CFD) solver. The ML-SGS model so developed provided highly accurate results when applied to three test cases with different system parameters.

Mesh dependence of the solver is studied and compared with solver using linear reconstruction for face fluxes. The study reveals that the ML-SGS model performed better with low resolution meshes than the linear solver. The ML-SGS model also provided highly accurate concentration profile for species B, P and S. The results reveal the effect of bubble shapes on the formation of product and by products.

7 FUTURE WORK

The results obtained from the study of cyclic jamming in granular system can be used to study the evolution history of the substructures associated with each particle in the granular system. These sub-structures can be represented by the complex network structure formed by groups of particles within the system and can be considered to be part of a finite state space. The evolution of particles' sub-structure can follow this state space. Hence the path taken by all the sub-structures can be analyzed to create a transition matrix for the evolution of sub-structures for granular particles. The key insight will be to observe the most preferred transition of the particles' sub-structure. This will ultimately provide a much deeper knowledge of the self-assembly of granular materials under any loading conditions.

The CVOFLS-DPD method developed in this study is very general and can be extended to study many different fluid-nanoparticle systems. The method already has the capability to handle multi-component liquids miscible or not. Evaporation of complex multi-component liquids, akin to many biological fluids, and the subsequent dried-up substrate pattern is an interesting area of research to be explored in the future. The present model can be extended to include conjugate heat transfer analysis of the substrate where the substrate temperature varies with the evaporating fluid. Further variation is deposit structure can be obtained by varying the temperature of the substrate.

Due to the data driven approach, the ML-SGS solver presented in Chapter 6 has the potential to be extended to employ more advanced deep learning techniques and the trained models can be tested for more challenging cases of deforming bubbles with turbulent wake structures or bubble swarm. That would be an appropriate application of

the data driven technique since there is an obvious scale difference when a full industrial reactor is considered. Deep learning techniques can bridge the gap between the scale where sub-grid scale model is required to the scale where the bubbles collide and mix up to the scale where the whole reactor can be simulated.

8 LIST OF PUBLICATIONS PRODUCED

1. Tayeb, R, Zhang, Y. (2021). Evaporation induced self-assembly of rough colloids: a multiscale simulation study. International Journal of Heat and Mass Transfer. Volume 179, 2021, Article 121681.

2. Tayeb, R, Zhang, Y. (2019). Controlling Evaporation Induced Self-Assembly of Polymeric Nanoparticles: A VOF-DPD Study. Proceedings of the ASME 2019 International Mechanical Engineering Congress and Exposition.

3. Tayeb, R., Mao, Y., & Zhang, Y. (2019). Smoothed particle hydrodynamics simulation of granular system under cyclic compressions. Powder Technology, 353, 84-97.

4. Tayeb, R., Mao, Y., & Zhang, Y. (2016). Numerical Investigation of evaporation induced self-assembly of sub-micron particles suspended in water. ASME 2016 5th International Conference on Micro/Nanoscale Heat and Mass Transfer.

5. Tayeb, R., Mao, Y., & Zhang, Y. (2016). Numerical Simulation of Jamming Transition in Granular System Under Cyclic Compression Using Smooth Particle Hydrodynamics. ASME 2016 International Mechanical Engineering Congress and Exposition.

6. Tayeb, R., Dou, X., Mao, Y., & Zhang, Y. (2016). Analysis of Cohesive Microsized Particle Packing Structure Using History-Dependent Contact Models. ASME. J. Manuf. Sci. Eng. 138(4): 041005.

REFERENCES

[1] Shao, Fenfen, Ng Tuck Wah, Efthimiadis Jim, Somers Anthony, Schwalb Willem, "Evaporative Micro-Particle Self Assembly Influenced by Capillary Evacuation," *Journal of Colloid and Interface Science*, 2012; **377**(1): pp. 421-429.

[2] Mahoney, Luther, Koodali Ranjit, "Versatility of Evaporation-Induced Self-Assembly (Eisa) Method for Preparation of Mesoporous Tio2 for Energy and Environmental Applications," *Materials*, 2014; **7**(4): p. 2697.

[3] Farhadi, Somayeh, Behringer Robert P., "Dynamics of Sheared Ellipses and Circular Disks: Effects of Particle Shape," *Physical Review Letters*, 2014; **112**(14): p. 148301.

[4] Howell, Daniel, Behringer R. P., Veje Christian, "Stress Fluctuations in a 2d Granular Couette Experiment: A Continuous Transition," *Physical Review Letters*, 1999; **82**(26): pp. 5241-5244.

[5] Snoeijer, Jacco H., Ellenbroek Wouter G., Vlugt Thijs J. H., van Hecke Martin, "Sheared Force Networks: Anisotropies, Yielding, and Geometry," *Physical Review Letters*, 2006; **96**(9): p. 098001.

[6] Ren, Jie, Dijksman Joshua A., Behringer Robert P., "Reynolds Pressure and Relaxation in a Sheared Granular System," *Physical Review Letters*, 2013; **110**(1): p. 018302.

[7] Richard, Patrick, Nicodemi Mario, Delannay Renaud, Ribière Philippe, Bideau Daniel, "Slow Relaxation and Compaction of Granular Systems," *Nature Materials*, 2005; **4**: p. 121.

[8] Philippe, P., Bideau D., "Compaction Dynamics of a Granular Medium under Vertical Tapping," *EPL (Europhysics Letters)*, 2002; **60**(5): p. 677.

[9] Alonso-Marroquín, F., Herrmann H. J., "Ratcheting of Granular Materials," *Physical Review Letters*, 2004; **92**(5): p. 054301.

[10] Brown, Robert, "Xxvii. A Brief Account of Microscopical Observations Made in the Months of June, July and August 1827, on the Particles Contained in the Pollen of Plants; and on the General Existence of Active Molecules in Organic and Inorganic Bodies," *The Philosophical Magazine*, 1828; **4**(21): pp. 161-173.

[11] Deegan, Robert D., Bakajin Olgica, Dupont Todd F., Huber Greg, Nagel Sidney R., Witten Thomas A., "Contact Line Deposits in an Evaporating Drop," *Physical Review E*, 2000; **62**(1): pp. 756-765.

[12] Katiyar, Parul, Singh Jayant K., "Evaporation Induced Self-Assembly of Different Shapes and Sizes of Nanoparticles: A Molecular Dynamics Study," *The Journal of Chemical Physics*, 2019; **150**(4): p. 044708.

[13] Spaeth, Justin R., Kevrekidis Ioannis G., Panagiotopoulos Athanassios Z., "Dissipative Particle Dynamics Simulations of Polymer-Protected Nanoparticle Self-Assembly," *The Journal of Chemical Physics*, 2011; **135**(18): p. 184903.

[14] Liu, Wendong, Midya Jiarul, Kappl Michael, Butt Hans-Jürgen, Nikoubashman Arash, "Segregation in Drying Binary Colloidal Droplets," *ACS Nano*, 2019; **13**(5): pp. 4972-4979.

[15] Sung, Pei-Fang, Wang Lihui, Harris Michael T., "Deposition of Colloidal Particles During the Evaporation of Sessile Drops: Dilute Colloidal Dispersions," *International Journal of Chemical Engineering*, 2019; **2019**: p. 7954965.

[16] Bhardwaj, Rajneesh, Fang Xiaohua, Attinger Daniel, "Pattern Formation During the Evaporation of a Colloidal Nanoliter Drop: A Numerical and Experimental Study," *New Journal of Physics*, 2009; **11**(7): p. 075020.

[17] Brilliantov, Nikolai V., Spahn Frank, Hertzsch Jan-Martin, Pöschel Thorsten, "Model for Collisions in Granular Gases," *Physical Review E*, 1996; **53**(5): pp. 5382-5392.

[18] Silbert, Leonardo E., Ertaş Deniz, Grest Gary S., Halsey Thomas C., Levine Dov, Plimpton Steven J., "Granular Flow Down an Inclined Plane: Bagnold Scaling and Rheology," *Physical Review E*, 2001; **64**(5): p. 051302.

[19] Zhang, H. P., Makse H. A., "Jamming Transition in Emulsions and Granular Materials," *Physical Review E*, 2005; **72**(1): p. 011301.

[20] Kloss, Christoph, Goniva Christoph, Hager Alice, Amberger Stefan, Pirker Stefan, "Models, Algorithms and Validation for Opensource Dem and Cfd-Dem," *Progress in Computational Fluid Dynamics, an International Journal*, 2012; **12**(2): pp. 140-152.

[21] Hamaker, H. C., "The London—Van Der Waals Attraction between Spherical Particles," *Physica*, 1937; **4**(10): pp. 1058-1072.

[22] Götzinger, Martin, Peukert Wolfgang, "Dispersive Forces of Particle–Surface Interactions: Direct Afm Measurements and Modelling," *Powder Technology*, 2003; **130**(1–3): pp. 102-109.

[23] Johnson, K. L. , Kendall K. , Roberts A. D., "Surface Energy and the Contact of Elastic Solids," *Proceedings of the Royal Society of London Series A, Mathematical and Physical Sciences*, 1971; **324**(1558): pp. 301-313.

[24] Kern, Willis Frederick, Bland James R. Solid Mensuration: With Proofs. 2nd ed. New York: Wiley 1938.

[25] Zhou, Y. C., Wright B. D., Yang R. Y., Xu B. H., Yu A. B., "Rolling Friction in the Dynamic Simulation of Sandpile Formation," *Physica A-statistical Mechanics and Its Applications*, 1999; **269**(2): pp. 536-553.

[26] Huang, Yrjö J., Nydal Ole Jørgen, Yao Baodian, "Time Step Criterions for Nonlinear Dense Packed Granular Materials in Time-Driven Method Simulations," *Powder Technology*, 2014; **253**(0): pp. 80-88.

[27] Jia, Tao, Zhang Yuwen, Chen J. K., He Y. L., "Dynamic Simulation of Granular Packing of Fine Cohesive Particles with Different Size Distributions," *Powder Technology*, 2012; **218**(0): pp. 76-85.

[28] Xiao Liang, Deng, Rajesh N Dave, "Dynamic Simulation of Particle Packing Influenced by Size, Aspect Ratios and Surface Energy," *Granular Matter*, 2013; **15**: pp. 401-415.

[29] Scott, G. David, "Packing of Spheres: Packing of Equal Spheres," *Nature*, 1960; **188**: pp. 908-909.

[30] An, Xizhong, Li Changxing, "Experiments on Densifying Packing of Equal Spheres by Two-Dimensional Vibration," *Particuology*, 2013; **11**(6): pp. 689-694.

[31] Di Renzo, Alberto, Di Maio Francesco Paolo, "Comparison of Contact-Force Models for the Simulation of Collisions in Dem-Based Granular Flow Codes," *Chemical Engineering Science*, 2004; **59**(3): pp. 525-541.

[32] Lucy, L. B., "A Numerical Approach to the Testing of the Fission Hypothesis," *Astronomical Journal*, 1977; **82**: pp. 1013-1024.

[33] Monaghan, JJ, "Sph Compressible Turbulence," *Monthly Notices of the Royal Astronomical Society*, 2002; **335**(3): pp. 843-852.

[34] Monaghan, J. J., "An Introduction to Sph," *Computer Physics Communications*, 1988; **48**(1): pp. 89-96.

[35] Monaghan, J. J., "Smoothed Particle Hydrodynamics," *Annual Review of Astronomy and Astrophysics*, 1992; **30**(1): pp. 543-574.

[36] Johnson, Gordon R., Stryk Robert A., Beissel Stephen R., "Sph for High Velocity Impact Computations," *Computer Methods in Applied Mechanics and Engineering*, 1996; **139**(1–4): pp. 347-373.

[37] Randles, P. W., Libersky L. D., "Smoothed Particle Hydrodynamics: Some Recent Improvements and Applications," *Computer Methods in Applied Mechanics and Engineering*, 1996; **139**(1–4): pp. 375-408.

[38] Seo, Songwon, Min Oakkey, "Axisymmetric Sph Simulation of Elasto-Plastic Contact in the Low Velocity Impact," *Computer Physics Communications*, 2006; **175**(9): pp. 583-603.

[39] Libersky, Larry D., Petschek Albert G., Carney Theodore C., Hipp Jim R., Allahdadi Firooz A., "High Strain Lagrangian Hydrodynamics," *Journal of Computational Physics*, 1993; **109**(1): pp. 67-75.

[40] Monaghan, J. J., Lattanzio J. C., "A Refined Particle Method for Astrophysical Problems," *Astronomy & Astrophysics*, 1985; **149**: pp. 135-143.

[41] Monaghan, J. J., "Simulating Free Surface Flows with Sph," *Journal of Computational Physics*, 1994; **110**(2): pp. 399-406.

[42] Monaghan, J. J., "Sph without a Tensile Instability," *J Comput Phys*, 2000; **159**(2): pp. 290-311.

[43] Gray, J. P., Monaghan J. J., Swift R. P., "Sph Elastic Dynamics," *Computer Methods in Applied Mechanics and Engineering*, 2001; **190**(49–50): pp. 6641-6662.

[44] Petschek, A. G., Libersky L. D., "Cylindrical Smoothed Particle Hydrodynamics," *Journal of Computational Physics*, 1993; **109**(1): pp. 76-83.

[45] Lubachevsky, B. D., Graham R. L., "Curved Hexagonal Packings of Equal Disks in a Circle," *Discrete & Computational Geometry*, 1997; **18**(2): pp. 179-194.

[46] Radjai, Farhang, Jean Michel, Moreau Jean-Jacques, Roux Stéphane, "Force Distributions in Dense Two-Dimensional Granular Systems," *Physical Review Letters*, 1996; **77**(2): pp. 274-277.

[47] Combe, Gaël, Roux Jean-Noël, "Strain Versus Stress in a Model Granular Material: A Devil's Staircase," *Physical Review Letters*, 2000; **85**(17): pp. 3628-3631.

[48] Edwards, S. F., "The Equations of Stress in a Granular Material," *Physica A: Statistical Mechanics and its Applications*, 1998; **249**(1): pp. 226-231.

[49] O'Hern, Corey S., Silbert Leonardo E., Liu Andrea J., Nagel Sidney R., "Jamming at Zero Temperature and Zero Applied Stress: The Epitome of Disorder," *Physical Review E*, 2003; **68**(1): p. 011306.

[50] O'Hern, Corey S., Langer Stephen A., Liu Andrea J., Nagel Sidney R., "Random Packings of Frictionless Particles," *Physical Review Letters*, 2002; **88**(7): p. 075507.

[51] Silbert, Leonardo E., Ertaş Deniz, Grest Gary S., Halsey Thomas C., Levine Dov, "Geometry of Frictionless and Frictional Sphere Packings," *Physical Review E*, 2002; **65**(3): p. 031304.

[52] van Hecke, M., "Jamming of Soft Particles: Geometry, Mechanics, Scaling and Isostaticity," *Journal of Physics: Condensed Matter*, 2009; **22**(3): p. 033101.

[53] Baranau, Vasili, Hlushkou Dzmitry, Khirevich Siarhei, Tallarek Ulrich, "Pore-Size Entropy of Random Hard-Sphere Packings," *Soft Matter*, 2013; **9**(12): pp. 3361-3372.

[54] Göncü, Fatih, Durán Orencio, Luding S. Jamming in Frictionless Packings of Spheres: Determination of the Critical Volume Fraction; 2009.

[55] Göncü, Fatih, Durán Orencio, Luding Stefan, "Constitutive Relations for the Isotropic Deformation of Frictionless Packings of Polydisperse Spheres," *Comptes Rendus Mécanique*, 2010; **338**(10): pp. 570-586.

[56] Kumar, Nishant, Magnanimo Vanessa, Luding Stefan. Tuning the Bulk Properties of Bidisperse Granular Mixtures by Size Ratio; 2015.

[57] Kumar, Nishant, Magnanimo Vanessa, Ramaioli Marco, Luding Stefan, "Tuning the Bulk Properties of Bidisperse Granular Mixtures by Small Amount of Fines," *Powder Technology*, 2016; **293**: pp. 94-112.

[58] VanderWerf, Kyle, Jin Weiwei, Shattuck Mark D., O'Hern Corey S., "Hypostatic Jammed Packings of Frictionless Nonspherical Particles," *Physical review E*, 2018; **97**(1-1): pp. 012909-012909.

[59] Coppersmith, S. N., Liu C. h, Majumdar S., Narayan O., Witten T. A., "Model for Force Fluctuations in Bead Packs," *Physical Review E*, 1996; **53**(5): pp. 4673-4685.

[60] Majmudar, TS, Sperl M, Luding S, Behringer Robert P, "Jamming Transition in Granular Systems," *Physical review letters*, 2007; **98**(5): p. 058001.

[61] Falk, M. L., Langer J. S., "Dynamics of Viscoplastic Deformation in Amorphous Solids," *Physical Review E*, 1998; **57**(6): pp. 7192-7205.

[62] Rycroft, Chris H., "Voro++: A Three-Dimensional Voronoi Cell Library in C++," *Chaos: An Interdisciplinary Journal of Nonlinear Science*, 2009; **19**(4): p. 041111.

[63] Tordesillas, Antoinette, Walker David M., Lin Qun, "Force Cycles and Force Chains," *Physical Review E*, 2010; **81**(1): p. 011302.

[64] Mehlhorn, Kurt, Michail Dimitrios, "Minimum Cycle Bases: Faster and Simpler," *ACM Trans Algorithms*, 2009; **6**(1): pp. 1-13.

[65] "Numerical Investigation of Dynamic Effects for Sliding Drops on Wetting Defects," *Physical Review E*, 2015; **91**(2).

[66] Ounis, Hadj, Ahmadi Goodarz, McLaughlin John B., "Brownian Diffusion of Submicrometer Particles in the Viscous Sublayer," *Journal of Colloid and Interface Science*, 1991; **143**(1): pp. 266-277.

[67] Li, J., Mason D. J., "A Computational Investigation of Transient Heat Transfer in Pneumatic Transport of Granular Particles," *Powder Technology*, 2000; **112**(3): pp. 273-282.

[68] Hardt, S., Wondra F., "Evaporation Model for Interfacial Flows Based on a Continuum-Field Representation of the Source Terms," *J Comput Phys*, 2008; **227**(11): pp. 5871-5895.

[69] Introduction. Multiphase Flows with Droplets and Particles, Second Edition: CRC Press; 2011: 1-16.

[70] Roenby, Johan, Bredmose Henrik, Jasak Hrvoje, "A Computational Method for Sharp Interface Advection," *Royal Society Open Science*, 2016; **3**(11): p. 160405.

[71] Greenshields, Christopher J., Weller Henry G., Gasparini Luca, Reese Jason M., "Implementation of Semi-Discrete, Non-Staggered Central Schemes in a Colocated, Polyhedral, Finite Volume Framework, for High-Speed Viscous Flows," *International Journal for Numerical Methods in Fluids*, 2010; **63**(1): pp. 1-21.

[72] Saufi, A. E., Frassoldati A., Faravelli T., Cuoci A., "Interface-Resolved Simulation of the Evaporation and Combustion of a Fuel Droplet Suspended in Normal Gravity," *Fuel*, 2020: p. 119413.

[73] Saufi, A. E., Frassoldati A., Faravelli T., Cuoci A., "Dropletsmoke++: A Comprehensive Multiphase Cfd Framework for the Evaporation of Multidimensional Fuel Droplets," *International Journal of Heat and Mass Transfer*, 2019; **131**: pp. 836-853.

[74] Smith, Joseph Mauk. Introduction to Chemical Engineering Thermodynamics. ACS Publications; 1950.

[75] Banerjee, R, Isaac K. M., "An Algorithm to Determine the Mass Transfer Rate from a Pure Liquid Surface Using the Volume of Fluid Multiphase Model," *International Journal of Engine Research*, 2004; **5**(1): pp. 23-37.

[76] Reutzsch, Jonathan, Kieffer-Roth Corine, Weigand Bernhard, "A Consistent Method for Direct Numerical Simulation of Droplet Evaporation," *Journal of Computational Physics*, 2020; **413**: p. 109455.

[77] Cuoci, A., Frassoldati A., Faravelli T., Ranzi E., "Opensmoke++: An Object-Oriented Framework for the Numerical Modeling of Reactive Systems with Detailed Kinetic Mechanisms," *Computer Physics Communications*, 2015; **192**: pp. 237-264.

[78] Foundation, The OpenFOAM. Nsrdsfunc6 Class Reference. https://cpp.openfoam.org/v4/classFoam_1_1NSRDSfunc6.html#details (accessed May 13 2021).

[79] Dupont, Jean-Baptiste, Legendre Dominique, "Numerical Simulation of Static and Sliding Drop with Contact Angle Hysteresis," *Journal of Computational Physics*, 2010; **229**(7): pp. 2453-2478.

[80] Linder, Nicklas. Numerical Simulation of Complex Wetting. 2015; 2015.

[81] Albadawi, A., Donoghue D. B., Robinson A. J., Murray D. B., Delauré Y. M. C., "Influence of Surface Tension Implementation in Volume of Fluid and Coupled Volume of Fluid with Level Set Methods for Bubble Growth and Detachment," *International Journal of Multiphase Flow*, 2013; **53**: pp. 11-28.

[82] Yokoi, Kensuke, "A Density-Scaled Continuum Surface Force Model within a Balanced Force Formulation," *Journal of Computational Physics*, 2014; **278**: pp. 221-228.

[83] Lebedev-Stepanov, Peter, Vlasov Konstantin, "Simulation of Self-Assembly in an Evaporating Droplet of Colloidal Solution by Dissipative Particle Dynamics," *Colloids and Surfaces A: Physicochemical and Engineering Aspects*, 2013; **432**: pp. 132-138.

[84] Lebedev-Stepanov, P. V., Kadushnikov R. M., Molchanov S. P., Rubin N. I., Shturkin N. A., Alfimov M. V., "Simulation of Self-Assembly of Micro- and Nanoparticles in an Evaporating Microdrop of Solution," *Nanotechnologies in Russia*, 2011; **6**(1): pp. 79-87.

[85] Bolintineanu, Dan S., Grest Gary S., Lechman Jeremy B., Pierce Flint, Plimpton Steven J., Schunk P. Randall, "Particle Dynamics Modeling Methods for Colloid Suspensions," *Computational Particle Mechanics*, 2014; **1**(3): pp. 321-356.

[86] Everaers, R., Ejtehadi M. R., "Interaction Potentials for Soft and Hard Ellipsoids," *Physical Review E*, 2003; **67**(4): p. 041710.

[87] Parsons, Drew F., Walsh Rick B., Craig Vincent S. J., "Surface Forces: Surface Roughness in Theory and Experiment," *The Journal of Chemical Physics*, 2014; **140**(16): p. 164701.

[88] Olarte-Plata, Juan D., Brekke-Svaland Gøran, Bresme Fernando, "The Influence of Surface Roughness on the Adhesive Interactions and Phase Behavior of Suspensions of Calcite Nanoparticles," *Nanoscale*, 2020; **12**(20): pp. 11165-11173.

[89] Eom, Namsoon, Parsons Drew F., Craig Vincent S. J., "Roughness in Surface Force Measurements: Extension of Dlvo Theory to Describe the Forces between Hafnia Surfaces," *The Journal of Physical Chemistry B*, 2017; **121**(26): pp. 6442-6453.

[90] Marčelja, Stjepan, "Hydration Forces near Charged Interfaces in Terms of Effective Ion Potentials," *Current Opinion in Colloid & Interface Science*, 2011; **16**(6): pp. 579-583.

[91] Grabbe, Alexis, Horn Roger G., "Double-Layer and Hydration Forces Measured between Silica Sheets Subjected to Various Surface Treatments," *Journal of Colloid and Interface Science*, 1993; **157**(2): pp. 375-383.

[92] Tayeb, Raihan, Dou Xin, Mao Yijin, Zhang Yuwen, "Analysis of Cohesive Microsized Particle Packing Structure Using History-Dependent Contact Models," *Journal of Manufacturing Science and Engineering*, 2015; **138**(4).

[93] Nguyen, Anh V., Evans Geoffrey M., "Axisymmetric Approach of a Solid Sphere toward a Non-Deformable Planar Slip Interface in the Normal Stagnation Flow—Development of Global Rational Approximations for Resistance Coefficients," *International Journal of Multiphase Flow*, 2002; **28**(8): pp. 1369-1380.

[94] Brenner, Howard, "The Slow Motion of a Sphere through a Viscous Fluid Towards a Plane Surface," *Chemical Engineering Science*, 1961; **16**(3): pp. 242-251.

[95] Fan, Tai-Hsi, Vinogradova Olga I., "Hydrodynamic Resistance of Close-Approached Slip Surfaces with a Nanoasperity or an Entrapped Nanobubble," *Physical Review E*, 2005; **72**(6): p. 066306.

[96] Maxwell, R., Ata S., Wanless E. J., Moreno-Atanasio R., "Computer Simulations of Particle–Bubble Interactions and Particle Sliding Using Discrete Element Method," *Journal of Colloid and Interface Science*, 2012; **381**(1): pp. 1-10.

[97] Attard, Phil, Miklavcic Stan J., "Effective Spring Description of a Bubble or a Droplet Interacting with a Particle," *Journal of Colloid and Interface Science*, 2002; **247**(1): pp. 255-257.

[98] Groot, Robert D., Warren Patrick B., "Dissipative Particle Dynamics: Bridging the Gap between Atomistic and Mesoscopic Simulation," *The Journal of Chemical Physics*, 1997; **107**(11): pp. 4423-4435.

[99] Cuoci, Alberto, Frassoldati Alessio, Faravelli Tiziano, Ranzi Eliseo, "A Computational Tool for the Detailed Kinetic Modeling of Laminar Flames: Application to C2h4/Ch4 Coflow Flames," *Combustion and Flame*, 2013; **160**(5): pp. 870-886.

[100] Hysing, S., Turek S., Kuzmin D., et al., "Quantitative Benchmark Computations of Two-Dimensional Bubble Dynamics," *International Journal for Numerical Methods in Fluids*, 2009; **60**(11): pp. 1259-1288.

[101] Klostermann, J., Schaake K., Schwarze R., "Numerical Simulation of a Single Rising Bubble by Vof with Surface Compression," *International Journal for Numerical Methods in Fluids*, 2013; **71**(8): pp. 960-982.

[102] Nguyen, Tuan A. H., Hampton Marc A., Nguyen Anh V., "Evaporation of Nanoparticle Droplets on Smooth Hydrophobic Surfaces: The Inner Coffee Ring Deposits," *The Journal of Physical Chemistry C*, 2013; **117**(9): pp. 4707-4716.

[103] Lohani, Deepa, Basavaraj Madivala G., Satapathy Dillip K., Sarkar Subhendu, "Coupled Effect of Concentration, Particle Size and Substrate Morphology on the Formation of

Coffee Rings," *Colloids and Surfaces A: Physicochemical and Engineering Aspects*, 2020; **589**: p. 124387.

[104] Zhang, Wenbin, Yu Tongxu, Liao Longguang, Cao Zexian, "Ring Formation from a Drying Sessile Colloidal Droplet," *AIP Advances*, 2013; **3**(10): p. 102109.

[105] Marin, Alvaro, Liepelt Robert, Rossi Massimiliano, Kähler Christian J., "Surfactant-Driven Flow Transitions in Evaporating Droplets," *Soft Matter*, 2016; **12**(5): pp. 1593-1600.

[106] Bhardwaj, Rajneesh, Fang Xiaohua, Somasundaran Ponisseril, Attinger Daniel, "Self-Assembly of Colloidal Particles from Evaporating Droplets: Role of Dlvo Interactions and Proposition of a Phase Diagram," *Langmuir*, 2010; **26**(11): pp. 7833-7842.

[107] Parsa, Maryam, Boubaker Riadh, Harmand Souad, Sefiane Khellil, Bigerelle Maxence, Deltombe Raphaël, "Patterns from Dried Water-Butanol Binary-Based Nanofluid Drops," *Journal of Nanoparticle Research*, 2017; **19**(8): p. 268.

[108] González-Gutiérrez, Jorge, Pérez-Isidoro Rosendo, Ruiz-Suárez J. C., "A Technique Based on Droplet Evaporation to Recognize Alcoholic Drinks," *Review of Scientific Instruments*, 2017; **88**(7): p. 074101.

[109] Carreón, Yojana J. P., Ríos-Ramírez Maricarmen, Moctezuma R. E., González-Gutiérrez Jorge, "Texture Analysis of Protein Deposits Produced by Droplet Evaporation," *Scientific Reports*, 2018; **8**(1): p. 9580.

[110] Khinast, Johannes G., Koynov Athanas A., Leib Tiberiu M., "Reactive Mass Transfer at Gas–Liquid Interfaces: Impact of Micro-Scale Fluid Dynamics on Yield and Selectivity of Liquid-Phase Cyclohexane Oxidation," *Chemical Engineering Science*, 2003; **58**(17): pp. 3961-3971.

[111] Falcone, Manuel, Bothe Dieter, Marschall Holger, "3d Direct Numerical Simulations of Reactive Mass Transfer from Deformable Single Bubbles: An Analysis of Mass Transfer Coefficients and Reaction Selectivities," *Chemical Engineering Science*, 2018; **177**: pp. 523-536.

[112] Majumder, Subrata Kumar. Hydrodynamics and Transport Processes of Inverse Bubbly Flow: Elsevier; 2016.

[113] Khinast, Johannes G., "Impact of 2-D Bubble Dynamics on the Selectivity of Fast Gas–Liquid Reactions," *AIChE Journal*, 2001; **47**(10): pp. 2304-2319.

[114] Dani, Adil, Guiraud Pascal, Cockx Arnaud, "Local Measurement of Oxygen Transfer around a Single Bubble by Planar Laser-Induced Fluorescence," *Chemical Engineering Science*, 2007; **62**(24): pp. 7245-7252.

[115] Francois, J., Dietrich N., Guiraud P., Cockx A., "Direct Measurement of Mass Transfer around a Single Bubble by Micro-Plifi," *Chemical Engineering Science*, 2011; **66**(14): pp. 3328-3338.

[116] Kück, U. D., Schlüter M., Räbiger N., "Analyse Des Grenzschichtnahen Stofftransports an Frei Aufsteigenden Gasblasen," *Chemie Ingenieur Technik*, 2009; **81**(10): pp. 1599-1606.

[117] Dudukovic, Milorad P., Larachi Faical, Mills Patrick L., "Multiphase Reactors – Revisited," *Chemical Engineering Science*, 1999; **54**(13): pp. 1975-1995.

[118] Mills, P. L., Chaudhari R. V., "Reaction Engineering of Emerging Oxidation Processes," *Catalysis Today*, 1999; **48**(1): pp. 17-29.

[119] Aboulhasanzadeh, B., Thomas S., Taeibi-Rahni M., Tryggvason G., "Multiscale Computations of Mass Transfer from Buoyant Bubbles," *Chemical Engineering Science*, 2012; **75**: pp. 456-467.

[120] Bothe, Dieter, Kroger Michael, Alke Andreas, Warnecke Hans-Joachim, "Vof-Based Simulation of Reactive Mass Transfer across Deformable Interfaces," *Progress in Computational Fluid Dynamics, an International Journal*, 2009; **9**(6-7): pp. 325-331.

[121] Weber, Paul S., Marschall Holger, Bothe Dieter, "Highly Accurate Two-Phase Species Transfer Based on Ale Interface Tracking," *International Journal of Heat and Mass Transfer*, 2017; **104**: pp. 759-773.

[122] Koynov, Athanas, Khinast Johannes G., Tryggvason Grétar, "Mass Transfer and Chemical Reactions in Bubble Swarms with Dynamic Interfaces," *AIChE Journal*, 2005; **51**(10): pp. 2786-2800.

[123] Radl, Stefan, Koynov Athanas, Tryggvason Grétar, Khinast Johannes G., "Dns-Based Prediction of the Selectivity of Fast Multiphase Reactions: Hydrogenation of Nitroarenes," *Chemical Engineering Science*, 2008; **63**(12): pp. 3279-3291.

[124] Roghair, I., Van Sint Annaland M., Kuipers J. A. M., "An Improved Front-Tracking Technique for the Simulation of Mass Transfer in Dense Bubbly Flows," *Chemical Engineering Science*, 2016; **152**: pp. 351-369.

[125] Aboulhasanzadeh, B., Tryggvason G., "Effect of Bubble Interactions on Mass Transfer in Bubbly Flow," *International Journal of Heat and Mass Transfer*, 2014; **79**: pp. 390-396.

[126] Cano-Lozano, José Carlos, Martínez-Bazán Carlos, Magnaudet Jacques, Tchoufag Joël, "Paths and Wakes of Deformable Nearly Spheroidal Rising Bubbles Close to the Transition to Path Instability," *Physical Review Fluids*, 2016; **1**(5): p. 053604.

[127] Bhaga, D., Weber M. E., "Bubbles in Viscous Liquids: Shapes, Wakes and Velocities," *Journal of Fluid Mechanics*, 2006; **105**: pp. 61-85.

[128] Clift, Roland, Grace John R, Weber Martin E, "Bubbles, Drops, and Particles," 2005.

[129] Weiner, Andre, PhD Thesis, "Modeling and Simulation of Convection-Dominated Species Transfer at Rising Bubbles," 2020.

[130] Andre Weiner, https://github.com/AndreWeiner, Accessed July, 2021.

[131] Feng, Yuwei, Zeng Aiwu, "Selective Liquid-Phase Oxidation of Toluene with Molecular Oxygen Catalyzed by Mn3o4 Nanoparticles Immobilized on Cnts under Solvent-Free Conditions," *Catalysts*, 2020; **10**(6): p. 623.

[132] Mal, Diptangshu Datta, Khilari Santimoy, Pradhan Debabrata, "Efficient and Selective Oxidation of Toluene to Benzaldehyde on Manganese Tungstate Nanobars: A Noble Metal-Free Approach," *Green Chemistry*, 2018; **20**(10): pp. 2279-2289.

[133] Hoorn, J. A. A., Van Soolingen J., Versteeg G. F., "Modelling Toluene Oxidation: Incorporation of Mass Transfer Phenomena," *Chemical Engineering Research and Design*, 2005; **83**(2): pp. 187-195.

[134] Gast, Sebastian, Tuttlies Ute S., Nieken Ulrich, "Kinetic Study of the Toluene Oxidation in Homogeneous Liquid Phase," *Chemical Engineering Science*, 2020; **217**: p. 115500.

[135] Bird, R Byron, Stewart Warren E, Lightfoot Edwin N. Transport Phenomena: John Wiley & Sons; 2006.

[136] Weiner, Andre, Bothe Dieter, "Advanced Subgrid-Scale Modeling for Convection-Dominated Species Transport at Fluid Interfaces with Application to Mass Transfer from Rising Bubbles," *Journal of Computational Physics*, 2017; **347**: pp. 261-289.

[137] Levich, Veniamin Grigorevich, "Physicochemical Hydrodynamics," 1962.

[138] Gründing, Dirk, Fleckenstein Stefan, Bothe Dieter, "A Subgrid-Scale Model for Reactive Concentration Boundary Layers for 3d Mass Transfer Simulations with Deformable Fluid Interfaces," *International Journal of Heat and Mass Transfer*, 2016; **101**: pp. 476-487.

[139] Weiner, Andre, Timmermann Jens, Pesci Chiara, et al., "Experimental and Numerical Investigation of Reactive Species Transport around a Small Rising Bubble," *Chemical Engineering Science: X*, 2019; **1**: p. 100007.

[140] Weiner, Andre, Hillenbrand Dennis, Marschall Holger, Bothe Dieter, "Data-Driven Subgrid-Scale Modeling for Convection-Dominated Concentration Boundary Layers," *Chemical Engineering & Technology*, 2019; **42**(7): pp. 1349-1356.

[141] Laboratory, BYU DIPPR® Thermophysical Properties, University Brigham Young, Provo UT 84602. The Design Institute for Physical Property Data. 2021. https://dippr.aiche.org/ (accessed April 20, 2021.

[142] Tang, Liang Bin, "Kinetics of the Liquid-Phase Oxidation of Toluene by Air," *Industrial & Engineering Chemistry Research*, 2007; **46**(20): pp. 6442-6448.

[143] Paul, Melanie, Strassl Florian, Hoffmann Alexander, Hoffmann Marko, Schlüter Michael, Herres-Pawlis Sonja, "Reaction Systems for Bubbly Flows," *European Journal of Inorganic Chemistry*, 2018; **2018**(20-21): pp. 2101-2124.

[144] Paszke, Adam, Gross Sam, Massa Francisco, et al. Pytorch: An Imperative Style, High-Performance Deep Learning Library. 2019. p. 8024-8035.

[145] Greenshields, Christopher J, "Openfoam: The Open Source Cfd Toolbox," *User Guide*, 2015.

[146] Collobert, Ronan, Bengio Samy. Links between Perceptrons, Mlps and Svms. Proceedings of the twenty-first international conference on Machine learning. Banff, Alberta, Canada: Association for Computing Machinery; 2004. p. 23.

[147] Lochiel, A. C., Calderbank P. H., "Mass Transfer in the Continuous Phase around Axisymmetric Bodies of Revolution," *Chemical Engineering Science*, 1964; **19**(7): pp. 471-484.

[148] Takemura, Fumio, Yabe Akira, "Gas Dissolution Process of Spherical Rising Gas Bubbles," *Chemical Engineering Science*, 1998; **53**(15): pp. 2691-2699.

VITA

Raihan Tayeb was born in Izeh, Iran but he is from Bangladesh. He completed his Bachelor of Science in Mechanical Engineering at the Bangladesh University of Engineering and Technology, graduating in March 2012. In July 2014 Raihan obtained his Master of Science in Mechanical and Aerospace Engineering from the University of Missouri-Columbia for his thesis work, "Study of Micro-sized Particle Deposition Using Dem, CFD-DEM and SPH Approach". Finally, he received his Doctoral Degree also in Mechanical and Aerospace Engineering from the University of Missouri-Columbia for his work, " Numerical Study of Self-Assembly of Granular and Colloidal Particles". During his PhD at MU, he was responsible for several research projects focused on multiphase flows, phase change and fluid-particle interactions. In particular, he developed several related mathematical models and high performance computing (HPC) codes that can run complex Computational Fluid Dynamics (CFD) and Solid Mechanics cases.